

Rochester Institute of Technology

**RIT Digital Institutional Repository**

---

Theses

---

5-21-2024

## **Nano Biosensing Platform for Infectious Disease Diagnostics**

Li Liu

ll7067@rit.edu

Follow this and additional works at: <https://repository.rit.edu/theses>

---

### **Recommended Citation**

Liu, Li, "Nano Biosensing Platform for Infectious Disease Diagnostics" (2024). Thesis. Rochester Institute of Technology. Accessed from

This Dissertation is brought to you for free and open access by the RIT Libraries. For more information, please contact [repository@rit.edu](mailto:repository@rit.edu).

# R·I·T

## **Nano Biosensing Platform for Infectious Disease**

### **Diagnostics**

By

Li Liu

A dissertation submitted in partial fulfillment of the requirements  
for the degree of Doctorate of Philosophy in Microsystems Engineering

Microsystems Engineering Program  
Kate Gleason College of Engineering

Rochester Institute of Technology  
Rochester, New York  
May 21st, 2024

**Dissertation Title**  
**by**  
**Author**

**Committee Approval:**

We, the undersigned committee members, certify that we have advised and/or supervised the candidate on the work described in this dissertation. We further certify that we have reviewed the dissertation manuscript and approve it in partial fulfillment of the requirements of the degree of Doctor of Philosophy in Microsystems Engineering.

---

Ke Du Assistant Professor	Date
------------------------------	------

---

Mitchell R. O'Connell Assistant Professor	Date
--	------

---

Chuanhua Duan Associate Professor	Date
--------------------------------------	------

---

Michael Schrlau Associate Professor	Date
--	------

---

Michael Schertzer Associate Professor	Date
--	------

**Certified by:**

---

Stefan Preble Director, Microsystems Engineering Program	Date
---	------

---

Doreen Edwards Dean, Kate Gleason College of Engineering	Date
---	------

# ABSTRACT

Kate Gleason College of Engineering  
Rochester Institute of Technology

**Degree:** Doctor of Philosophy

**Program:** Microsystems Engineering

**Authors Name:** Li Liu

**Advisors Name:** Ke Du

**Dissertation Title:** Nano Biosensing Platform for Infectious Disease Diagnostics

CRISPR-Cas enabled biosensors offer great potential to be at the forefront of diagnostic medicine. This thesis focuses on the principles of CRISPR-Cas technology and its application to biosensors and virus diagnostics. It also provides a detailed discussion of the different detection methods available at this stage. The breakthrough achievements of CRISPR biosensors in nucleic acid detection are summarized. The CRISPR-Cas nano biosensors exhibit high accuracy, sensitivity, selectivity, and versatility, offering great potential for next-generation diagnostic and point-of-care devices. The prospects and future trends of CRISPR biosensors are also described.

From an engineering perspective, this thesis develops and applies several methods for CRISPR-based viral detection. A nanopore array platform for high-throughput single-molecule sensing was developed. Gold nanoparticle-labeled reactions for CRISPR virus detection were used as reporter signals, demonstrating the ability to lower the limits of detection reached while maintaining CRISPR accuracy and selectivity. An electrochemical sensor platform based on CRISPR virus detection was then developed, with electrochemistry offering the advantages of simple measurement procedures, short reaction

times, and adequate sensitivity and selectivity. Combined with the high selectivity of CRISPR, it makes detection more rapid and convenient.

Finally, we have developed an integrated digital microfluidic chip that realizes precise quantitative detection of nucleic acids and incorporates an isothermal amplification method to greatly reduce the detection limit, providing an excellent advancement for next-generation bedside diagnostics. Digital microfluidic chips and nanofluidic chips developed in recent years offer the advantages of greater resistance to inhibition, higher sensitivity, and more precise detection. Digital microarrays, in combination with nucleic acid amplification methods, allow absolute quantitative analysis of nucleic acid targets by dispensing the target molecules into small wells or droplets. When the sample is divided into numerous aliquots, these aliquots contain no target molecules or only one molecule. The concentration of the target molecule can then be derived by counting the number of positive aliquots.

This research addresses current hotspots in virus detection by developing several different virus detection platforms that not only reduce the detection limit, but also allow in-depth analysis of the physical and chemical properties of the molecules during the reaction.

## ACKNOWLEDGMENTS

First and foremost, I would like to express my deepest gratitude to my advisor, Dr. Ke Du, for his unwavering support, invaluable guidance, and continuous encouragement throughout my research journey. He has helped and inspired me a lot, both in academic guidance and as a person. It gave me more confidence and strength to face my future life.

I would also like to extend my sincere thanks to the members of my thesis committee, Dr. Mitchell R. O'Connell, Dr. Chuanhua Duan, Dr. Michael Schrlau, Dr. Michael Schertzer, and Dr. Karin Wuertz-Kozak, for their constructive feedback and insightful suggestions, which greatly enhanced the quality of my work.

My heartfelt thanks go to my colleagues and collaborators, Dr. Zhiheng Xu, Dr. Guohua Yi, Dr. Fan Yang, Dr. Denis Cormier, Dr. Stephen J Dollery, Dr. Gregory J Tobin, Dr. Kamel Awayda, Dr. Adrian Moises Molina Vargas, Dr. Guoyu Lu, Dr. Juhong Chen, Dr. Matthew D. Moore, etc. Without their supporting and collaborating, I cannot finish our work. And I also very thankful for my lab members, Dr. Xinye Chen, Dr. Can Wang, Dr. Mengdi Bao, Dr. Yu Chang, Dr. Jiaxiang Ye, Dr. Bhaskar Sharma, Ruonan Peng, Henry Yuqing, Jacob Waitkus, Natalie Luu and Kenny Hass, for their camaraderie, intellectual discussions, and emotional support. Their companionship has made this journey more enjoyable and less arduous.

I am deeply grateful to my family for their unconditional love, patience, and encouragement. To my parents, Yuzhi Fu and Baohua Liu, for always believing in me and

providing me with the foundation to pursue my dreams. To my siblings Yiming Liu, for his constant support and understanding.

Furthermore, I would like to express my gratitude to myself. During this difficult yet fulfilling academic journey, I encountered many challenges and obstacles. However, it was these very difficulties that fostered my growth and progress. I want to thank myself for never giving up and for my unwavering perseverance in the face of pressure and setbacks. This steadfast belief and determination helped me overcome numerous difficulties and ultimately enabled me to successfully complete my doctoral studies. I am grateful for my passion for academic research, which has been my driving force and source of motivation. I hope that in the future, I can continue to maintain this enthusiasm and resilience, constantly pursuing new knowledge and dreams.

Lastly, my appreciation goes to all the participants and respondents who contributed to my research. Without their cooperation, this thesis would not have been possible.

Thank you all for your contributions and support.

Li Liu

# Contents

<i>ABSTRACT</i> .....	2
<i>ACKNOWLEDGMENTS</i> .....	4
<i>Contents</i> .....	6
<i>List of Publications and Conferences</i> .....	9
<i>List of Figures</i> .....	11
<i>Chapter 1. Introduction: Advanced nano-biosensor for diagnosing viruses</i> .....	17
1.1 Introduction.....	17
1.2 CRISPR-Cas-based nucleic acid detection .....	19
1.3 Amplification-based detection .....	31
1.4 Outline and Contributions .....	37
<i>Chapter 2. Nanopore sensing and recent advances in nanopore research related to solid-state nanopores</i> .....	40
2.1 Introduction.....	40
2.2 Working principle of the nanopore sensor. ....	41
2.3 Selective sensing using molecular probes .....	44
2.4 Gold Nanoparticle-Labeled CRISPR-Cas13a Assay for nanopore virus detection .....	46
<i>Chapter 3. Electrochemical application in virus detection</i> .....	64
3.1 Introduction.....	64
3.2 Biosensors using electrochemical detection .....	65

3.3 Aerosol jet printing prints highly sensitive electrodes.....	68
3.4 Electrochemical and Colorimetric Biosensor for SARS-CoV-2 Detection.....	68
<i>Chapter 4. Loop-mediated amplification integrated on microfluidic chips for point-of-care quantitative detection of nucleic acid.....</i>	<i>86</i>
4.1 Introduction.....	86
4.2 The different strategy of LAMP visualization nucleic acid detection method	87
4.3 Introduction of Microfluidic Nano digital chip for nucleic acid detection .....	92
4.4 Integrated microfluidic chip for isothermal amplification detection of nucleic acids.....	95
4.5 Microfabrication of the integrated Nano digital microfluidic chip .....	98
4.6 Characteristics of the Nano-dChip and on-chip reaction .....	100
<i>Chapter 5. 3D Digital chip for simple and highly quantitative detection of HPV DNA</i>	<i>108</i>
5.1 Introduction.....	108
5.2 Characteristic of silicon chip and principle of digital chip .....	111
5.3 Analytical sensitivity and specificity of FQ-LAMP assay .....	112
5.4 On-chip reaction.....	115
5.5 Computer vision enables precise analysis.....	118
5.6 Highly quantitative nucleic acid detection and analysis.....	120
<i>Chapter 6. Conclusion: Micro Biosensing platform to fundamentals and applications</i>	<i>124</i>

<b>6.1 Conclusions.....</b>	<b>124</b>
<b>6.2 Future perspective in virus detection .....</b>	<b>126</b>
<b>6.3 Summarizing and Understanding Virus Detection.....</b>	<b>135</b>
<b><i>Bibliography</i>.....</b>	<b><i>137</i></b>

## List of Publications and Conferences

1. **Liu, L.**, Kasputis, T., Chen, J., Moore, M., and Du, K. Fully integrated digital nanofluidic chip for simple and highly quantitative detection of Norovirus, *in preparation*.
2. Kasputis, T., Yeh, P., **Liu, L.**, Marano, J., Weger-Lucarelli, J., Du, K., Lin, L., and Chen, J.(2024). Development of a self-powered digital microfluidic chip (SP-dChip) for the detection of emerging viruses, *In preparation*.
3. **Liu, L.**, Dollery, S., Tobin, G., Lu, G., and Du, K. (2024). Cleavable energy transfer labeled oligonucleotide probe for enhanced isothermal amplification detection and digital chip-based readout, *In preparation*.
4. Chen, X., **Liu, L.**, Lomeli-Prieto, J., Gu, J., Li, J., Ma, S., and Du, K. Nano-sieve based on-chip particle concentration for nucleic acid sensing, Proc. *SPIE* 12837, Microfluidics, BioMEMS, and Medical Microsystems XXII, 128370A (March 2024).
5. **Liu, L.**, Du, K. (2024). A perspective on computer vision in biosensing. *Biomicrofluidics*. 18, 011301.
6. Bao, M., Waitkus, J., **Liu, L.**, Chang, Y., Xu, Z., Qin, P., Chen, J., and Du, K. (2023). Micro-and Nano-systems for the Detection of Hemorrhagic Fever Viruses. *Lab on a Chip*. 23 (19), 4173-4200.
7. **Liu, L.**, Xu, Z., Vargas A., Dollery, S., Schrlau, M., Cormier, D., O'Connell, M., Tobin, G., and Du, K. (2023) Aerosol jet printing enabled dual-function electrochemical and colorimetric biosensor for SARS-CoV-2 detection. *Analytical Chemistry*. 95(32), 11997–12005.

8. **Liu, L.**, Xu, Z., Vargas A., Dollery, S., Schrlau, M., Cormier, D., O'Connell, M., Tobin, G., and Du, K. Aerosol jet printing enabled dual-function electrochemical and colorimetric biosensor for SARS-CoV-2 detection. The 66th International Conference on Electron, Ion and Photon Beam Technology and Nanofabrication (EIPBN), San Francisco, CA (June 2nd, 2023).
9. Waitkus, J., Chang, Y., **Liu, L.**, Puttaswamy, S., Chung, T., Vargas, A., Dollery, S., O'Connell, M., Cai, H., Tobin, G., Bhalla, N\*., and Du, K. (2022). Gold nanoparticle enabled localized surface plasmon resonance on unique gold nanomushroom structures for on-chip CRISPR-Cas13a sensing, *Advanced Materials Interfaces*, 10(1), 2370004.
10. **Liu, L.**, Xu, Z., Awayda, K., Dollery, S. J., Bao, M., Fan, J., ... & Du, K. (2022). Gold Nanoparticle-Labeled CRISPR-Cas13a Assay for the Sensitive Solid-State Nanopore Molecular Counting. *Advanced Materials Technologies*, 7(3), 2101550.
11. Yang, F.,\* **Liu, L.**,\* Neuenschwander, P. F., Idell, S., Vankayalapati, R., Jain, K. G., ... & Yi, G. (2021). Phage Display-Derived Peptide for the Specific Binding of SARS-CoV-2. *ACS omega*, 7(4), 3203-3211.
12. **Liu, L.**, Dubrovsky, M., Gundavarapu, S., Vermeulen, D., & Du, K. (2021, March). Viral nucleic acid detection with CRISPR-Cas12a using high contrast cleavage detection on micro-ring resonator biosensors. In *Frontiers in Biological Detection: From Nanosensors to Systems XIII* (Vol. 11662, pp. 8-13). *SPIE*.
13. Hass, K. N., Bao, M., He, Q., **Liu, L.**, He, J., Park, M., ... & Du, K. (2020). Integrated micropillar polydimethylsiloxane accurate CRISPR detection system for viral DNA sensing. *ACS omega*, 5(42), 27433-27441.

## List of Figures

Figure 1.1 The guide-target RNA duplex activates HEPN catalytic site of Cas13a. Reprinted from .....	20
Figure 1.2 Overall mechanism of CRISPR-guided diagnostic applications using optical detection. Reprinted from .....	21
Figure 1.3 Cell-free DNA (cfDNA) detection method using DNA-functionalized Au nanoparticles via colorimetric and metal enhanced fluorescence (MEF). Reprinted from .....	23
Figure 1.4 Schematic of the fluorescence sensing unit with a 488 nm laser as an excitation source and CRISPR Cas12a detection mechanism: CRISPR Cas12a binds with crRNA and ASFV-DNA and the Cas12a/crRNA/ASFV complex cleaves ssDNA probe for fluorescence sensing. Reprinted from .....	24
Figure 1.5 (a) Schematic of the clustered regularly interspaced short palindromic repeats (CRISPR)-based IMPACT chip DNA detection. (b) Photograph of the IMPACT chip. The dashed white box indicates regions patterned with micropillars. (c) Schematic of the surface treatment protocol, ssDNA probe binding, and CRISPR detection. Reprinted from .....	26
Figure 1.6 The EFE electrochemical CRISPR biosensor operates via immobilization-free detection, utilizing trans-cleavage and cis-cleavage activities of CRISPR-Cas12a. A pulsed electric field attracts nucleic acids to the positively charged working electrode surface. Electrochemical detection reveals increased current in the presence of target DNA due to reduced release of negative MB-labeled probe by Cas12a's trans-cleavage activity. Reprinted from .....	28
Figure 1.7 The schematic of the LSPR between AuNPs and AuNMs. Reprinted from ...	29
Figure 1.8 Schematic of the sandwich-structured protein detection process. Reprinted from .....	30
Figure 1.9 Schematic representation of the LAMP mechanism. Design of the primers for LAMP. Forward inner primer (FIP): F2 sequence with F1c sequence at the 5' end. Backward inner primer (BIP): B2 sequence with B1c sequence at the 5' end. Outer primers are designed at the regions of F3 and B3. Reprinted from .....	35
Figure 1.10 Principle of SARS-CoV-2 fragment detection using RPA amplification and CRISPR cleavage. Reprinted from .....	36
Figure 2.1 Illustrates the working principle of a nanopore sensor. a. The diagram of nanopore sensing. b. The signal analysis such as duration, signal amplitude, and signal frequency. c. Typical nanopore signal diagram. Reprinted from .....	43
Figure 2.2 Typical fabrication methods for solid nanopores. (a) Diagram of nanopore fabrication. (b) Relationship between nanopore diameter and thickness using helium ion etching method. (c)(d)(e) TEM images for different diameters nanopore. Reprinted from .....	44
Figure 2.3 Detection of local protein structures along DNA using solid-state nanopores. (a) Schematic layout of the experiment. DNA molecules (purple) are locally coated with RecA proteins (orange). The inset shows a TEM of a 30 nm diameter nanopore. (b) Current trace before and after addition of the molecules. (c) Conductance histogram of all events. Reprinted from .....	45

Figure 2.4 Schematic of solid-state CRISPR-Cas12a-assisted nanopore (SCAN) sensor. (a) Positive case, the trans-cleavage activity of the Cas12a after activation causes degradation of the circular ssDNA reporters, resulting in reduced reporter event rate through the nanopore. (b) Negative case, the Cas12a is not activated in the absence of target dsDNA and thus the ssDNA reporters are not cleaved. The nanopore event rate remains high. Reprinted from ..... 46

Figure 2.5 Schematic of the solid-state nanopore sensing platform. The nanopore chip is sandwiched between two microfluidic reservoirs (blue) and silicone pads. The trans-cleavage of CRISPR-Cas13a releases the gold nanoparticles to pass through the solid-state nanopore and changes the ionic current. Reprinted from ..... 50

Figure 2.6 (a) TEM image of the nanopore chip with a pore diameter of 90 nm with diagram showing cross-section. (b) A representative current–voltage (I–V) calibration curve of a ~90 nm nanopore in 1 M KCl. The inset shows the liner fits yield a conductance of 732.1 nS and the diagram of KCl buffer passing through the nanopore. Reprinted from ..... 51

Figure 2.7 (a) Schematic of the AuNP-Cas13-based nucleic acid detection strategy: Step 1. Cas13a/crRNA complex cleavage of ssRNA probes; Step 2. Streptavidin-coated AuNPs bind biotin-labeled ssRNA probes. Step 3. FAM-labeled ssRNA probes bind anti-FAM coated magnetic beads; Step 4. Magnetic bead isolation of non-cleaved ssRNA. Reprinted from ..... 52

Figure 2.8 The SARS-CoV-2 gene locus, target site, and the guide RNA sequence. Reprinted from ..... 53

Figure 2.9 The SARS-CoV-2 gene locus, target site, and the guide RNA sequence. (a) Images of the AuNPs containing the indicated concentrations of (i) SARS-CoV-2 target RNA (positive) and (ii) SARS-CoV-1 target RNA (negative). (b) TEM images of the cleaved products of (i) 100 nM of SARS-CoV-2 target RNA and (ii) 100 nM of SARS-CoV-1 target RNA. Scale bars are 200 nm. Reprinted from ..... 54

Figure 2.10 (a) Schematic of AuNPs (40 nm) passing through a nanopore chip (90 nm) at different concentrations. (b) Typical current-time traces of AuNPs (0.5 fM, 5 fM, 50 fM, 0.5 pM, 5 pM, and 50 pM) passing through a 90 nm nanopore with arrows showing detection events. Reprinted from ..... 55

Figure 2.11 (a) Nanopore event rate versus AuNP concentration ranging from 0.5 fM to 50 nM. (b) The histograms of the distribution of current increase corresponding to the translocations of AuNPs with various concentrations, fitted to Gaussian curves. Reprinted from ..... 56

Figure 2.12 (a) Scatter plots show increased current vs. dwell time for different concentrations of AuNPs. (b) ECD distribution with different concentrations of AuNPs. (c) Box plot of the event charge deficits (ECD) for various concentrations of AuNPs. Reprinted from ..... 56

Figure 2.13 (a) Ionic current vs. time trace for translocation events count, dwell time histograms, count and current histograms, and scatterplots of current and dwell time for different concentrations of SARS-CoV-2 target, labeled by AuNP-Cas13a assay. (b) Current trace of different concentrations of SARS-CoV-1 target (negative control). Reprinted from ..... 58

Figure 2.14 Nanopore event rate versus RNA concentration (50 fM to 50 nM): SARS-CoV-2 (black); SARS-CoV-1 (red). ( $R^2=0.9944$ ) Reprinted from ..... 59

Figure 2.15 The inter-arrival time of the translocation event for different concentrations of AuNPs, following the Poisson process. Reprinted from ..... 61

Figure 2.16 (a) Current trace and ionic current vs time trace for the AuNPs through (a) 90 nm nanopore chip and (b) 150 nm nanopore chip. Reprinted from ..... 62

Figure 3.1 Schematic illustrating the on-chip cleavage procedure for samples with or without target miRNAs (blue). The biotin and 6-FAM-labeled reporter RNA is immobilized to the anti-biotin antibody, where the GOx-labeled anti-fluorescein antibody binds to the reporter RNA. The crRNA/Cas13a complex and a sample with and without target miRNAs (blue), is introduced into the biosensor to the completely pre-immobilized assay. The target activated enzyme cleaves the bound reporter RNA and thus enables the removal of the GOx-labeled antibody, resulting in a reduced amperometry signal. Reprinted from ..... 67

Figure 3.2 Electrochemical Strategy for Low-Cost Viral Detection. MB (methylene blue)-labeled oligonucleotides immobilized on gold leaf electrodes, the activated Cas12a can cleavage the oligonucleotides and resulting in the voltametric signal changes. Reprinted from ..... 68

Figure 3.3 A. Schematic of the reaction strategy: Step 1. CRISPR-Cas13a:crRNA complex cleaves an ssRNA probe; Step 2. Anti-FAM HRP binds the FAM labeled ssRNA probe; Step 3. The non-cleaved biotin-labeled ssRNA probe is isolated by streptavidin magnetic beads; Step 4. Colorimetric reaction and current detection with TMB oxidization. B. SARS-CoV-2 gene location, target site, and guide RNA sequence. C. Current Signal Change Ratio with and without SARS-CoV-2 target, showing ~3-fold difference in signal. The statistical significances are calculated by *t*-test (\*\*\*\*P ≤ 0.0001). Error bars: SD, n=3. Reprinted from ..... 75

Figure 3.4 A. (1) Schematic of the aerosol jet printing process for the dual-function biosensor and the graphene electrode with a working electrode, a counter electrode, and a reference electrode. (2) The photonic curing system for the graphene electrode. Reprinted from ..... 76

Figure 3.5 A. Profilometer scan of the graphene electrode, showing a smooth surface with only ± 0.2 μm variation. B. Graphene electrode voltammetry curves for H<sub>2</sub>SO<sub>4</sub> solution (0.05 mM). Lines 1, 2, and 3 are scans on the same day, and lines 4, 5, and 6 are scans from different days (one day apart). Reprinted from ..... 77

Figure 3.6 Height value of electrode cross section. Reprinted from ..... 77

Figure 3.7 A. UV-vis spectrum vs. SARS-CoV-2 RNA concentration after RNA detection by our assay. B. UV-vis spectrum vs. positive and negative target. C. Top: Photographs of the test solution with different SARS-CoV-2 concentrations under daylight. Bottom: The relationship between the integrated absorbance and the concentration of SARS-CoV-2 RNA. Inset: The calibration curve for the integrated absorbance value vs. The logarithm of the target concentration. Error bars denote standard deviation (n = 5). D. Top: Photographs of the test solution of different targets under daylight. Detection specificity of the SARS-CoV-2 RNA target compared with other targets. Error bars denote standard deviation (n = 5). The asterisks represent statistical significance according to a *t*-test of \*P ≤ 0.05, \*\*P ≤ 0.01, \*\*\*P ≤ 0.001, \*\*\*\*P ≤ 0.0001. Reprinted from ..... 79

Figure 3.8 A. Top: Photographs of the test solution with different SARS-CoV-2 RNA concentrations under daylight. Bottom: The relationship between the R value and the

concentration of the SARS-CoV-2 RNA. Inset: Calibration curve of the R value vs. The logarithm of the target concentration. Error bars denote standard deviation (n = 5). B. Top: Photographs of the test solution with different RNA targets under daylight. Bottom: Detection specificity of the SARS-CoV-2 RNA target compared with other targets. Error bars denote standard deviation (n = 5). The asterisks represent statistical significance according to a *t*-test. \*P ≤ 0.05, \*\*P ≤ 0.01, \*\*\*P ≤ 0.001, \*\*\*\*P ≤ 0.0001. Reprinted from..... 80

Figure 3.9 A. Chronoamperometric responses of SARS-CoV-2 RNA targets at different concentrations. B. Plot of current of last 30s mean value versus different concentrations of SARS-CoV-2 target. Error bars denote standard deviation (n = 5). Inset: Calibration curve of the current vs. the logarithm of the target concentration. C. Chronoamperometric responses of the positive and negative targets. D. Detection specificity of the SARS-CoV-2 RNA target compared with other targets. Error bars denote standard deviation (n = 5). The asterisks represent statistical significance according to a *t*-test. \*P ≤ 0.05, \*\*P ≤ 0.01, \*\*\*P ≤ 0.001, \*\*\*\*P ≤ 0.0001. Reprinted from ..... 81

Figure 3.10 R value intensity and measured current vs. target RNA concentration with a R<sup>2</sup> value of 0.9508 and 0.9913, respectively. Error bars denote standard deviation (n = 5). Reprinted from..... 82

Figure 4.1 Overview of indirect and direct detection methods used for monitoring loop-mediated isothermal amplification (LAMP). A. Chemical equation for the DNA polymerase reaction. Me<sup>2+</sup> represents a metal ion that can be detected indirectly by LAMP byproducts. B. Top: Magnesium pyrophosphate precipitation causes either a turbid solution or the appearance of white particles. Middle: The color change in hydroxynaphthol blue (HNB) can be attributed to a decrease in magnesium. Bottom: Calcium xanthophyll is initially quenched by manganese. C. Direct detection of amplified DNA using DNA cross-linking dyes such as SYBR Green I, EvaGreen, and berberine. Reprinted from..... 88

Figure 4.2 Colorimetric detection of the SARS-CoV-2 DNA by LAMP reactions. .... 90

Figure 4.3 Fluorescent dye-based LAMP reaction result. 1. LAMP result with Eva green dye, target is lambda DNA, the detection limit can reach the 10 aM. The bottom figure shows the turbidity result of positive and negative. 2. LAMP result with SYBR Green I dye, the top photograph shows the tube under natural light. And the bottom photograph shows the fluorescent signal, the detection limit can reach 10 aM..... 91

Figure 4.4 The gel electrophoresis image of Norovirus RNA sample..... 95

Figure 4.5 a. The schematic of the RT-LAMP reaction using a FAM-FIP probe and Quenching probe. b. The concentration of FIP was fixed at 1.6 μM, and 0 μM, 0.8 μM, 1.6 μM, and 2.4 μM of the quenching probe were added, respectively. The best quenching effect was observed with a quenching probe concentration of 2.4 μM (with a quencher probe to FIP probe ratio of 1.5:1). (mean ± SD, n = 3)..... 98

Figure 4.6 a. Comparison of positive and negative results for mismatched sequences of the quencher probe, including fully matched, one mismatch, two mismatches, and three mismatches, demonstrating optimal quenching only when all bases are fully matched (mean ± SD, n = 3). b. Comparison of positive and negative results for mismatched sequences of the quencher probe, including 1. 8th mismatch, 2. 9th mismatch, 3. 10th mismatch and 4. fully matched, demonstrating optimal quenching only when all bases are fully matched (mean ± SD, n = 3)..... 98

Figure 4.7 a. A photograph of the microfluidic chip, with red food dye load onto it to enhance visibility of the microfluidic channel. b. Design and dimensions of the microfluidic chip, the channels and vacuum lungs have a width of 200  $\mu\text{m}$ , and the wells have a dimension of  $400 \times 200 \times 100 \mu\text{m}$  (length  $\times$  width  $\times$  depth) that will hold a liquid of 8 nL. The whole microfluidic chip has 1040 wells, and each well will be one individual reactor. c. Chip fabrication step: (1) Silicon wafer used as substrate; (2) The negative photoresist SU-8 utilized as a mold; (3) PDMS mixture poured onto the mold to create the channels; (4) PDMS channels bonded on glass substrate to form the chip. d. Microfluidic chip filled with reaction reagent and mineral oil, observed under bright-field illumination. .... 100

Figure 4.8 Vacuum lung on the chip. a. Side view of the nano dChip design, the vacuum lung design which can remove the reaction reagent into dead-end wells for digital amplification. b. Reaction reagent automatically driven by vacuum lung, after fill with mineral oil, the wells will separate into thousand reaction chambers. c. The design of the vacuum lung enables the reaction reagent to be automatically loaded into the chip in 3 minutes. d. The chips without the vacuum lung cannot automatically load samples. .... 102

Figure 4.9 Quantitative digital amplification of nucleic acid. a. The concept of digital amplification. Wells have target templates are amplified, whereas others remain unamplified. One can determine the original template concentration by counting the number of amplified wells. Isothermal nucleic acid amplification was done with RT-LAMP. b. the average well area was  $432.7 \pm 42.98 (\times 1000 \mu\text{m}^2)$  with a 9.9% variation in pore area ( $R^2=0.9819$ ). c. the average fluorescence intensity was  $118098 \pm 11351 \text{ a.u.}$ , with a variation in fluorescence intensity of 9.6% ( $R^2=0.9787$ ). .... 103

Figure 4.10 a. The end-point fluorescence images of reactions with different starting concentrations of Norovirus RNA. Scale bar, 5 mm. b. The relationship between number of wells and the concentration of the Norovirus RNA (mean  $\pm$  SD,  $n = 3$ ). c. Calibration curve of the number of wells vs the logarithm of the target concentration (mean  $\pm$  SD,  $n = 3$ ). The asterisks represent statistical significance according to a *t*-test. \* $P \leq 0.05$ , \*\* $P \leq 0.01$ , \*\*\* $P \leq 0.001$ , \*\*\*\* $P \leq 0.0001$ . .... 104

Figure 5.1 a. Schematic illustration of FQ LAMP assay. One-pot reaction mixture is first prepared in one tube. The sample mixture then distributed randomly into over ten thousand of microwells. When incubated at 63  $^{\circ}\text{C}$ , each micro reaction with plasmid HPV 16 DNA target undertakes reaction and generates strong green fluorescence (positive spots), whereas not in those without target (negative spots). Through detecting and counting the positive micro reactions (or spots), plasmid HPV 16 DNA can be quantified based on the proportion of positive spots. b. SEM image of micro digital chip, Scale bar is 60  $\mu\text{m}$ . .... 111

Figure 5.2 a. (1) 450-base pair (bp) sequences of HPV-L1 gene from HPV16 insert into plasmid cDNA3.1(+) vector. (2) Principle of the FQ-LAMP assay. In the assay, LAMP's loop backward (LB) primer was used to design the FQ LAMP probe, the target sequence recognition and enhanced fluoresce detection of the FQ LB probe. .... 113

Figure 5.3 a. The LAMP conditions were optimized for the reaction with a mixture of LB/FQ LB primers at concentrations of 0.2, 0.4, and 0.6  $\mu\text{M}$ , respectively. b. The LAMP conditions were optimized for the reaction with a mixture ratio of LB/FQ LB primers were 2:1, 2:2, and 2:4, respectively. For each concentration's testing, error bars denote

the standard deviation ( $n = 3$ ). The asterisks represent statistical significance according to a t-test.  $*P \leq 0.05$ ,  $**P \leq 0.01$ ,  $***P \leq 0.001$ ,  $****P \leq 0.0001$ . ..... 114

Figure 5.4 a. Endpoint fluorescence detection of the FQ LAMP after 45-min amplification of various concentrations of plasmid HPV 16 DNA targets, from 10 aM to 1 pM. b. Endpoint fluorescence detection of the Plasmid HPV 16 DNA target (1 pM) compared with plasmid HPV 18 DNA target (1 pM) and no template control. For each concentration's testing, error bars denote the standard deviation ( $n = 3$ ). The asterisks represent statistical significance according to a t-test.  $*P \leq 0.05$ ,  $**P \leq 0.01$ ,  $***P \leq 0.001$ ,  $****P \leq 0.0001$ . ..... 115

Figure 5.5 a. The concept of digital amplification. Wells that have at least one or more target templates are amplified, whereas others remain unamplified. One can determine the original template concentration by counting the number of amplified wells. Isothermal nucleic acid amplification was done with LAMP. b. Endpoint fluorescence micrographs of the QuantStudio digital chip for the HPV 16 detection with various incubation time (0, 15, 30, 45, 60 and 90 min) at 63 °C. 1 pM plasmid HPV 16 DNA and no template control were loaded. Scale bar, 1 mm. c. The average positive spots increase to a detectable level within 15 min, and when the time was greater than 45 min, there was no significant change in the positive spots. Error bars denote the standard deviation ( $n = 5$ ). d. Histogram of well area conforming to Gaussian distribution ( $R^2=0.9805$ ), 10 pM plasmid HPV 16 DNA target was loaded, proofing the chip has the high uniformity of all wells. .... 116

Figure 5.6 a. End-point fluorescence images of reactions with different starting concentrations of plasmid HPV 16 DNA target within 45 min incubation at 63 °C. Scale bar, 1 mm. b. Quantification range of the digital chip. The relationship between positive spots (Y) and concentration of targets (X), from 100 aM to 100 pM. The low-end shows the enlarged view of low concentration range from 100 aM to 100 fM. c. End-point fluorescence images for the specificity detection. Plasmid HPV 16 PC, Plasmid HPV 18 control and no template control. Scale bar, 1 mm. d. Detection specificity of the Plasmid HPV 16 DNA target (1 pM) compared with plasmid HPV 18 DNA target (1 pM) and no template control. For each concentration's testing, error bars denote the standard deviation ( $n = 5$ ). The asterisks represent statistical significance according to a t-test.  $*P \leq 0.05$ ,  $**P \leq 0.01$ ,  $***P \leq 0.001$ ,  $****P \leq 0.0001$ . ..... 118

Figure 5.7 Image processing and testing result classification pipeline of computer vision enabled HPV target sensing on Digital Nanofluidic Chip, which involves feature generation, intensity range selection, and feature classification. .... 120

Figure 6.1 Overview of the progress, challenges, and prospects for computer vision in biosensors application. Reprinted from ..... 128

# **Chapter 1. Introduction: Advanced nano-biosensor for diagnosing viruses**

## **1.1 Introduction**

Humanity has been confronted with viral infections throughout its history. The history of mankind is a history of struggle and coexistence with multiple viruses. Especially in the past two decades, there has been an increasing frequency of emerging viral infections, including SARS, Ebola, and Zika, causing significant public health concerns [1]. The rapid detection of viral infections is very important for the early prevention of diseases. The incredibly swift global spread of COVID-19 re-emphasizes the critical need for rapid and sensitive molecular diagnostics to combat current and future pandemics. The clustered regularly interspaced short palindromic repeats (CRISPR) technology has been used in pathogens detection for many years and has excellent performance [2]. In recent years, the (CRISPR)-associated proteins (Cas) systems have led to significant advances in the field of genome editing. Especially, Cas12 and Cas13 show trans-cleavage behaviors. CRISPR-Cas12a or Cas13a effector proteins are RNA-guided enzymes that cut DNA/RNA components of bacterial adaptive immune systems. Specifically, the binding of Cas12a/Cas13a to its target DNA/RNA unleashes nonspecific ssDNA/RNA cleavage activity, which completely degrades other existing ssDNA/RNA molecules. This target-activated trans-ssDNA/RNA collateral activity of Cas12/Cas13 has been used for molecular diagnostics of DNA/RNA molecules and led to the development of many detection methods, such as fluorescent readout assays [3], colorimetric readout [4], electrochemical detection [5], etc. Meanwhile, CRISPR-Cas systems combined with amplification methods can significantly improve the detection limit with better specificity

[6]. Moreover, integrating CRISPR systems microfluidic devices can realize the point of care detection [7], which can make the detection more convenient, fast, and sensitive.

Nucleic acid amplification-based methods are another molecular diagnostic approach that has received much attention. In recent years, many methods for virus detection have been developed. Sensitive polymerase chain reaction (PCR) based tests are the gold standard for molecular diagnostics [8], and currently it's still the main testing method for nucleic acid detection. However, this testing method has some disadvantages, such as its reliance on bulky and expensive instruments, the need for professional laboratory personnel to do the test, and easy detection of false positive results due to nonspecific amplification. Thus, they are not suitable for self-diagnosis or point-of-care (POC) settings. Isothermal amplification is a molecular biology technique that has garnered significant attention in recent years due to its versatility and numerous advantages over traditional PCR (polymerase chain reaction) methods. This method involves the amplification of DNA or RNA at a constant temperature, eliminating the need for thermal cycling equipment and streamlining the amplification process. There are many advantages like simplicity and cost-effectiveness, rapid amplification, robustness and tolerance to inhibitors, and versatility compared with traditional PCR. Isothermal amplification of nucleic acids combined with point-of-care devices can enable rapid and sensitive molecular diagnostics.

This thesis develops several different virus detection platforms using current virus detection approaches, which not only reduces the detection limit but also provides an in-depth analysis of the physical and chemical properties of the molecules during the reaction.

## 1.2 CRISPR-Cas-based nucleic acid detection

### 1.2.1 Introduction of CRISPR diagnostics technology

The clustered regularly interspaced short palindromic repeats (CRISPR) diagnostics technology is a novel approach for sensitive and specific in vitro DNA/RNA detection [9]. The activated CRISPR complex demonstrates collateral cleavage of single-stranded nucleic acids. This collateral cleavage is then transduced into an amplified signal using nucleic acid reporters. Compared with traditional amplified virus detection methods, CRISPR-based diagnostics have several advantages, including high specificity due to enzyme recognition of specific target nucleic acid sequences, with almost no false-positive signals. In addition, CRISPR's convenient isothermal reaction generally has an optimal reaction temperature of 37 degrees, which does not require complex temperature cycling devices to achieve optimal reaction results. Furthermore, fast reaction time, especially Cas13a enzyme for reporter RNA probes, can be completed within ten minutes for trans-cleavage. These advantages enabled us to develop a simple detection method using the CRISPR/Cas system and apply this method to diagnosing many kinds of pathogens. **Figure 1.1** shows the Cas13a is activated by guide RNA [10]. The HEPN catalytic site of the Cas enzyme is activated when the guide target nucleic acid is complementary to the target nucleic acid sequence.

**The HEPN catalytic site of Cas13a is activated by the formation of guide-target RNA duplex.**

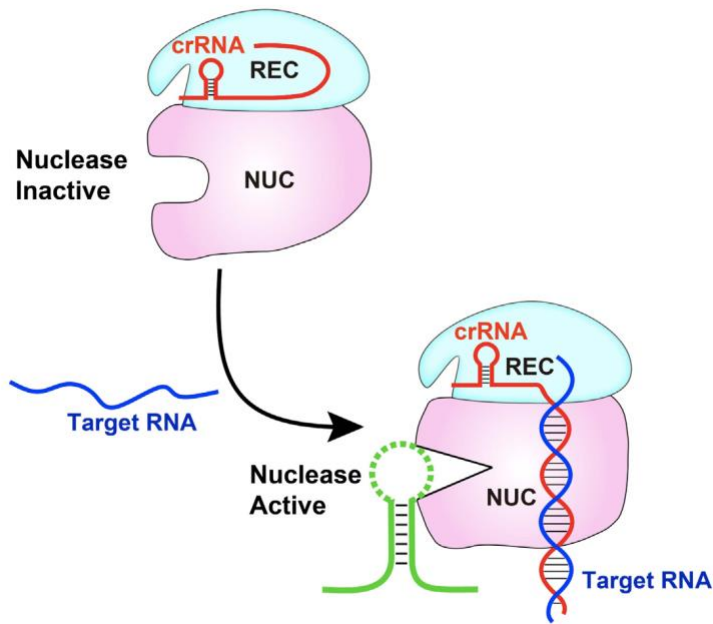


Figure 1.1 The guide-target RNA duplex activates HEPN catalytic site of Cas13a. Reprinted from [10]

At the same time, the CRISPR-Cas system can be combined with various detection methods, such as colorimetric detection [11] or detection of visual fluorescence signals [12] by a simple portable optical detector. Using this approach, many diseases diagnostic methods have been developed.

Biosensing diagnostics have a very promising future as a CRISPR-based application. Depending on the characteristics of the Cas enzymes, such as Cas12 or Cas13, they can cleave a reporter in *trans* when the guide RNA sequence is complementary to the virus sequence. Therefore, it has not only high sensitivity but also specificity and thus can significantly reduce false positive signals. Fluorescent dyes, metal nanoparticles, and other molecules are often used as labeled reporter molecules in CRISPR diagnostics. These

molecules have specific chemical properties, desirable optical and electrocatalytic properties, etc. Therefore, using different sensing methods, including but not limited to fluorescence, luminescent resonance, colorimetric, and electrochemical signal readout, CRISPR technology has driven tremendous advances in nano biosensors. **Figure 1.2** shows a typical mechanism of CRISPR-guided diagnostic applications using optical detection [13]. Patient samples can be extracted from blood, urine, cells, etc. The target nucleic acids can be recognized by Cas proteins, triggering trans-cleavage activities, and releasing reporter molecules.

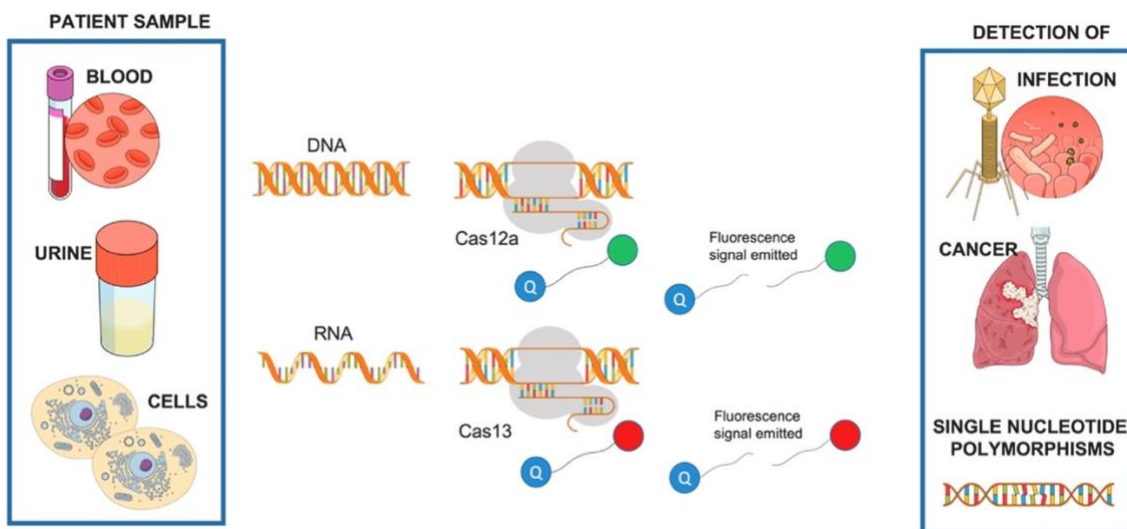


Figure 1.2 Overall mechanism of CRISPR-guided diagnostic applications using optical detection. Reprinted from [13]

### 1.2.2 Colorimetric-based detection

Reporter nucleic acids can be labeled with different analytes, like fluorescent dyes, metal particles, dyes that can produce colorimetric reactions, etc. By detecting the analytes, we can detect pathogens. Gold nanoparticles are a kind of particle that is usually used in nano biosensors due to their specific characteristics [14]. Their intrinsic features (optics,

electronics, and physicochemical characteristics) can be altered by changing the characterization of the nanoparticles, such as shape, size, and aspect ratio. The optical properties of AuNPs are dependent on surface plasmon resonance (SPR), which is the fluctuation and interaction of electrons between negative and positive charges at the surface [15]. Jin-Ha et al. developed a strategy for CRISPR-Cas12 based gold nanoparticles assisted metal enhanced fluorescence and colorimetric detection [16]. **Figure 1.3** shows the schematic for the two gold nanoparticle reactions. Different sizes of gold nanoparticles were hybridized via two complimentary ssDNA, and one ssDNA was functionalized with FITC, which is quenched by gold nanoparticles. After applying the activated CRISPR-Cas12a complex, the hybrid DNA will be cleaved, leading to fluorescence emission and solution color change to red-purple color due to the dispersal of the gold nanoparticles. Using this system, breast cancer gene-1 (BRCA-1) can be detected with very high sensitivity (as low as 0.34 fM) in 30 min.

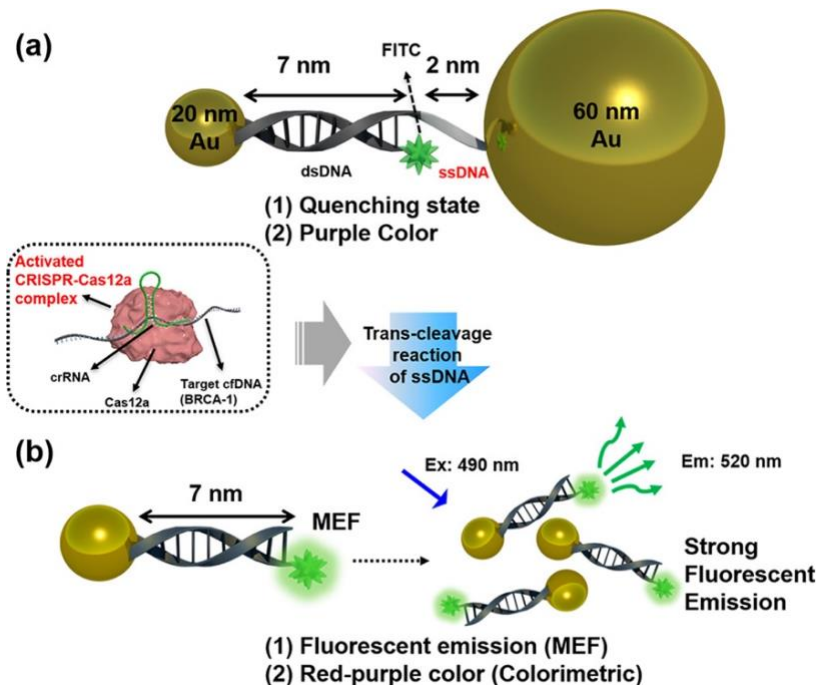


Figure 1.3 Cell-free DNA (cfDNA) detection method using DNA-functionalized Au nanoparticles via colorimetric and metal enhanced fluorescence (MEF). Reprinted from [16]

### 1.2.3 Fluorescence-based detection

The CRISPR-based fluorescence-based nucleic acid detection method capitalizes on the precise targeting capability of CRISPR systems to detect specific sequences of DNA or RNA [17]. This method offers several advantages over traditional approaches, including rapidity, sensitivity, specificity, and simplicity. Moreover, it does not require the complex amplification steps of PCR, making it particularly suitable for point-of-care diagnostics and field applications. Fluorescence-based detection is a widely utilized method employing fluorescent indicators to label the target of interest. When the target is present in the sample, these fluorescent labels become activated, emitting a distinctive fluorescence signal that can be measured and quantified. Unlike colorimetric detection, which offers qualitative sensing, the use of quantum dots (QDs) [18], dyes [19], and other fluorescent materials [20] enables quantitative detection. He, et al. developed a high-throughput, all-solution phase, isothermal detection system for African Swine Fever Virus (ASFV), combining CRISPR-Cas12a with a fluorescence-based point-of-care (POC) system [21]. Notably, the compact system includes a disposable cartridge and custom-designed fluorometer, suitable for low-resource settings. **Figure 1.4** shows the Schematic of disposable cartridge fluorescence-based detection system and CRISPR Cas12a-based detection methods.

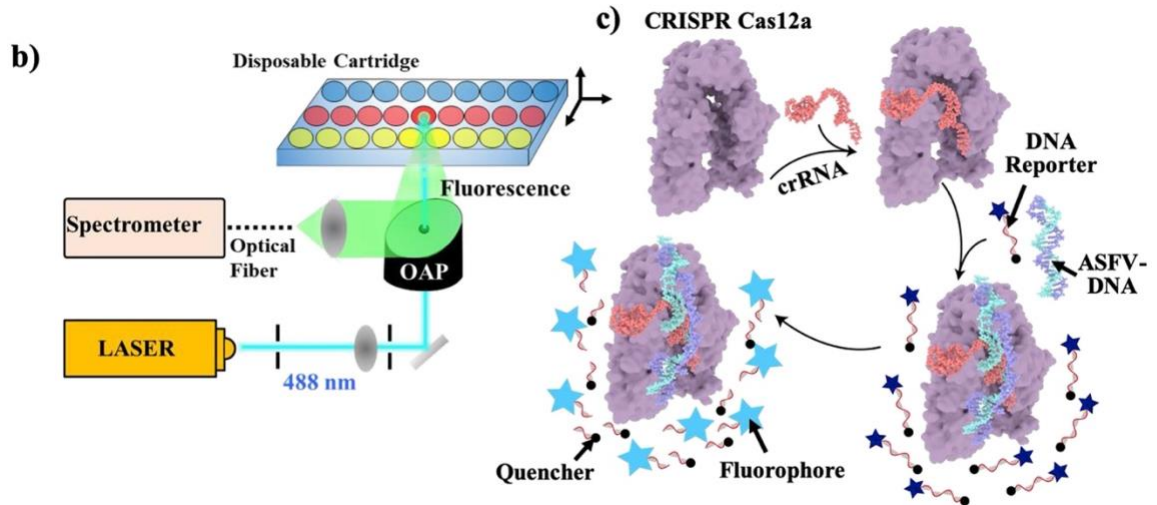


Figure 1.4 Schematic of the fluorescence sensing unit with a 488 nm laser as an excitation source and CRISPR Cas12a detection mechanism: CRISPR Cas12a binds with crRNA and ASFV-DNA and the Cas12a/crRNA/ASFV complex cleaves ssDNA probe for fluorescence sensing. Reprinted from [21]

In the pursuit of enhancing diagnostic tests and bioimaging, the fusion of CRISPR-based assays with complementary technologies, such as microfluidics and nanotechnology, has emerged as a promising strategy [2]. This amalgamation has yielded significant advancements, particularly through integration with microfluidic chips and nanomaterials, which have substantially bolstered assay sensitivity and efficiency [22]. These synergistic approaches capitalize on the distinctive attributes of microfluidic systems and nanomaterials, leveraging their capabilities to augment every facet of the detection process [23]. Advances in fabrication processes for nanostructures have also enhanced the prospects for nanotechnology applications [24], [25], [26]. From enhancing target capture to amplifying signals and facilitating detection readout, these innovative strategies represent a transformative leap forward in molecular diagnostics and imaging modalities.

Microfluidic chips provide a highly controlled environment for sample manipulation and analysis on a miniaturized scale [27]. By integrating CRISPR-based detection assays onto microfluidic platforms, researchers can achieve precise control over reaction conditions, sample handling, and reaction kinetics. Microfluidic channels and chambers enable efficient mixing of reagents, rapid sample processing, and reduced sample volumes, ultimately improving the overall sensitivity and speed of CRISPR-based detection assays [28]. In addition, microfluidic chips also enable multiple detection [29]. Hass et al. developed a fully Integrated Micropillar Polydimethylsiloxane Accurate CRISPR detection (IMPACT) system for viral DNA detection [30]. The system, featuring high-aspect-ratio micropillars for enhanced reporter probe binding, undergoes surface modification and probe immobilization before the injection of the CRISPR-Cas12a/crRNA complex into the microchannel. Notably, the system avoids traditional dye-quencher-labeled probes, minimizing fluorescence background. Additionally, the one-step detection protocol operates on-chip at isothermal conditions (37°C), eliminating the need for off-chip probe hybridization and denaturation. **Figure 1.5** shows the schematic of the microfluidic chip design and surface reaction of the IMPACT reaction.

Furthermore, nanotechnology offers versatile tools for enhancing CRISPR-based detection through the development of novel nanomaterials and nanostructures. Nanoparticles, such as gold nanoparticles, quantum dots, and magnetic nanoparticles, can be functionalized with CRISPR components, including guide RNAs and Cas proteins, to improve target capture and signal amplification. These nanomaterials can enhance the sensitivity of CRISPR-based detection by increasing the surface area available for target binding and

enabling signal enhancement strategies, such as fluorescence resonance energy transfer (FRET) and surface-enhanced Raman scattering (SERS).

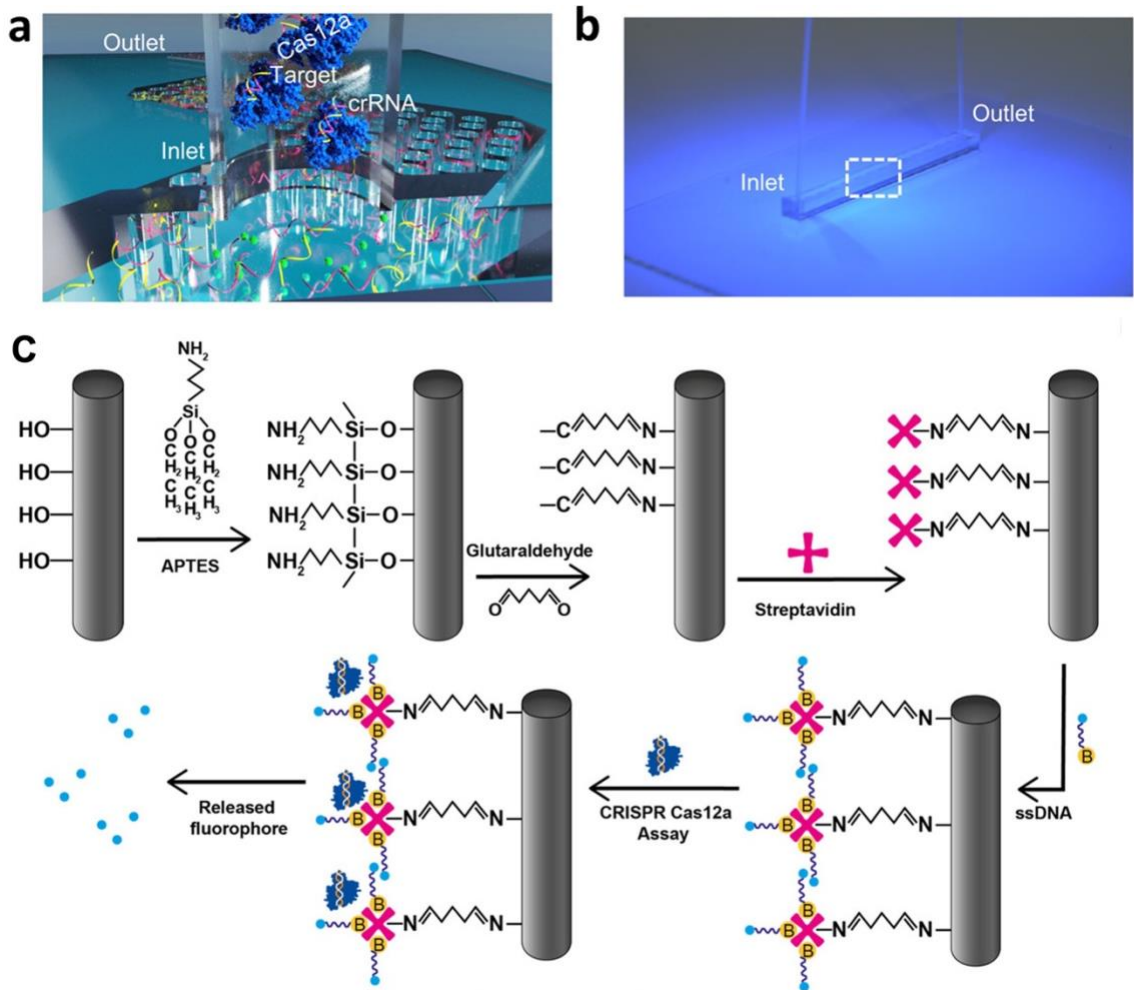


Figure 1.5 (a) Schematic of the clustered regularly interspaced short palindromic repeats (CRISPR)-based IMPACT chip DNA detection. (b) Photograph of the IMPACT chip. The dashed white box indicates regions patterned with micropillars. (c) Schematic of the surface treatment protocol, ssDNA probe binding, and CRISPR detection. Reprinted from [30]

#### 1.2.4 Electrochemical-based detection

Electrochemical-based detection methods for viruses involve the use of electrochemical sensors or biosensors to detect and quantify viral particles or viral nucleic acids. These methods rely on the principle of converting biochemical interactions or target recognition

events into measurable electrical signals, providing a sensitive and specific means of virus detection [31]. Electrochemical biosensors combine the specificity of biological recognition elements with the sensitivity of electrochemical detection. These biosensors typically consist of an electrode modified with a receptor, such as antibodies, aptamers, or enzymes, that can selectively interact with the viral target. The binding event results in an electrochemical signal that can be quantitatively measured. Various electrochemical techniques, including amperometry, potentiometry, and conductometry, can be employed in electrochemical biosensors for virus detection [32].

Electrochemical-based detection methods for viruses offer advantages such as high sensitivity, rapid response, and the potential for miniaturization and portability [33]. They have found applications in viral diagnostics, environmental monitoring, and point-of-care testing, contributing to the timely detection and control of viral infections. These methods continue to be explored and developed for their potential in improving virus detection and surveillance strategies. Li, et al. developed an electric field enhanced, electrochemical CRISPR biosensor for DNA detection in a homogeneous solution [34]. A pulsed electric field was applied to enrich nucleic acids on the electrode surface, enabling sensitive DNA biosensing. The developed CRISPR biosensor can directly detect unamplified human papillomavirus-16 (HPV-16) DNA with a sensitivity of 1 pM. **Figure 1.6** shows the working principle of the EFE platform.

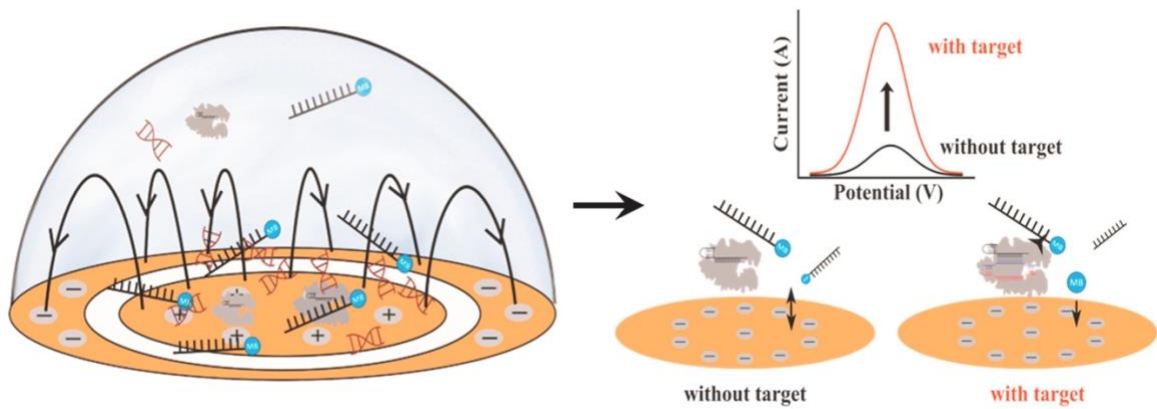


Figure 1.6 The EFE electrochemical CRISPR biosensor operates via immobilization-free detection, utilizing trans-cleavage and cis-cleavage activities of CRISPR-Cas12a. A pulsed electric field attracts nucleic acids to the positively charged working electrode surface. Electrochemical detection reveals increased current in the presence of target DNA due to reduced release of negative MB-labeled probe by Cas12a's trans-cleavage activity. Reprinted from [34]

### 1.2.5 Plasmonic-based detection

Plasmonic-based virus detection refers to the use of plasmonic nanoparticles or plasmonic structures to detect and identify viruses [35]. Plasmonic is a branch of nanophonics that involves the interaction of light with metal nanoparticles or nanostructures, typically gold or silver, leading to unique optical properties. These properties can be exploited for virus detection based on changes in the local electromagnetic field caused by viral binding events [36]. Here are a few commonly used plasmonic-based virus detection techniques.

**Localized Surface Plasmon Resonance (LSPR):** LSPR is a phenomenon that occurs when metal nanoparticles are illuminated with light at a specific wavelength, leading to the collective oscillation of the conduction electrons (plasmons) and the generation of an enhanced electromagnetic field [37]. By functionalizing the nanoparticle surface with viral receptors or antibodies, the binding of viral particles to the nanoparticles induces changes

in the LSPR signal, such as a shift in the resonance wavelength or a change in the intensity of the plasmonic peak [38]. These changes can be measured and correlated with the presence and concentration of the virus. Waitkus, et al. developed a novel localized surface plasmon resonance (LSPR) system based on the coupling of gold nano mushrooms (AuNMs) and gold nanoparticles (AuNPs) is developed to enable a significant plasmonic resonant shift [39]. This LSPR substrate is packaged in a microfluidic cell and integrated with a CRISPR-Cas13a RNA detection assay for the detection of the SARS-CoV-2 RNA targets. As shown in **Figure 1.7**, the LSPR interactions between AuNMs and AuNPs changed the local refractive index at the interface and resulted in a redshift in the absorption spectra.

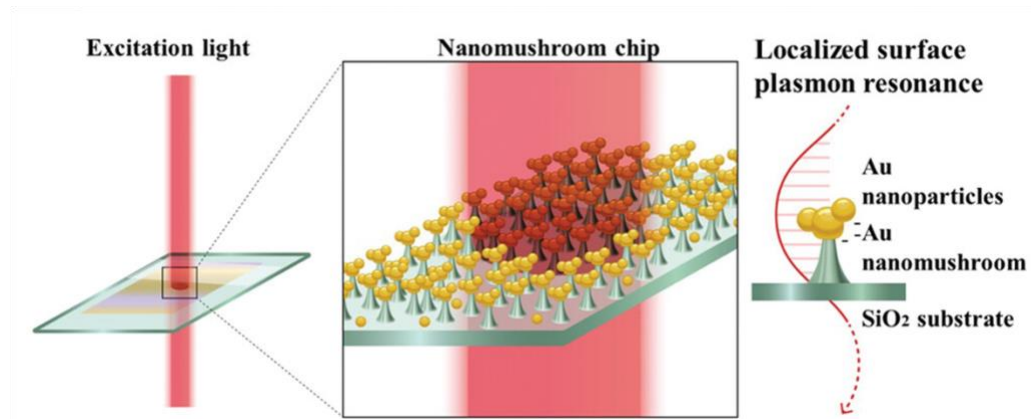


Figure 1.7 The schematic of the LSPR between AuNPs and AuNMs. Reprinted from [39]

Surface-enhanced Raman Scattering (SERS): SERS is a spectroscopic technique that exploits the plasmonic properties of metal nanoparticles to enhance the Raman scattering signal of nearby molecules [40]. In the context of virus detection, SERS-based assays can utilize specific Raman-labeled probes or antibodies that bind to viral targets. The binding event induces changes in the SERS signal, allowing for sensitive and specific detection of viruses. SERS offers multiplexing capabilities and high sensitivity, enabling the detection

of low concentrations of viral particles. Chu et al. developed an ultrasensitive protein detection platform using multiphoton Resonance Raman scattering in ZnS nanocrystals [41]. The narrow bandwidth and high stability of multiphoton Raman lines (MRLs) of ZnS, along with their strong resistance to interference, were leveraged as Raman probe signals. These features enabled reliable bio detection with high selectivity and specificity, with a detection limit of approximately 5 fM. A sandwich-structured assay protocol was designed for sensitive protein detection (**Figure 1.8**).

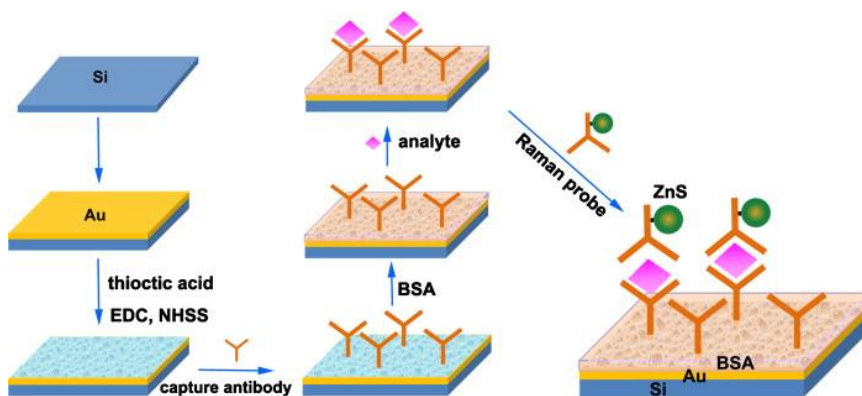


Figure 1.8 Schematic of the sandwich-structured protein detection process. Reprinted from [41]

Plasmonic-based Colorimetric Assays: Colorimetric assays are based on the observation of changes in the color of a solution or substrate upon viral binding [42]. Plasmonic nanoparticles or nanostructures are functionalized with viral receptors or antibodies, and when the target virus binds to the nanoparticles, it induces aggregation or dispersion of the nanoparticles, leading to a visible color change. This color change can be detected with the naked eye or using simple spectrophotometric techniques. Plasmonic-based colorimetric assays offer simplicity, cost-effectiveness, and ease of use for virus detection in resource-limited settings.

Plasmonic-Enhanced Fluorescence: Plasmonic nanostructures can be used to enhance the fluorescence signal emitted by fluorescent labels in virus detection assays [43]. By incorporating fluorescently labeled viral probes or antibodies onto plasmonic substrates, the proximity of the fluorophores to the plasmonic nanostructures enhances the excitation and emission rates, resulting in increased fluorescence intensity [44]. This plasmonic-enhanced fluorescence can improve the sensitivity and detection limits of virus detection methods.

In general, plasmonic-based sensors can be enhanced through various means, including utilizing intricate geometries [45], incorporating functionalized nanomaterials, integrating with conventional assays, fine-tuning surface chemistry, and employing multiple fluorophore labels [46]. These approaches offer robust characteristics such as high sensitivity, reusability, and portability. Plasmonic-based sensing has proven to be a versatile methodology for swiftly detecting a broad array of bio-targets. Notably, in virus detection, plasmonic techniques boast advantages such as high sensitivity, label-free detection, real-time monitoring, and potential for miniaturization and integration into portable devices. They have been effectively applied in detecting viruses like influenza, HIV, and SARS-CoV-2 [47]. However, optimizing assay conditions, nanoparticle properties, and surface functionalization is crucial to ensure the specificity and reliability of plasmonic-based virus detection methods.

### **1.3 Amplification-based detection**

Amplification-based detection methods are widely used in virology to identify and detect the presence of viruses in various samples [48]. These methods utilize the process of amplifying viral nucleic acids to increase their concentration, making it easier to detect and identify the virus. One of the most commonly employed amplification-based detection methods is polymerase chain reaction (PCR). PCR is a widely used technique that enables the amplification of specific DNA or RNA sequences [49]. It involves multiple cycles of heating and cooling in the presence of a DNA polymerase to facilitate the replication of targeted viral genetic material. PCR can detect even a small amount of viral genetic material, making it highly sensitive and specific for virus detection. Reverse transcription polymerase chain reaction (RT-PCR) is another widely used amplification-based technique specifically designed to detect RNA viruses [50]. It combines the reverse transcription of RNA into complementary DNA (cDNA) followed by PCR amplification of the cDNA. RT-PCR is commonly used for the detection of RNA viruses like influenza, HIV, and SARS-CoV-2 [51].

Over the past few decades, a variety of PCR kits and thermal cyclers have been developed and released to public markets [52]. For example, quantitative polymerase chain reaction (qPCR), has revolutionized viral detection with its high sensitivity and specificity [53]. qPCR utilizes DNA intercalating dyes or fluorescent probes to amplify DNA iteratively until a specific signal intensity is reached, allowing for accurate quantification of viral load in patient samples based on the cycle threshold. Recent advancements have further enhanced qPCR's capabilities, including multiplexing to detect multiple nucleic acid targets per well and introducing novel primer designs that significantly improve sensitivity.

These advancements underscore the indispensable role of qPCR in modern diagnostics, making it the gold standard for viral detection strategies. In a recent study, Jacky et al. pushed the boundaries of multiplexing in qPCR, achieving the detection of up to 20 nucleic acid targets per well using standard qPCR instrumentation [54]. Their approach involved generating distinct combined intensities for every possible combination of targets within a single well, coupled with a robust encoding system to identify the presence of each target. This innovation significantly expands the capacity for simultaneous detection within qPCR assays. In a separate development, Zhang et al. introduced a groundbreaking primer design, departing from traditional approaches [55]. They presented a novel short-stem hairpin primer with a 3' quencher modification and a fluorophore attached to the 5'-overhang. This inventive primer design resulted in a remarkable tenfold increase in sensitivity and facilitated the amplification of multiple DNA targets simultaneously. This breakthrough promises enhanced performance and efficiency in multiplexed DNA amplification assays, marking a significant advancement in molecular diagnostics.

In recent studies, many isothermal amplification techniques have been explored, such as Recombinase Polymerase Amplification (RPA) [56], Loop-mediated isothermal amplification (LAMP) [57], rolling-circle amplification (RCA) [58], and nucleic acid sequence-based amplification (NASBA) [59]. Isothermal amplification techniques are a group of molecular biology methods that allow for the amplification of nucleic acids at a constant temperature, typically around 37-65 degrees Celsius. Unlike traditional amplification methods such as PCR, isothermal amplification techniques do not require

cycling temperature changes, making them simpler and more accessible for various applications, including virus detection, diagnostics, and research [60].

LAMP is a robust and highly specific amplification method that can amplify DNA or RNA targets. It utilizes a combination of four to six primers that recognize multiple regions of the target sequence, resulting in the rapid and exponential amplification of the target nucleic acid [61]. LAMP reactions can be visually detected by the turbidity of the reaction mixture or by the addition of fluorescent dyes that emit visible light upon amplification.

**Figure 1.9.** shows the LAMP mechanism, it usually uses 4-6 primers recognizing 6-8 distinct regions of target DNA for a highly specific amplification reaction. The LAMP method employs a single strand of DNA shaped like a dumbbell with loops at both ends. This starting material is used to initiate a cycle of amplification reactions. DNA having an inverse structure relative to the starting material is produced, and the starting material is formed again by the same reaction. This cycle produces amplified DNA products that are connected to an inverted repeat structure at the amplified region. The amplified products again pass through repeated elongation reactions, which generate amplified DNA products of various stem lengths.

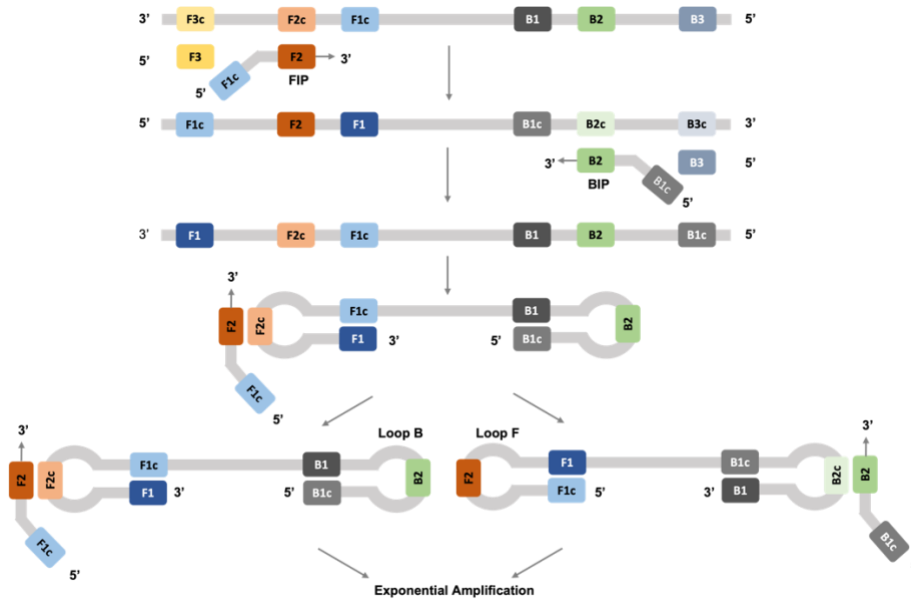


Figure 1.9 Schematic representation of the LAMP mechanism. Design of the primers for LAMP. Forward inner primer (FIP): F2 sequence with F1c sequence at the 5' end. Backward inner primer (BIP): B2 sequence with B1c sequence at the 5' end. Outer primers are designed at the regions of F3 and B3.

RPA is an isothermal amplification technique that uses a combination of recombinase enzymes and a strand-displacing DNA polymerase [62]. The recombinase enzymes facilitate the binding of primers to the target DNA, and the polymerase extends the primers, leading to the exponential amplification of the target sequence. RPA is a very fast technique, typically providing results within 10-30 minutes. This is in contrast to PCR, which requires multiple temperature cycles and can take several hours to complete. RPA reactions typically operate at a constant temperature of around 37-42 degrees Celsius and can be detected using various methods, including lateral flow strips [63], fluorescent probes [56], or turbidity measurements [64]. Many applications have been developed for the virus detection. Bao, et al. developed a FAST (funnel adapted sensing tube) chip to detect the SARS-CoV-2 virus (**Figure 1.10**) [65]. First use RPA to amplify the target, and then combining with the CRISPR Cas12 to detect the SARS-CoV-2 virus, which is power-free and pipette-free nucleic acid detection. Make it easy to use in point-of-care detection.

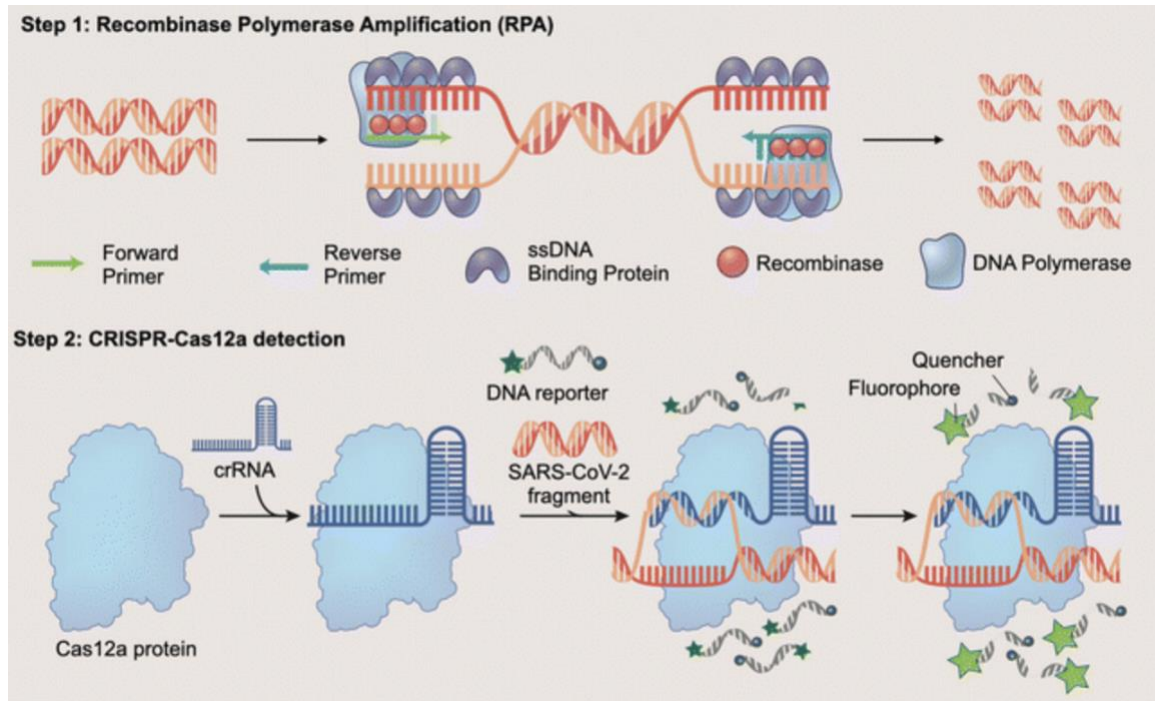


Figure 1.10 Principle of SARS-CoV-2 fragment detection using RPA amplification and CRISPR cleavage. Reprinted from [65]

In summary, while the reliance on thermal cycling machines in PCR technologies poses logistical challenges for on-site diagnostics, the emergence of isothermal amplification techniques has garnered significant attention within the field. Isothermal amplification methods offer distinct advantages over traditional PCR, primarily due to their ability to operate at a constant temperature. This feature simplifies instrumentation requirements, accelerates amplification times, and facilitates the execution of reactions in portable and field settings. The adoption of isothermal amplification techniques represents a paradigm shift in molecular diagnostics. Notably, these methods have broad applications across various domains, including infectious disease diagnostics, point-of-care testing, environmental monitoring, and research endeavors. By eliminating the need for thermal cycling, isothermal amplification streamlines the diagnostic process, enabling rapid and

efficient detection of target nucleic acids. In many cases, isothermal amplification is also combined with CRISPR technology to achieve more sensitive, specific, and simplified nucleic acid detection [66].

Amplification-based detection methods, regardless of whether they employ traditional PCR or isothermal techniques, have revolutionized virus detection and diagnosis. Their inherent high sensitivity and specificity empower clinicians and researchers to identify even minute concentrations of viral genetic material accurately. This capability is particularly crucial in the context of infectious disease surveillance, allowing for the early detection of pathogens and the prompt implementation of intervention and control measures. Overall, the integration of amplification-based detection methods into diagnostic protocols has significantly advanced our capacity to combat infectious diseases. By providing clinicians and public health authorities with timely and accurate information, these techniques play a pivotal role in mitigating the spread of pathogens and safeguarding public health.

#### **1.4 Outline and Contributions**

This introduction **Chapter 1** reviews the background, current status and potential power of the different kind of biosensors. In conclusion, two main types of nucleic acid assays are described, one based on CRISPR technology and the other based on amplification methods. CRISPR-based nucleic acid assays offer excellent specificity, rapid detection within minutes to hours, and the ability to perform single-step assays, reducing time and resource requirements. They enable multiplexing, targeting multiple nucleic acid

sequences simultaneously, and can be conducted with minimal equipment, making them suitable for resource-limited settings. Amplification methods, such as PCR and LAMP, offer high sensitivity, enabling the detection of low concentrations of nucleic acids even with limited sample volumes. They also enable quantitative analysis, facilitating accurate measurement of gene expression levels or pathogen load.

**Chapter 2** presents a novel nanopore platform for high-throughput single-molecule sensing, utilizing gold nanoparticles (AuNPs) to enhance the detection of viral RNA. A sensitive CRISPR-Cas13a assay is employed for recognizing SARS-CoV-2 target RNA. After magnetic bead separation, the CRISPR-Cas13 cleaved AuNPs are introduced into a solid-state nanopore reader for detection. This combination of a highly specific CRISPR assay with a highly sensitive nanopore platform represents a significant advancement towards portable, rapid, and highly quantitative nucleic acid detection technology in point-of-care (POC) settings.

**Chapter 3** shows a novel integration of CRISPR-Cas assays with electrochemical biosensors provides a multiplexing and amplification-free diagnostic platform, overcoming limitations associated with conventional techniques. The presented dual-function biosensor, utilizing aerosol inkjet printing and HRP-labeled CRISPR-Cas13a assay, demonstrates excellent sensitivity and specificity for SARS-CoV-2 detection, offering a valuable tool for point-of-care diagnostics of infectious diseases.

**Chapter 4** reveals a self-powered digital nanofluidic chip (dChip) offers nano-liter loop-mediated isothermal amplification (LAMP) for rapid and quantitative genetic material detection. Utilizing a vacuum lung system, our chip digitizes samples into nanoliter wells, serving as individual reactors for on-site nucleic acid quantification. With a proof-of-concept demonstration for Norovirus detection, our dChip exhibits superior user-friendliness, portability, and robustness, promising improved POC diagnostics and advancing public health efforts against emerging viruses.

**Chapter 5** presents a digital nanofluidic chip that further advance nucleic acid amplification by distributing target molecules into small pores for absolute quantitative analysis. Our study presents a novel energy transfer-labeled oligonucleotide probe and digital warm start assay within a nanofluidic chip for highly sensitive and quantitative detection of HPV 16, offering a promising solution for precise diagnosis of sexually transmitted infections in hospital or point-of-care settings.

Finally, **Chapter 6** reviews the biosensing platform from fundamental principles to applications and proposes future directions on what else these biosensing platforms can bring us and what else we can learn from them. We foresee that the introduction of artificial intelligence will revolutionize biosensors in the coming era of big data.

## **Chapter 2. Nanopore sensing and recent advances in nanopore research related to solid-state nanopores**

### **2.1 Introduction**

Nanopore sensing is a powerful technique that utilizes nanometer-sized pores to detect and analyze molecules such as DNA, RNA, proteins, and small molecules [67]. The basic principle involves passing these molecules through a nanopore, typically made from a biological membrane protein or solid-state materials, and measuring changes in electrical current or other physical properties as the molecules interact with the pore [68]. Solid-state nanopores, in particular, offer several advantages over biological nanopores, including greater stability, easier fabrication, and the ability to customize pore geometry and surface properties. Recent advances in solid-state nanopore research have focused on enhancing the sensitivity, selectivity, speed, and scalability of nanopore sensing platforms [69].

Some recent advances in solid-state nanopore research include improved sensitivity and resolution: researchers have been working on reducing the size of solid-state nanopores to enhance sensitivity and resolution [70]. This enables the detection and discrimination of smaller molecules and finer structural features within biomolecules; Functionalization and Surface Modifications: Surface modifications of solid-state nanopores can enhance their selectivity towards specific analytes or enable the detection of molecules with greater precision [71]. Functionalization with biomolecules, polymers, or nanoparticles can impart additional functionalities such as molecular recognition or signal amplification [72]; Integration with Advanced Electronics: Integration of solid-state nanopores with advanced electronic devices allows for real-time monitoring and analysis of molecular interactions.

This includes the development of integrated circuits, field-effect transistors, and other electronic components that interface directly with nanopore sensors [73]; Single-Molecule Analysis: Solid-state nanopores enable the direct detection and analysis of individual molecules in real-time, providing insights into molecular dynamics, conformational changes, and interactions at the single-molecule level [74]. This capability is invaluable for applications such as DNA sequencing [75], protein profiling [76], and drug screening [77]; Multiplexed Detection: Advances in nanopore array technology enable parallel analysis of multiple nanopores, allowing for high-throughput screening of biomolecules and simultaneous detection of different analytes [78]. This improves the efficiency and scalability of nanopore-based sensing platforms; Applications in Biomedicine and Point-of-Care Diagnostics: Solid-state nanopores hold great promise for applications in biomedicine, including rapid and portable diagnostic devices for detecting pathogens, biomarkers, and genetic variations [79]. The ability to perform label-free, rapid, and sensitive measurements makes solid-state nanopores attractive for point-of-care diagnostics and personalized medicine.

Overall, solid-state nanopore research continues to push the boundaries of molecular sensing and analysis, with significant potential impact across various fields including biotechnology, healthcare, environmental monitoring, and beyond. As researchers continue to innovate and refine nanopore-based technologies, we can expect further advancements in sensitivity, specificity, and practical applications of this versatile sensing platform.

## **2.2 Working principle of the nanopore sensor.**

Nanopore-based sensors have become an important tool for single-molecule analysis, including nucleic acids, proteins, sugars, and a large number of biomolecules [80]. The principle of conventional nanopore detection is resistive pulse sensing, which measures the temporal fluctuation signal of the ionic current passing through the pore. By characterizing the current signal, such as duration, signal amplitude, and signal frequency, we can obtain information about the analyte, such as its size, shape, etc. **Figure 2.1** illustrates the working principle of a nanopore sensor [69].

Nanopore sensor devices are typically two reservoirs filled with an electrolyte (usually a buffered salt solution, e.g., potassium chloride) separated by a thin, impermeable membrane and connected by a nanopore. A constant voltage bias is applied at both ends of the nanopore through electrodes, resulting in a steady-state ionic current flowing through the nanopore. The ionic current either decreases due to the presence of an analyte that hinders the access of the ions to the nanopore volume or increases when metal nanoparticles are passing through the nanopore and enhance the ionic current due to the high conductivity.

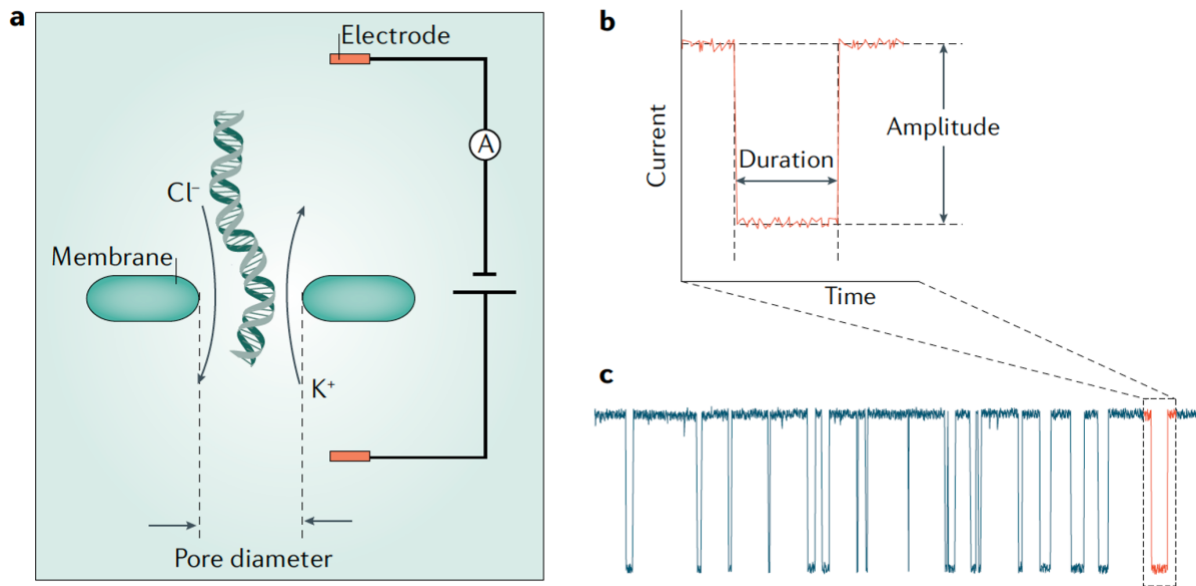


Figure 2.1 Illustrates the working principle of a nanopore sensor. a. The diagram of nanopore sensing. b. The signal analysis such as duration, signal amplitude, and signal frequency. c. Typical nanopore signal diagram. Reprinted from [69]

The main point of the single molecule approach is that the space and time of the individual analytes must be limited during the measurement. Ideally, the size of the sensing volume should be comparable to the size of the analyte to achieve the sensitivity of a single molecule. In a nanopore, the molecules are confined to a space of comparable size. This places very high demands on the fabrication of the nanopore. On the one hand, the diameter of the nanopore should be similar to that of the analyte in order to facilitate the detection of a significant signal. On the other hand, the thickness of the nanopore should be as small as possible, which allows for maximizing the detected signal. Recent advances in materials science and surface chemistry have led to a wide range of different methods for processing and fabricating nanopores, which make the devices not only more robust and sensitive but also greatly increase the range of detection [81]. **Figure 2.2** shows a typically fabricated method of solid nanopores. Silicon nitride as a membrane for solid nanopores. PECVD

method to coating the silicon. Wet etching for silicon, dry etching for silicon dioxide, helium ion etching for silicon nitride layer [82].

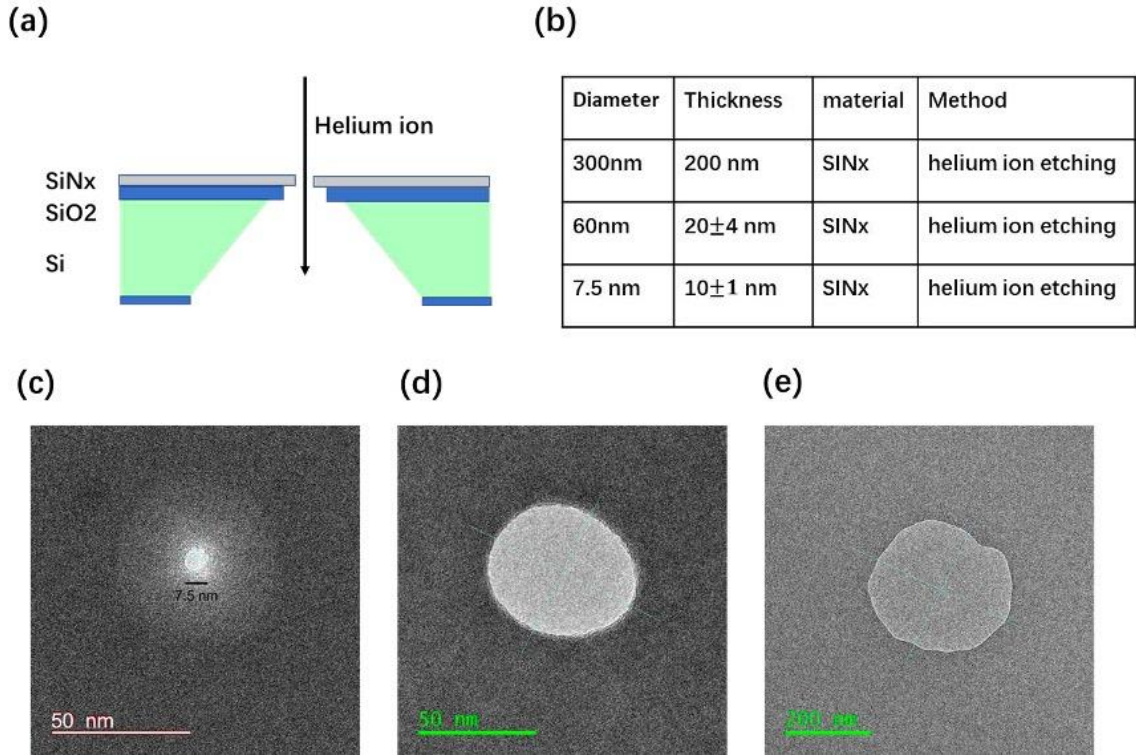


Figure 2.2 Typical fabrication methods for solid nanopores. (a) Diagram of nanopore fabrication. (b) Relationship between nanopore diameter and thickness using helium ion etching method. (c)(d)(e) TEM images for different diameters nanopore.

### 2.3 Selective sensing using molecular probes

In recent years, solid-state nanopore sensing has attracted increasing attention in detecting single molecules with many advantages, including controllable feature size, high sensitivity, simple readout, and label-free electronic sensing [83]. The technology has been applied to many areas such as DNA sequencing [84], protein detection [85], nanoparticle separation [86], and energy conversion [87]. Stefan et al. demonstrate that using the solid-state nanopore can detect the local protein structures along the DNA [88]. In **Figure 2.3**,

DNA was coated with RecA protein. When the DNA translocates the nanopore, it shows a different signal intensity. The current blocking time is also different for different molecules.

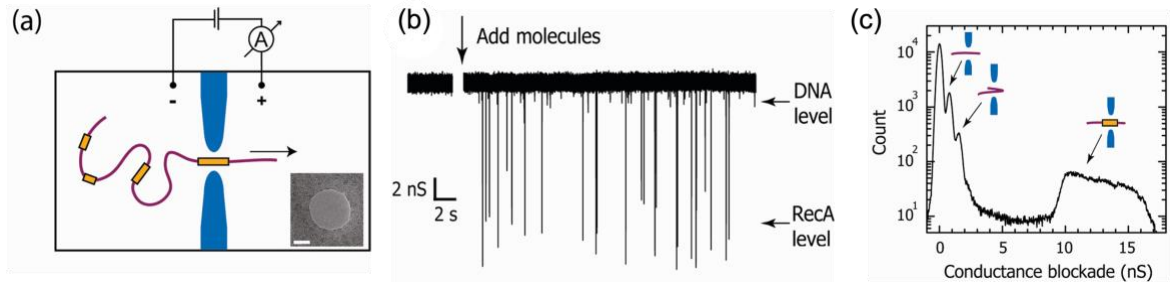


Figure 2.3 Detection of local protein structures along DNA using solid-state nanopores. (a) Schematic layout of the experiment. DNA molecules (purple) are locally coated with RecA proteins (orange). The inset shows a TEM of a 30 nm diameter nanopore. (b) Current trace before and after addition of the molecules. (c) Conductance histogram of all events. Reprinted from [88]

CRISPR assays have shown outstanding competence for highly specific nucleic acid targeting and have been used in various nanopore sensing platforms. For instance, Nouri et al. developed solid-state CRISPR-Cas12a-assisted nanopores (SCAN) to specifically detect the HIV-1 (**Figure 2.4**). The glass nanopore sensor is effective in monitoring the cleavage activity of the target-DNA-activated Cas12a [89]. In addition, Nicole et al. demonstrated the use of a highly specific dCas9 probe to create unique barcodes on DNA that nanopore sensors can read. Multiple dCas9 probes are available to create characteristic structural patterns on DNA. These sequence-specific structures simultaneously recognize different DNA targets in a mixture, demonstrating an important step toward rapid DNA identification [90].

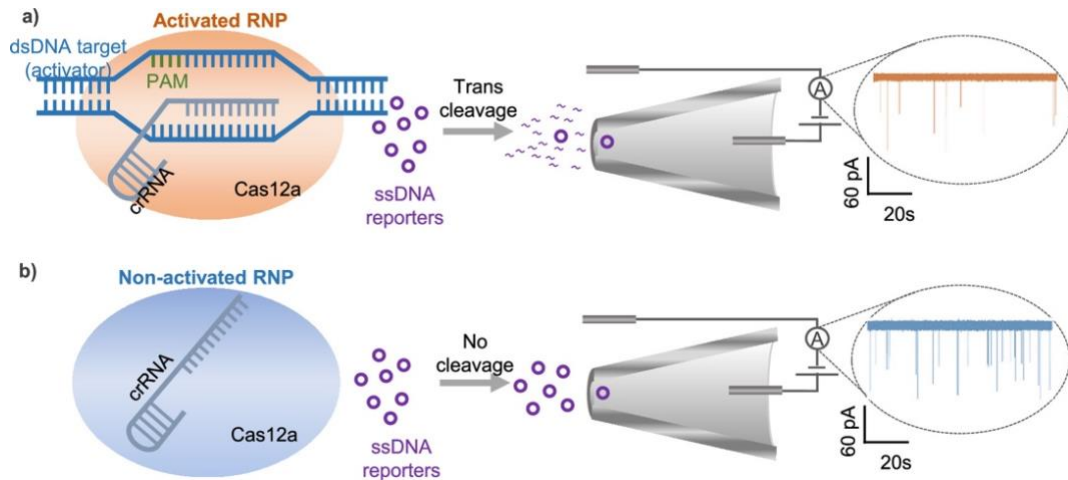


Figure 2.4 Schematic of solid-state CRISPR-Cas12a-assisted nanopore (SCAN) sensor. (a) Positive case, the trans-cleavage activity of the Cas12a after activation causes degradation of the circular ssDNA reporters, resulting in reduced reporter event rate through the nanopore. (b) Negative case, the Cas12a is not activated in the absence of target dsDNA and thus the ssDNA reporters are not cleaved. The nanopore event rate remains high. Reprint from [89]

## 2.4 Gold Nanoparticle-Labeled CRISPR-Cas13a Assay for nanopore virus detection

This work aims to develop a nanopore array platform for high throughput single molecule sensing. We leverage the strong ionic signal pulse caused by gold nanoparticles (AuNPs) in the detection of viral RNA. A sensitive CRISPR-Cas13a assay has been developed to recognize the SARS-Cov-2 target RNA. After magnetic bead separation, the CRISPR-Cas13 cleaved AuNPs are introduced into a solid-state nanopore reader for detection. Our combination of a highly specific CRISPR assay and a highly sensitive nanopore platform has enabled our results to be an important step forward in the implementation of portable, rapid, and highly quantitative nucleic acid detection technology in the POC environment. In addition, it is also important to understand the physics of the particles translocation process in a complex system, where electrohydrodynamic (electrophoresis, electroosmosis), photon-induced thermal effects are involved.

## **AuNP-labeled CRISPR-Cas13a nucleic acid assay for solid state nanopore sensing.**

The protocol we developed is AuNPs labeled CRISPR-Cas13a assay for the virus detection. Gold nanoparticles are one of the most commonly utilized nanomaterials due to their stability and optical properties. Gold nanoparticles are readily conjugated to antibodies and other proteins due to the affinity of sulfhydryl (-SH) groups for the gold surface, and gold-biomolecule conjugates have been widely incorporated into diagnostic applications, where their bright red color is used in home and point-of-care tests such as lateral flow assays. And Gold nanoparticles have many properties that can make them have many advantages in biosensors with easily functionalized surfaces, and surface plasmon resonance properties. In the AuNP-labeled CRISPR-Cas13a nucleic acid assay, different virus concentrations result in different amounts of reporter RNA cleavage, and after the separation of magnetic spheres, the reporter RNA of label AuNP will be released in the supernatant, and the virus can be quantified by colorimetric reaction and nanopore reader. The nanopore reader is a single-molecule pass-through detection device that greatly improves detection limits.

### **Materials and reagents.**

#### **2.4.1 AuNP-labeled CRISPR-Cas13a nucleic acid assay.**

CRISPR Lbu-Cas13a Trans-Cleavage: CRISPR-Cas13a and guide RNA were first mixed in the following order: RNase-free water (22  $\mu$ l), 6  $\mu$ l of 5 $\times$  Standard (STD) Buffer ( $250 \times 10^{-3}$  M KCl,  $100 \times 10^{-3}$  M HEPES,  $25 \times 10^{-3}$  M MgCl<sub>2</sub>,  $5 \times 10^{-3}$  M DTT, 25% Glycerol, pH 6.8), 1.67  $\mu$ l of Lbu Cas13a in-stock solution ( $18 \times 10^{-6}$  M), 0.33  $\mu$ l of guide RNA in-stock solution ( $100 \times 10^{-6}$  M) to a total volume of 30  $\mu$ l. The mixture was incubated at

37 °C for 2 min followed by 8 min at room temperature, then put on ice for later use. Two microliters of the Cas13a-guide RNA complex were then added into 11 µl of RNase-free water, 4 µl of 5× STD buffer, 2 µl of RNA target with different concentrations, and 1 µl of the biotin-fluorescein ssRNA reporter ( $10 \times 10^{-6}$  M) to a total volume of 20 µl. The reaction was incubated at 37 °C for 30 min.

**Immobilizing RNA Reporters onto AuNPs:** Streptavidin-coated AuNPs with a diameter of 40 nm ( $1.1 \times 10^{-6}$  M) were purchased from nano Composix Inc. The stock solution was concentrated by a centrifuge process: 500 µL of stock AuNPs was added in a microcentrifuge tube and spun for 8 min (8000 rpm) and then 400 µl of the supernatant was removed to achieve 100 µl ( $5.5 \times 10^{-3}$  M) of AuNPs. Ten microliters of the concentrated AuNPs was taken and added into 20 µl of Cas13-guide RNA–RNA reporter probe mixture. The sample was incubated on a rotary mixer at room temperature for 15 min. **Magnetic Bead Isolation:** Dynabeads MyOne Streptavidin C1 with a diameter of 1 µm ( $10 \text{ mg ml}^{-1}$ ) were purchased from Thermo Fisher Scientific Inc. Biotinylated anti-fluorescein antibody ( $1 \text{ mg ml}^{-1}$ ) was purchased from Vector Laboratories Inc. Before conjugation, streptavidin-coated magnetic beads were washed three times with 1× PBS buffer. Ten microliters of biotinylated anti-fluorescein antibody ( $1 \text{ mg ml}^{-1}$ ) were added to the 10 µl Dynabeads solution, followed by incubation at room temperature using a rotary mixer for 30 min. After incubation, the beads were washed three times with 1× PBS buffer to remove any unbound anti-fluorescein antibody. Thirty microliters of AuNPs labeled Cas13a reaction products from the last step were then added. The reaction tube was incubated at 37 °C for 30 min. After the reaction, the magnetic beads were isolated by a magnet and left the supernatant for nanopore experiments.

SiNx Nanopore Fabrication and Preparation: The 90 nm diameter SiNx nanopore chips were provided by Norcada Inc. Before each experiment, the nanopore chip was sonicated for 5 min to remove the debris. Deionized water and isopropyl alcohol were used to wash the chip and the sample was dried with high-pressure gas. Nanopore Sensing and Data Analysis: The portable nanopore reader (100 kHz bandwidth) was purchased from Elements Inc. The nanopore flow-cell was constructed with two translucent parts made by Delrin [PolyOxyMethylene (POM)]. Each part had a channel and a reservoir to hold the electrolyte. The two translucent parts sandwiched the nanopore chip in the middle and then were assembled with a  $15 \times 25 \text{ mm}^2$  PCB board with integrated Ag/AgCl electrodes. Two microliters AuNPs samples was added into 90  $\mu\text{l}$  of buffer (1 M KCl) on each side of the reservoirs. Constant voltage ( $-700 \text{ mV}$  to  $700 \text{ mV}$ ) was applied across the portable nanopore reader in this study. The Elements data reader collected the current data with a frequency of 20 000 Hz. The Elements data analyzer (data analysis program developed by the Elements. Inc) and a customized Python program was used to extract the single molecule translocation events, the ionic current dip, and the molecule dwell time. Specifically, the data analyzer detected the events by setting the baseline threshold, which was the average value of the noise floor, and the high threshold, which was at least five standard deviations ( $5\sigma$ ) above the noise floor. The dwell time of the events that were lower than 0.1 ms or longer than 100 ms was considered not regular dwell time, and the events were discarded. TEM Imaging: JEOL (JEM-2010, Japan) was used to image the AuNPs (HV = 200.0 kV, direct Mag = 6 k  $\times$ ).

#### **2.4.2 Gold nanoparticles labeled CRISPR Cas13a virus detection results.**

## Characterization of Solid Nanopore sensing

The approach for solid-state nanopore sensing is shown in **Figure 2.5**. A SiN<sub>x</sub> nanopore chip is sandwiched between two microfluidic reservoirs shown in blue. Two AgCl electrodes are immersed in the reservoirs on both sides, and a constant voltage (−700 to 700 mV) is applied across the nanopore, causing a steady-state ionic-current flux at the picoamp (pA) level through the nanopore. The translocation of the free AuNPs changes the ionic current and is detected by the nanopore reader shown in the diagrams to the right.

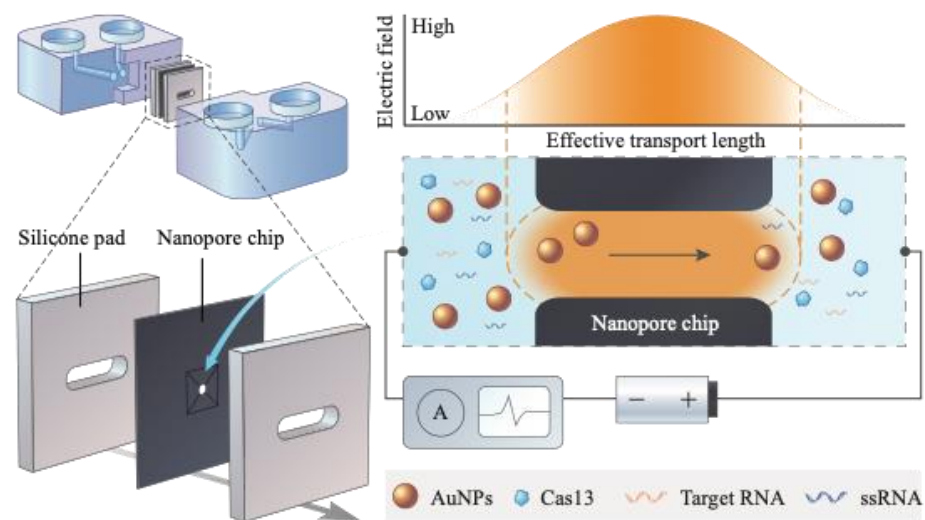


Figure 2.5 Schematic of the solid-state nanopore sensing platform. The nanopore chip is sandwiched between two microfluidic reservoirs (blue) and silicone pads. The trans-cleavage of CRISPR-Cas13a releases the gold nanoparticles to pass through the solid-state nanopore and changes the ionic current. Reprinted from [72]

The free-standing SiN<sub>x</sub> membrane (thickness:  $20 \pm 3$  nm) sits on a 200  $\mu\text{m}$  thick silicon substrate with a frame size of  $5 \times 5$  mm. A 60 nm thick SiO<sub>2</sub> layer was deposited between the silicon substrate and the SiN<sub>x</sub> membrane to reduce the electrical noise. The nanopore (diameter: 90 nm) was prepared with a helium ion microscope (**Figure 2.6a**), the pore is

visible as a round opening of  $\approx 90$  nm by transmission electron microscopy (TEM). Before introducing AuNPs into the chip, the open-pore current in 1 M KCl solution was analyzed to characterize the nanopore chip and the nanopore reader. As shown in **Figure 2.6b**, a linear relationship between the ionic current and the applied voltage in the range of  $-400$  to  $400$  mV was recorded ( $R^2 = 0.999$ ) in 1 M KCl with a corresponding pore conductance  $G$ , calculated to be  $732.1$  nS. The ionic conductance through an open solid-state nanopore can be calculated by

$$G_0 = \sigma \left[ \frac{4l}{\pi d^2} + \frac{1}{d} \right]^{-1}, \quad (1)$$

where  $\sigma$  is the solution conductivity,  $l$  is the membrane thickness, and  $d$  is the nanopore diameter.

Here,  $l$  is  $20$  nm and  $\sigma$  is  $10.5$  S/m in 1 M KCl at  $23^\circ\text{C}$ . The calculated nanopore diameter is  $89.5$  nm, which is consistent with the TEM characterization.

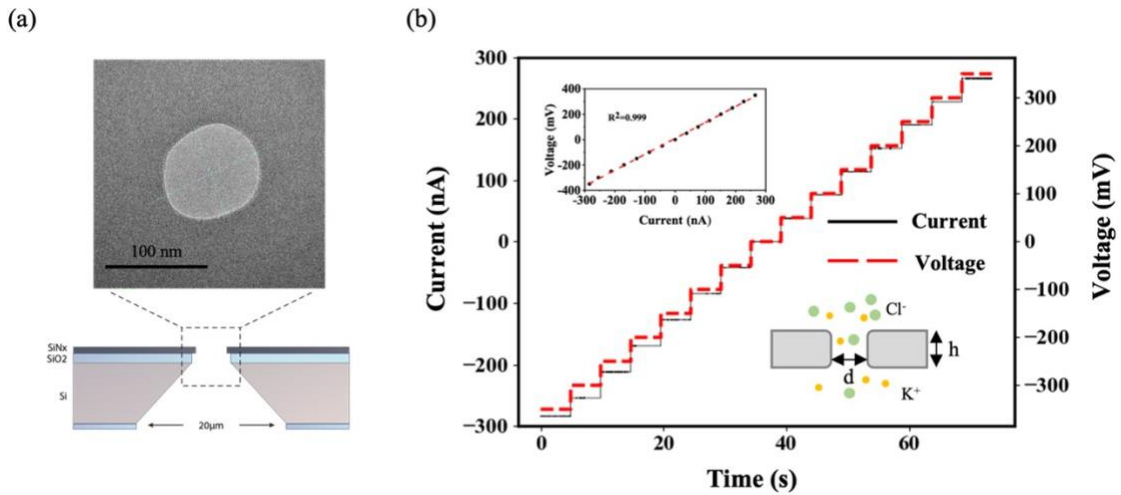


Figure 2.6 (a) TEM image of the nanopore chip with a pore diameter of 90 nm with diagram showing cross-section. (b) A representative current–voltage (I–V) calibration curve of a  $\sim 90$  nm nanopore in 1 M KCl. The inset shows the linear fits yield a conductance of  $732.1$  nS and the diagram of KCl buffer passing through the nanopore. Reprinted from [72]

### Strategy for AuNPs labeled CRISPR Cas13a virus detection

The schematic of the AuNP-Cas13 detection process is shown in **Figure 2.7**. Lbu-Cas13a protein and crRNA are premixed to form a Cas13a:crRNA complex. In this case, the guide RNA is specific for a nucleotide sequence within the S reading frame of SARS-CoV-2. Then, biotin-FAM-labeled ssRNA probes are introduced into the mixture (step 1). Next, Streptavidin-coated AuNPs are added to the assay (step 2). The presence of the target RNA (SARS-CoV-2) activates the Cas13a:crRNA complex, cleaving the ssRNA probes in the solution. In the absence of the target RNA, the non-cleaved ssRNA probes are captured by anti-FAM coated magnetic beads (step 3) and isolated by a super magnet (step 4). Since ssRNA probe cleavage is correlated to the target concentration, the amount of AuNPs presented in the supernatant can be used for quantitative RNA target sensing.

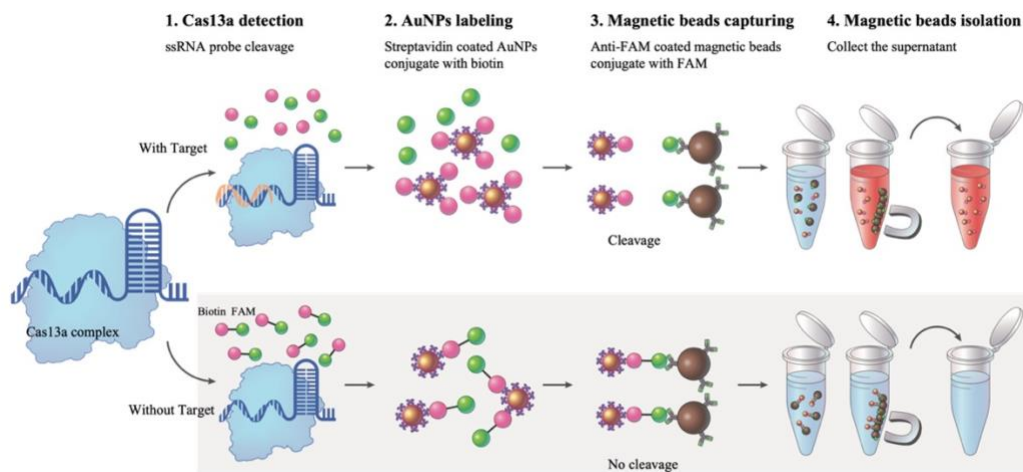


Figure 2.7 (a) Schematic of the AuNP-Cas13-based nucleic acid detection strategy: Step 1. Cas13a/crRNA complex cleavage of ssRNA probes; Step 2. Streptavidin-coated AuNPs bind biotin-labeled ssRNA probes. Step 3. FAM-labeled ssRNA probes bind anti-FAM coated magnetic beads; Step 4. Magnetic bead isolation of non-cleaved ssRNA. Reprinted from [72]

The target and the guide RNA sequences are listed in **Figure 2.8**. The SARS-CoV-2 target (703 nts) was selected from the plasmid pUC57-SARS-CoV-2 (spike S gene). A 20-mer guide RNA was selected to recognize a 20-nt sequence within the SARS-CoV-2 target.

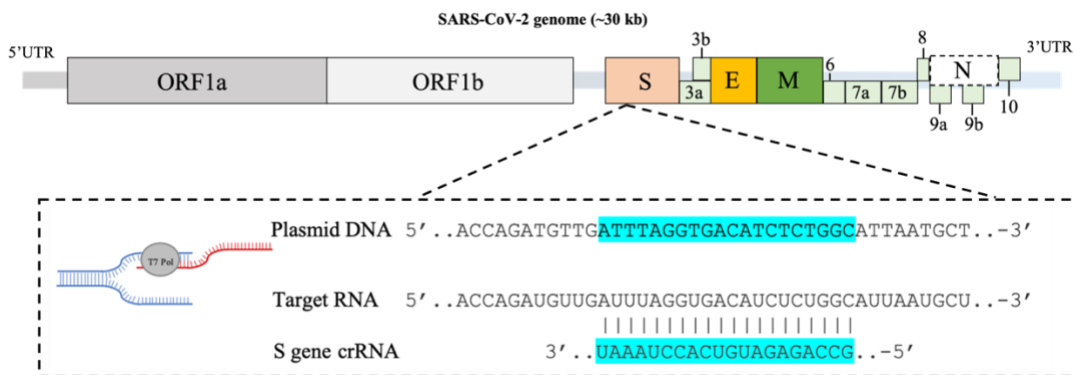


Figure 2.8 The SARS-CoV-2 gene locus, target site, and the guide RNA sequence. Reprinted from [72]

The photographs of the cleaved products contained within microtubes are shown in **Figure 2.9 a(i)**. The red color is observed for positive samples with a concentration above  $0.1 \times 10^{-9}$  M. On the other hand, for negative samples, the collected supernatants do not show any color, regardless of the input target concentration (**Figure 2.9 a(ii)**). The results were further confirmed by TEM imaging (**Figure 2.9 b**). For the  $100 \times 10^{-9}$  M positive sample (**Figure 2.9b(i)**), clusters of the AuNPs are easily observed, indicating that the ssRNA probes were cleaved, leaving the AuNPs in the supernatant. In the negative sample (**Figure 2.9b(ii)**), it was extremely difficult to observe AuNPs with TEM, indicating that most AuNPs are conjugated on the magnetic beads.

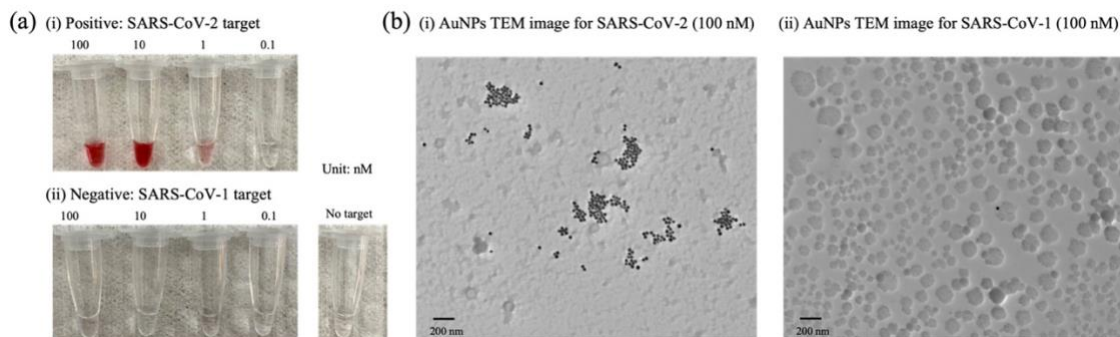
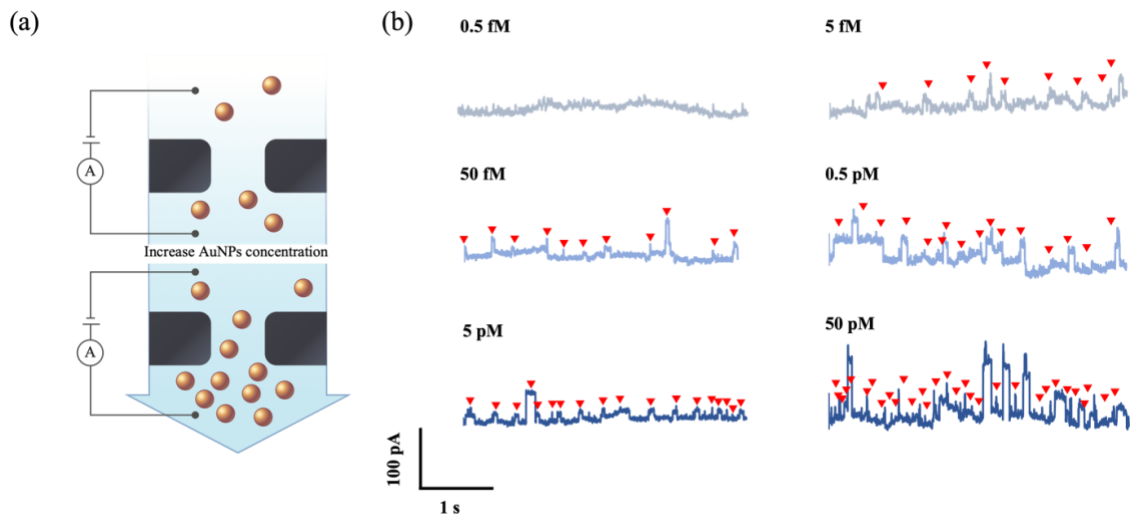


Figure 2.9 The SARS-CoV-2 gene locus, target site, and the guide RNA sequence. (a) Images of the AuNPs containing the indicated concentrations of (i) SARS-CoV-2 target RNA (positive) and (ii) SARS-CoV-1 target RNA (negative). (b) TEM images of the cleaved products of (i) 100 nM of SARS-CoV-2 target RNA and (ii) 100 nM of SARS-CoV-1 target RNA. Scale bars are 200 nm. Reprinted from [72]

### Identification of single AuNPs

To validate that the nanopore event rate can be used as a quantitative readout for the AuNP and thus target RNA abundance, we performed nanopore counting with serially diluted Streptavidin-coated AuNPs in 1 M KCl solution (**Figure 2.10a**). Typical current traces of AuNPs with varying concentrations ( $0.5 \times 10^{-15}$  to  $50 \times 10^{-12}$  M) translocated through a 90 nm nanopore are shown in **Figure 2.10b**. The upward pulses along the time trace indicates that the negatively charged AuNPs bring new ions into the nanopore, resulting in a temporary increase in conductance. The nanopore chip is small in size and occupies the largest resistance component in the whole circuit. Therefore, when the original solution (buffer solution) is replaced by a more conductive solution, the resistance of the circuit would decrease, resulting in the current increase. The current increases when adding more AuNPs to the solution since the conductivity of the AuNPs is higher than the buffer solution. A quick glance at these traces reveals that the events occur more frequently with the increase of the AuNPs concentration.



The extracted event rate exponentially increases with the AuNPs concentration ( $R^2 = 0.9106$ ), as shown in **Figure 2.11a**. The corresponding histogram of the current increase ( $\Delta I$ ) versus the AuNPs concentration is shown in **Figure 2.11b**. The  $\Delta I$  value is  $320.5 \pm 132.1$  pA for  $50 \times 10^{-15}$  M AuNPs,  $395.5 \pm 90.3$  pA for  $0.5 \times 10^{-12}$  M AuNPs,  $454.0 \pm 171.7$  pA for  $5 \times 10^{-12}$  M AuNPs, and  $454.3 \pm 197.5$  pA for  $50 \times 10^{-12}$  M AuNPs, indicating that the  $\Delta I$  increases with AuNP concentration.

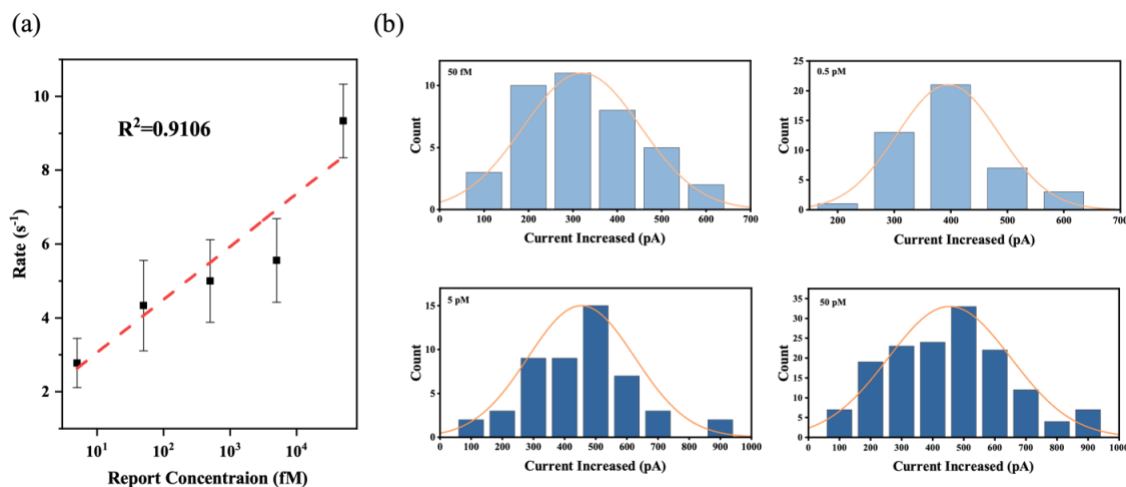


Figure 2.11 (a) Nanopore event rate versus AuNP concentration ranging from 0.5 fM to 50 nM. (b) The histograms of the distribution of current increase corresponding to the translocations of AuNPs with various concentrations, fitted to Gaussian curves. Reprinted from [72]

To further explore the current variation of the AuNPs, we extracted the dwell time and the distribution of event charge deficit (ECD) for the AuNPs with various concentrations (Figure 2.12). The calculated ECD value does not change with the different concentrations of the AuNPs.

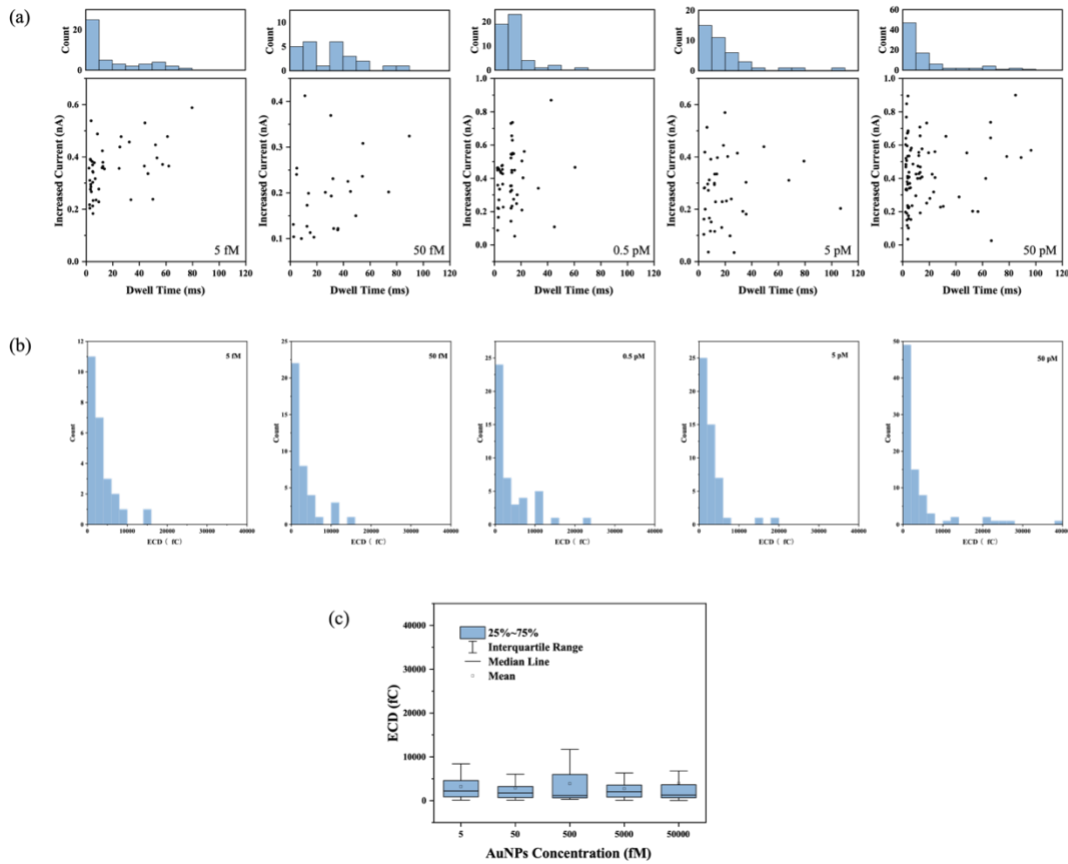


Figure 2.12 (a) Scatter plots show increased current vs. dwell time for different concentrations of AuNPs. (b) ECD distribution with different concentrations of AuNPs. (c) Box plot of the event charge deficits (ECD) for various concentrations of AuNPs. Reprinted from [72]

## Nanopore molecular accounting for virus detection

After verifying the relationship between the AuNPs and the nanopore event rate, RNA sensing was performed by varying the RNA concentration from  $0.1 \times 10^{-12}$  to  $10 \times 10^{-9}$  M while setting the AuNPs concentration at  $5.5 \times 10^{-9}$  M. The current traces were recorded using a single applied voltage (700 mV) for 5 min after the signal appeared. Multiple specific periods were analyzed for each concentration. **Figure 2.13a** shows the detected current trace of AuNPs with various SARS-CoV-2 RNA target concentrations and the corresponding ion current versus the observed translocation time. More current traces of AuNPs were detected with increasing target RNA concentrations. The current trace of the AuNPs for negative control (SARS-CoV-1) is shown in **Figure 2.13b**. A flat control signal was detected at most concentrations, and we only found a very low frequency of AuNPs in the  $10 \times 10^{-9}$  M negative sample.



Extrapolating the positive measured rate and comparing it with the negative control suggests a detection limit of  $\approx 50 \times 10^{-15}$  M.

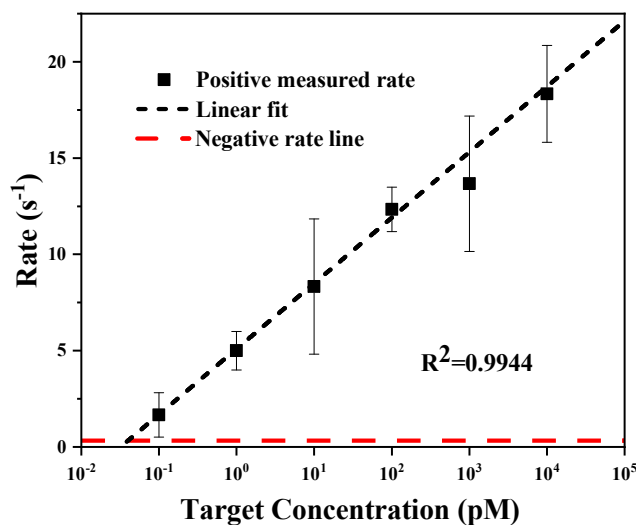


Figure 2.14 Nanopore event rate versus RNA concentration (50 fM to 50 nM): SARS-CoV-2 (black); SARS-CoV-1 (red). ( $R^2=0.9944$ ) Reprinted from [72]

### 2.4.3 Discussion

The CRISPR-enabled solid-state nanopore sensing established here shows great sensitivity and specificity for viral RNA sensing. Without front-end target amplification, a detection limit of  $50 \times 10^{-15}$  M (30 000 copies  $\mu\text{l}^{-1}$ ) is achieved by the unique trans-cleavage property of the CRISPR-Cas13a assay. This detection limit is close to the required sensitivity for rapid screening of SARS-CoV-2 [12]. Moreover, our protocol can be integrated with established reverse transcription-loop-mediated isothermal amplification (RT-LAMP) and reverse transcription-recombinase polymerase amplification (RT-RPA) methods to extend the detection limit further by several orders of magnitude [9], [11].

Our solid-state nanopore sensing platform requires only a smartphone-sized nanopore reader designed for POC applications. Simple and inexpensive, CRISPR-based lateral flow strips have been developed to diagnose SARS-CoV-2, but these tests cannot provide quantitative results. On the other hand, quantitative polymerase chain reaction (qPCR) is ultra-sensitive and quantitative but relies on bulky instruments and cannot be used in POC settings or for frequent self-diagnosis [91]. Our strategy can differentiate SARS-CoV-2 and SARS-1 with femtomolar level sensitivity with a wide dynamic range of six orders of magnitude, ideally for accurate detection and frequent testing to monitor the viral load in the patients. Furthermore, since the nanopore chips are made by conventional microfabrication, numerous nanopores can be patterned on a single substrate. Coupling with the commercially available miniaturized multi-channel amplifiers, our system can enable a highly multiplexing diagnostic instrument. However, we realized that pore-to-pore variation might affect the detection limit, especially for nanopore array-based multiplexing sensing. For future POC testing, all the nanopores will need to be calibrated with reference samples.

Due to the small feature size of the nanopores, the presence of debris and air bubbles can prevent the solution and target particles from flowing through the nanopore. Therefore, a pre-wetting and cleaning process is crucial for the stable translocation of the AuNPs. We found that treating the chip with a 5 min sonication, followed by washing with deionized water and isopropyl alcohol is sufficient to wet and clean the chip. In our case, 40 nm AuNPs are chosen for this CRISPR assay and are passed through a 90 nm nanopore. We tested the inter-arrival time of the AuNPs at various concentrations and showed it follows

the Poisson process (**Figure 2.15**). The nanoparticle and nanopore size combination ensure the sensitive trace tracking of single AuNPs without causing nanopore blocking issues. With the same nanoparticle size, we determined that a larger nanopore can indeed reduce the blocking, but it also compromises the sensitivity. The mechanism of nanopore detection is to detect the concentration of nanoparticles by detecting the current change when nanoparticles pass through the nanopore at a certain time. When the nanopore size is too large in proportion to the size of the nanoparticles, most of the nanopore space is not affected when the nanoparticles pass through the nanopore. Therefore, the current change is not obvious, and it is difficult to distinguish it from the signal fluctuation caused by artefacts, such as current noise. For example, many translocation events were not distinguished from the background with the 150 nm nanopore but were apparent with the 90 nm nanopore (**Figure 2.16**).

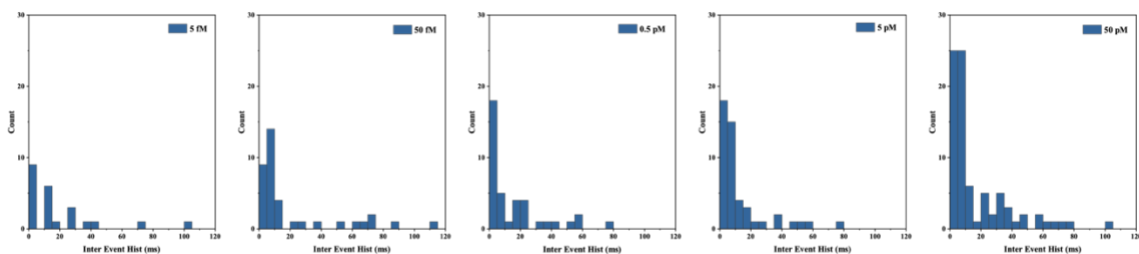


Figure 2.15 The inter-arrival time of the translocation event for different concentrations of AuNPs, following the Poisson process. Reprinted from [72]

In this work, the upper bound of the voltage setting is 700 mV, and the maximum current value that can be read is 200 nA. In the future, the sensitivity of solid-state nanopore sensing can be further improved by upgrading the electronic sensing circuit. Since the driving force of AuNPs movement comes from the electrical potential difference of the electrodes, increasing the voltage at both ends will increase the number and frequency of

nanoparticles passing through the nanopore. In addition, increasing the current by either increasing the applied voltage or changing the buffer concentration can also increase the signal-to-noise ratio as the translocation signals from the background noise can be better identified [89], [92].

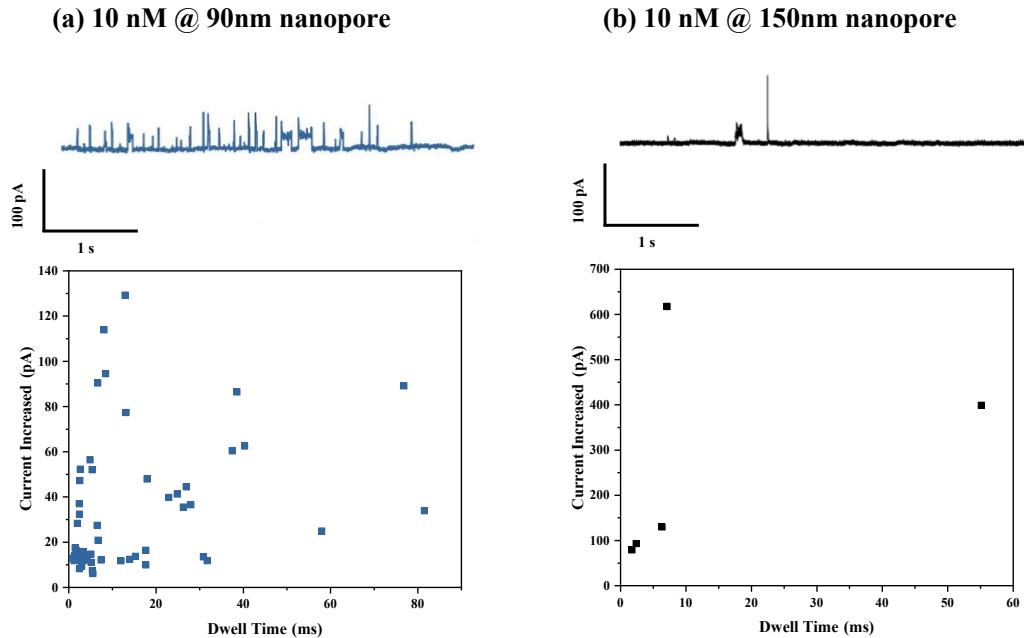


Figure 2.16 (a) Current trace and ionic current vs time trace for the AuNPs through (a) 90 nm nanopore chip and (b) 150 nm nanopore chip. Reprinted from [72]

For the trace of the CRISPR-cleaved AuNPs, the histogram of the current increase does not fit a Gaussian distribution. There could be two reasons for this: 1) Impurities, such as CRISPR-Cas13 complexes and nucleic acid probes in the sample, can affect the translocation signal of the AuNPs. In contrast, the current signal of the pure AuNPs (Figure 3) fits the Gaussian distribution well because there are no impurities in the solution; 2) For CRISPR experiments, the AuNPs concentration in the solution is low. Since our data model will only fit the Gaussian distribution with a large amount of data, the statistical analysis

is likely to deviate when the AuNP concentration is low. In the future, we will focus on improving our data model to interpret the data more effectively [79].

One unique advantage of the CRISPR-Cas13a assay is that the guide RNA sequence can be programmed to detect a specific target RNA. In this work, we designed a guide sequence for SARS-CoV-2, and this guide showed great specificity against the SARS-CoV-1 negative control. This strategy can be extended to detecting other diseases, such as sepsis, cancer, and genetic disorders, by using nucleic acids as biomarkers [93]. The combination of the high specificity of the AuNP-based CRISPR assay with a sensitive solid-state nanopore sensor can provide an appealing alternative for nucleic acid detection methods. Finally, it is worth noting that the experimental setup presented here may be useful for studying the dynamics of microscopic particles, as well as the change of conductivity of microscopic particles in different solutions [94].

## Chapter 3. Electrochemical application in virus detection

### 3.1 Introduction

Electrochemical detection is a powerful analytical technique used to detect and quantify molecules based on their electrochemical properties. It involves the conversion of chemical information into an electrical signal, which can be measured and analyzed to provide information about the presence and concentration of target analytes [95]. The basic principle of electrochemical detection relies on the redox reactions that occur at electrodes when analyte molecules interact with the electrode surface. These reactions result in changes in electrical current, voltage, or impedance, which can be monitored and correlated with the concentration of the analyte [96].

There are several common types of electrochemical detection techniques, including:

**Voltammetry:** In voltammetry, a potential is applied to the working electrode, and the resulting current is measured as a function of the applied potential [97]. By sweeping the potential over a range of values, different redox reactions can be induced, allowing for the identification and quantification of analytes;

**Amperometry:** Amperometry involves measuring the current at a constant applied potential [98]. When analyte molecules undergo redox reactions at the electrode surface, they produce a current that is directly proportional to their concentration, allowing for sensitive detection;

**Potentiometry:** Potentiometry measures the voltage difference between a reference electrode and a working electrode in a solution containing the analyte [99]. Changes in voltage, resulting from redox reactions or changes in ion concentration, are used to determine the concentration of the analyte.

Electrochemical detection offers several advantages, including high sensitivity, rapid response times, and compatibility with a wide range of analytes [100]. It is widely used in various fields, including environmental monitoring [101], pharmaceutical analysis [102], clinical diagnostics [103], and food safety testing [104]. Recent advances in electrochemical detection techniques have focused on improving sensitivity, selectivity, and miniaturization. Nanomaterials, such as carbon nanotubes, graphene, and metal nanoparticles [105], have been employed to enhance the performance of electrochemical sensors by increasing the surface area, facilitating electron transfer, and providing sites for specific molecular recognition. Additionally, advancements in microfabrication techniques have enabled the development of miniaturized and integrated electrochemical sensor platforms, suitable for point-of-care testing and portable devices [106]. These innovations continue to expand the capabilities and applications of electrochemical detection, making it an indispensable tool in modern analytical chemistry.

### **3.2 Biosensors using electrochemical detection**

Electrochemical sensors involve using electrodes to measure the electrochemical changes that occur when a chemical interacts with a sensing surface. An electrochemical sensor is a device for quantitatively detecting oxidation or reduction currents of a specific chemical species. Electrochemical sensors have the advantages of simple measurement procedures, short reaction times, and adequate sensitivity and selectivity [31]. In chemical sensor systems, a chemical reaction can convert the target species into a detectable species. On

the other hand, electrochemical sensor systems can easily monitor concentration changes over time [32].

Electrochemical biosensors are preferred for POC testing due to their speed, affordability, and simplicity. The combination of electrochemical biosensors with microfluidics [107], novel conductive materials [108], and CRISPR/Cas technology [109] enables rapid, sensitive, and quantifiable multiplex nucleic acid detection. Also, the electrochemical sensors have enhanced sensitivity, and the change of signal also can be easily quantified by electrochemical detection.

Compared to fluorescence detection, electrochemical detection offers a simpler, lower-cost, and more powerful strategy for nucleic acid detection. Recently, several electrochemical CRISPR-based biosensors have been established for nucleic acid detection by exploiting the cleavage ability of CRISPR-Cas proteins. Richard et al. developed a kind of Electrochemical microfluidic biosensor for miRNA diagnostics (**Figure 3.1**) [110]. It is CRISPR-Cas13a-driven electrochemical microfluidic biosensor for nucleic acid amplification-free miRNA diagnostics. GOx-labeled antibody as the electrochemical signal indicator. Different current signals are displayed in the presence or absence of target RNA.

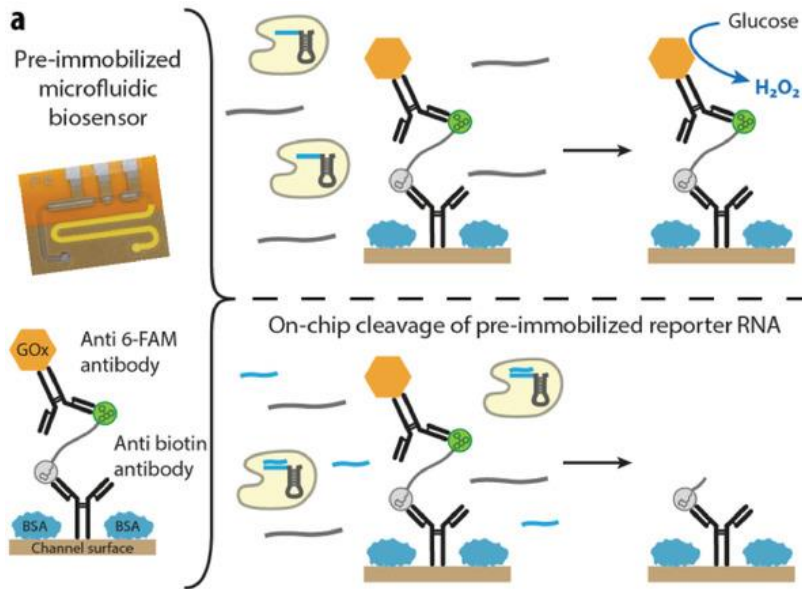


Figure 3.1 Schematic illustrating the on-chip cleavage procedure for samples with or without target miRNAs (blue). The biotin and 6-FAM-labeled reporter RNA is immobilized to the anti-biotin antibody, where the GOx-labeled anti-fluorescein antibody binds to the reporter RNA. The crRNA/Cas13a complex and a sample with and without target miRNAs (blue), is introduced into the biosensor to the completely pre-immobilized assay. The target activated enzyme cleaves the bound reporter RNA and thus enables the removal of the GOx-labeled antibody, resulting in a reduced amperometry signal. Reprinted from [110]

Marjon et al. developed an electrochemical strategy for low-cost viral detection [111].

Methylene blue is the signal indicator conjugated on the gold electrode surface via ssDNA.

After the LAMP amplification and CRISPR Cas12a cleavage, the methylene blue will

cleave from the gold surface and can cause changes in electrical signals (**Figure 3.2**).

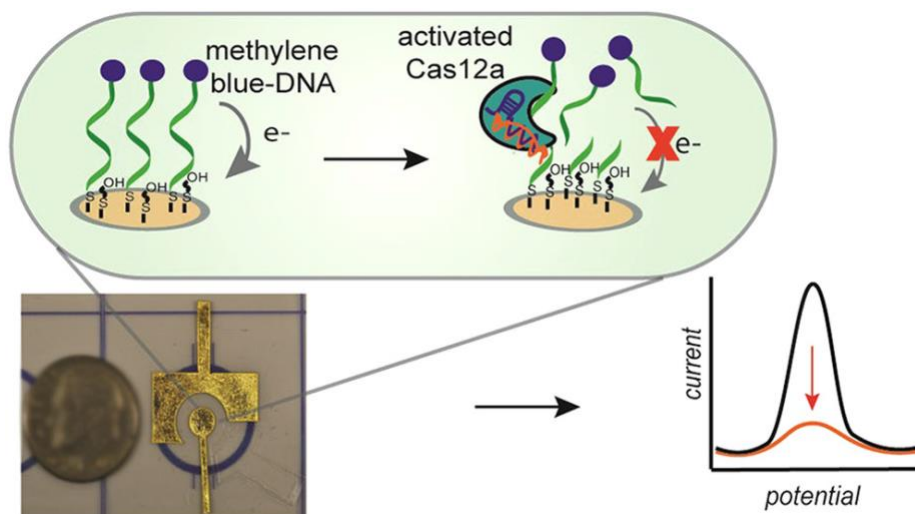


Figure 3.2 Electrochemical Strategy for Low-Cost Viral Detection. MB (methylene blue)-labeled oligonucleotides immobilized on gold leaf electrodes, the activated Cas12a can cleave the oligonucleotides resulting in voltametric signal changes. Reprinted from [111]

### **3.3 Aerosol jet printing prints highly sensitive electrodes**

Aerosol inkjet printing is an innovative technique that has gained significant attention in recent years for its ability to create high-resolution prints and coating on various surfaces [112]. This printing methods involves the use of an aerosolized ink, which is propelled onto a substrate using an inkjet nozzle system. The ink is broken down into fine droplets and then ejected onto the desired surface, resulting in precise and detailed patterns. As the aerosol inkjet printing offers several advantages over traditional printing methods [113]. Firstly, it enables high-resolution printing on various substrates, including paper, plastic, and even 3-D objectives. This versatility makes it suitable for a wide range of applications. Such as electronics [114], healthcare [115], and energy [116]. Secondly, aerosol inkjet printing allows for faster printing speeds and improved efficiency compared to other techniques. It is easy to achieve large-scale production. Additionally, the non-contact nature of the process eliminates the risk of damage to delicate substrates. Here, we present a dual-function biosensor for the detection of infectious disease pathogens using SARS-CoV-2 as an example. This biosensor is an integrated three-electrode platform, fabricated by aerosol inkjet printing [117].

### **3.4 Electrochemical and Colorimetric Biosensor for SARS-CoV-2 Detection**

In the chemical or colorimetric signal generation format, the HRP-enzyme + 3,3',5,5'-tetramethylbenzidine (TMB)-substrate signal generation is a common group reagent [118]. The redox relationship between hydrogen peroxide ( $\text{H}_2\text{O}_2$ ) and TMB exists, and HRP can catalyze the oxidation of TMB to the blue product  $\text{TMB}^{2+}$ . Due to their intrinsic and significant catalytic properties, enzymes are often used as signal amplifiers in biochemically relevant assays, and the change in color signal intensity is linearly related to the target concentration and can be read out by the naked eye or quantified with a spectrometer. At the same time, different amounts of TMB redox reactions also produce different electrochemical signals, which can be detected by potentiostat, not only with good detection sensitivity but also to quantify the reaction conditions.

Moreover, CRISPR-Cas assays can work with various sensing mechanisms to achieve a multiplexing and amplification-free diagnostic platform. For example, electrochemical biosensors have drawn great interest due to their excellent sensitivity/specificity, cost-effectiveness, and ease of manufacturing [119], [120]. CRISPR-integrated electrochemical biosensors have been developed for biomarker detection of nucleic acids, proteins, and transcriptional regulation [34], [121]. However, most of these biosensors are fabricated by expensive microfabrication processes and require the immobilization of sensing probes on an electrode surface, which is complicated and time-consuming [122], [123]. Therefore, developing a new electrochemical biosensor platform that does not require probe immobilization is highly desired.

Here, we present a dual-function biosensor for the detection of infectious disease pathogens using SARS-CoV-2 as an example. This biosensor is an integrated three-electrode platform, fabricated by aerosol inkjet printing. Aerosol inkjet printing is an innovative technique that has gained significant attention in recent years for its ability to create high-resolution prints and coating on various surfaces [112]. In addition, we developed a horseradish peroxidase (HRP)-labeled CRISPR-Cas13a assay to detect SARS-CoV-2 virus. Both colorimetric and electrochemical readouts are provided by the catalytic oxidation of 3,3',5,5'-tetramethylbenzidine (TMB) with a HRP tag. After activation of CRISPR-Cas13a by an RNA target and subsequent cleavage of the HRP-labeled ssRNA probes, the TMB substrate is added to produce colored oxidation products by a redox reaction. This reaction changes both the electrochemical properties and the color of the assay solution and has thus dual function. Without target amplification, detection limits of 195 and 163 fM are achieved for colorimetric and electrochemical sensing, respectively. Both readouts demonstrate excellent linearity with target concentrations ranging from the femtomolar to picomolar range and are highly specific against negative control samples. Thus, this dual-function biosensor establishes a key technology that is intended for POC detection of infectious diseases.

3.4.1 Anti-FAM HRP labeled CRISPR-Cas13a nucleic acid assay for current and colorimetric detection.

**Materials and reagents:** Dynabeads<sup>TM</sup> MyOne<sup>TM</sup> Streptavidin C1 (10 mg/ml) was purchased from Thermo Fisher Scientific, Inc. HRP Anti-Fluorescein antibody (1 mg/ml)

was purchased from Abcam, Inc. TMB Substrate Solution was purchased from Thermo Fisher Scientific, Inc. Guide RNA and RNA reporter were purchased from IDT. Inc. Lbu-Cas13a protein was prepared based on our established protocols and described in our previous publication [124]. The target SARS-CoV-2 spike genes and negative controls virus SARS-1 and Influenza A (H3N2) were amplified from plasmids.

**CRISPR Lbu-Cas13a trans-cleavage:** The Cas13a:crRNA complex was prepared by incubating 1  $\mu$ M CRISPR Lbu-Cas13a and 1.1  $\mu$ M grRNA in 6  $\mu$ l of 5  $\times$  Standard Buffer (250 mM KCl, 100 mM HEPES, 25 mM MgCl<sub>2</sub>, 5 mM DTT, 25% Glycerol, pH 6.8) and 24  $\mu$ l RNase-free water for 2 min at 37°C followed by 8 minutes at room temperature. Then put on ice for later use. Afterward, we added 4  $\mu$ l of the Cas13a:crRNA complex into 20  $\mu$ l of RNase-free water, 8  $\mu$ l of 5  $\times$  Standard Buffer, 4  $\mu$ l of target RNA with different concentrations, and 4  $\mu$ l of fluorescein-biotin ssRNA (10  $\mu$ M). The complex solution was incubated for 15 min at 37°C.

**Conjugating the RNA reporters onto HRP Anti-Fluorescein antibody:** After the trans-cleavage of the ssRNA reporter. Then 20  $\mu$ l (0.6  $\mu$ g/ml) of HRP Anti-Fluorescein antibody was added and incubated on a rotary mixer at room temperature for 30 min.

**Magnetic bead isolation:** The streptavidin-coated magnetic beads were washed with washing buffer (1 $\times$ PBS containing 0.01% Tween 20) three times before use. Then 60  $\mu$ l of CRISPR:Cas13a-HRP complex solution was added to 20  $\mu$ l of Dynabeads solution. The mixture was incubated on a rotary mixer at room temperature for 30 min. The HRP-magnetic beads were separated from the unbound ssRNA reporter by magnetic separation.

**Colorimetric detection:** The magnetic bead solution was then washed with washing buffer three times. Afterward, 20  $\mu$ L of the TMB substrate solution was added into the magnetic

bead solution. The colorimetric changes were visually observed after a 15 min reaction. The absorption spectrum was recorded with a microplate reader (Spectramax iD3, Molecular Devices, USA) by removing the supernatant from the beads solution and diluting to 100  $\mu$ L in nuclease-free water.

RGB value analysis: Images were taken by a smartphone camera (iPhone 12) and the changes in RGB values for each reaction were extracted for analysis. A 500-pixel x 500-pixel square in each reaction pool was extracted (n=5) and analyzed by ImageJ, where the color RGB value was recorded.

Fabrication of the graphene electrode: The 3-electrode platform includes a working electrode, a counter electrode, and a reference electrode. An aerosol jet (Aerosol Jet 300, Optomec Inc. US) with aerodynamic focusing was used to precisely deposit graphene ink (Sigma Inc. US) onto the polyethylene terephthalate (PET)-based printed electronics substrate (Novacentrix, Novele™ IJ-220). The ink was placed in an atomizer that produces ink droplets with a size between 1 and 5  $\mu$ m. The aerosol mist was then delivered to the deposition head, which was focused by the sheath gas that acts as an annulus around the aerosol. As the sheath gas and aerosol passed through the nozzle, they were accelerated, and the aerosol was "focused" into a tight stream of droplets that flows within the sheath gas. The resulting high-speed particle stream remained focused over a distance of 2 mm from the nozzle to the substrate without compromising the resolution. Once the chip was fabricated, photonic curing was used to rapidly and efficiently convert the graphene ink solution into high-quality thin-film electrodes [125]. Samples were passed through a Novacentrix Pulseforge 3300 machine to expose graphene to an incident energy. The PulseForge 3300 tool is capable of delivering peak power up to 100 kW/cm<sup>2</sup> in pulses as

short as 30 ms. In this work, each sample was exposed to two 200 V pulses with a pulse frequency of 2.8 Hz and a duration of 1,200 ms.

Characterization of the 3-electrode testing chip: The electrode morphology was scanned using a profilometer (Modular Standard Optical Profilometer, Nanovea ST400). The dimensions of the three-electrode section and the thickness of various materials were determined by the profilometer. The stability and reproducibility for the 3-electrode system were also tested. Twenty microliters of H<sub>2</sub>SO<sub>4</sub> background electrolyte (0.05 M) were added into the reservoir. Cyclic voltammetry was set between 0 and 1.2 V/ The speed rate was 0.1 V/s and the number of scans was five cycles.

Electrochemical detection: After the magnetic bead isolation, 20 µL of the reacted TMB solution was removed from the tube and placed into the electrochemical platform reservoir. The chronoamperometric response was obtained at + 3mV over 60 s on a potentiostat (Reference 600TM, Gamry Instruments Inc, USA) with a graphene counter electrode and a reference electrode.

#### 3.4.2 HRP-labeled CRISPR Cas13a assay for virus detection.

##### **Working principle of the assay.**

The working principle of the dual-function biosensor is illustrated in **Figure 3.3A**. In this protocol, an RNA fragment of the S gene of SARS-CoV-2 is detected by the LbuCas13a:crRNA complex. In the presence of the target gene, the dual labeled fluorescein and biotin ssRNA reporters are cleaved by the CRISPR-Cas13a complex. In the next step, the HRP anti-fluorescein antibody is added to the solution, which can be conjugated with

the fluorescein on the reporter side of the ssRNA. After magnetic separation, the conjugates are present on the magnetic beads while the unbound HRP anti-fluorescein antibody is removed from the supernatant. In the last step, TMB substrate solution is added to the washed magnetic beads, allowing the HRP on the magnetic beads to catalyze TMB to the blue product TMB<sup>2+</sup>. For electrochemical detection, the amount of HRP attached to the magnetic beads varies with the target RNA concentration due to the amount of trans-cleaved probes. HRP reacts with TMB for signal amplification and current detection. For colorimetric detection, the HRP conjugated on the magnetic beads can catalyze the oxidation reaction of TMB. This reaction presents a color change from colorless to blue and can be detected by a microplate reader. The inset in Figure 1A shows the details of the activated and inactivated Cas13a reaction. When the Cas13 enzyme is activated, no HRP remains on the beads, thus TMB cannot be oxidized. On the other hand, inactivated Cas13 enzyme does not cleave the reporter probes, leaving HRP on the magnetic beads and oxidizing TMB, which increases H<sub>2</sub>O in the solution and decreases the current. **Figure 3.3B** shows the segment of the target and the guide RNA sequences. We used the gold electrodes to monitor SARS-CoV-2 RNA-activated LbuCas13a:crRNA complex endonuclease activity. As shown in **Figure 3.3C**, the current signal increases significantly from 0.30 to 0.84 after the addition of the LbuCas13a:crRNA complex, indicating that the CRISPR complex is active.

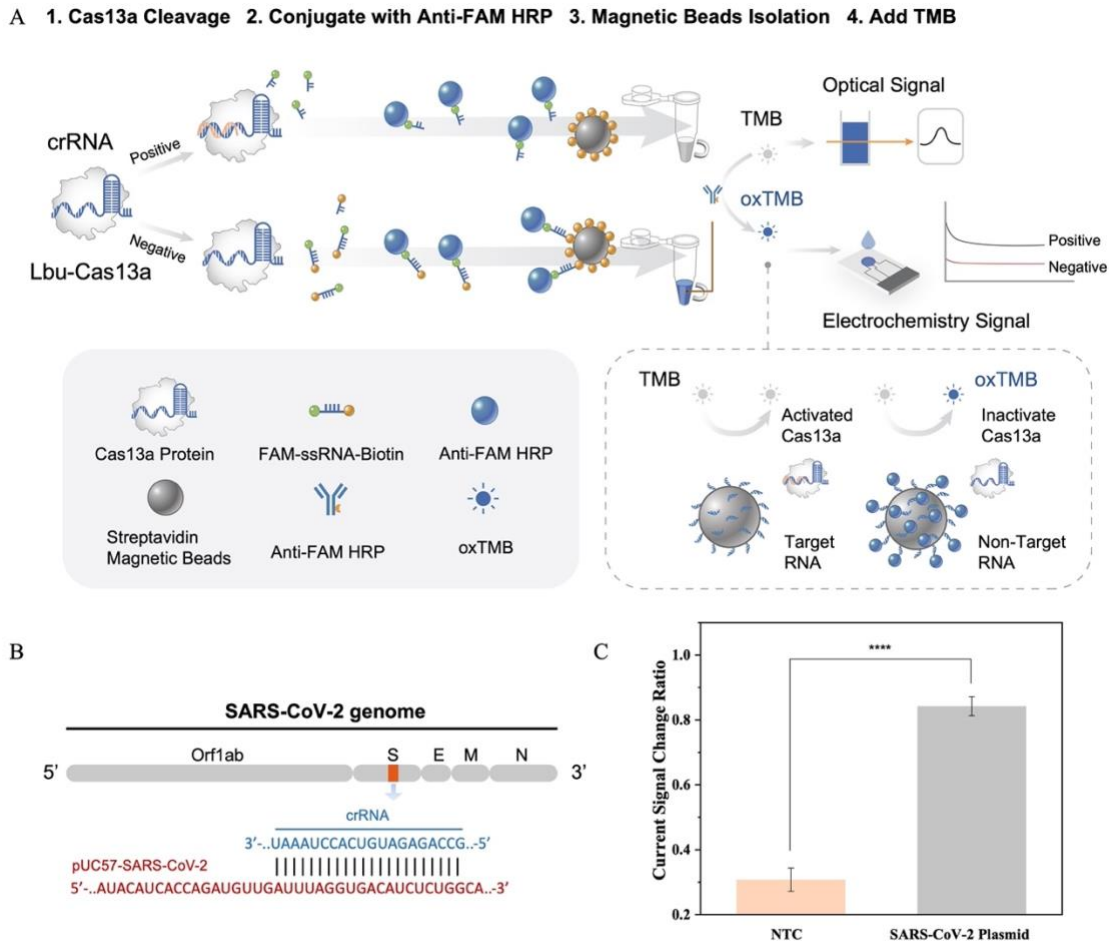


Figure 3.3 A. Schematic of the reaction strategy: Step 1. CRISPR-Cas13a:crRNA complex cleaves an ssRNA probe; Step 2. Anti-FAM HRP binds the FAM labeled ssRNA probe; Step 3. The non-cleaved biotin-labeled ssRNA probe is isolated by streptavidin magnetic beads; Step 4. Colorimetric reaction and current detection with TMB oxidization. B. SARS-CoV-2 gene location, target site, and guide RNA sequence. C. Current Signal Change Ratio with and without SARS-CoV-2 target, showing ~3-fold difference in signal. The statistical significances are calculated by *t*-test (\*\*\*\* $P \leq 0.0001$ ). Error bars: SD,  $n=3$ . Reprinted from [117]

The fabrication process of the chip (10 mm x 6 mm) is shown in **Figure 3.4A**. The surface topography was characterized using optical profilometry (**Figure 3.5A**) and cyclic voltammetry (**Figure 3.5B**). The thickness of the graphene electrode is  $3 \pm 0.2 \mu\text{m}$ , showing a very smooth surface (**Figure 3.6**). The repeatability and reproducibility of the gold electrodes were tested by tracking their response to  $\text{H}_2\text{SO}_4$  solutions over a set period.

The electrode substrate was stored in a closed container and the response to the H<sub>2</sub>SO<sub>4</sub> solution (0.05 mM) was recorded. **Figure 3.5A** shows several representative voltammetry curves of the graphene electrodes. In the voltammograms of the three measurements performed on the same day (lines 1, 2, and 3), 98.0% of the original peaks and potentials were found to be retained, demonstrating the high stability of the chip. Similarly, the response of the H<sub>2</sub>SO<sub>4</sub> solution (0.05 mM) was recorded on different days (one day apart, lines 4, 5, 6). Voltammograms show similar trends with the same current magnitude at the desired potential with an RSD of 5.81%, demonstrating the high repeatability and reproducibility of the working electrode [126].

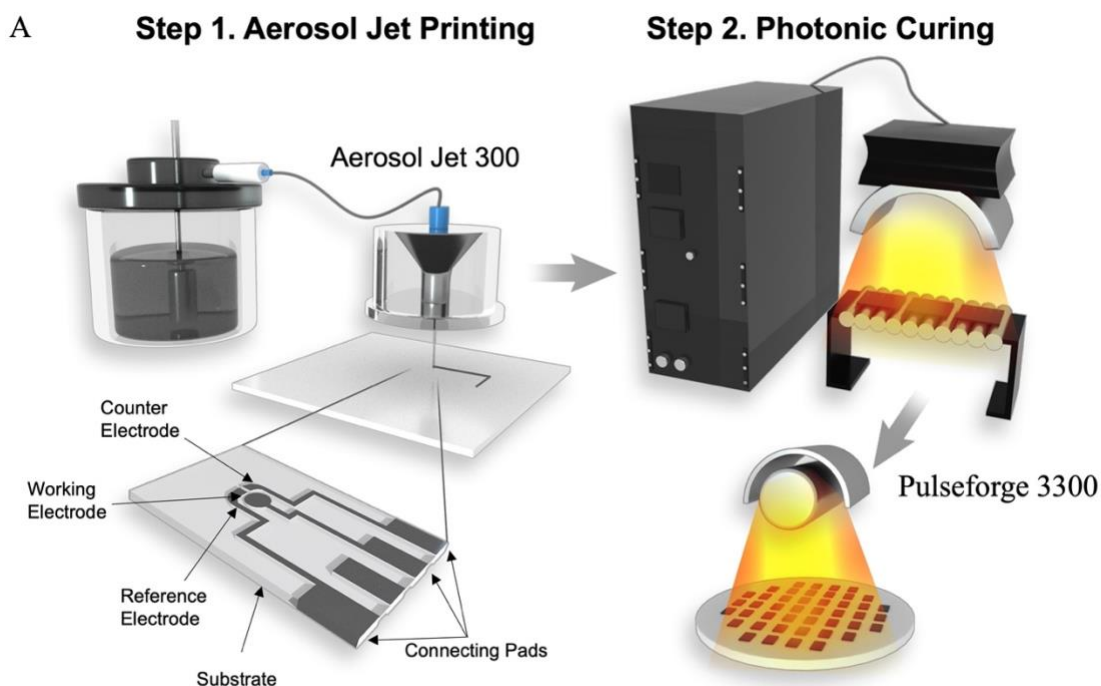


Figure 3.4 A. (1) Schematic of the aerosol jet printing process for the dual-function biosensor and the graphene electrode with a working electrode, a counter electrode, and a reference electrode. (2) The photonic curing system for the graphene electrode. Reprinted from [117]

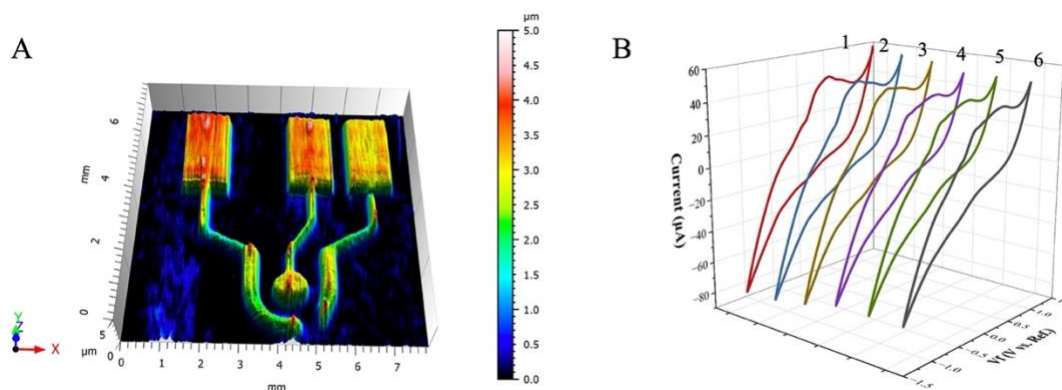


Figure 3.5 A. Profilometer scan of the graphene electrode, showing a smooth surface with only  $\pm 0.2 \mu\text{m}$  variation. B. Graphene electrode voltammetry curves for  $\text{H}_2\text{SO}_4$  solution (0.05 mM). Lines 1, 2, and 3 are scans on the same day, and lines 4, 5, and 6 are scans from different days (one day apart). Reprinted from [117]

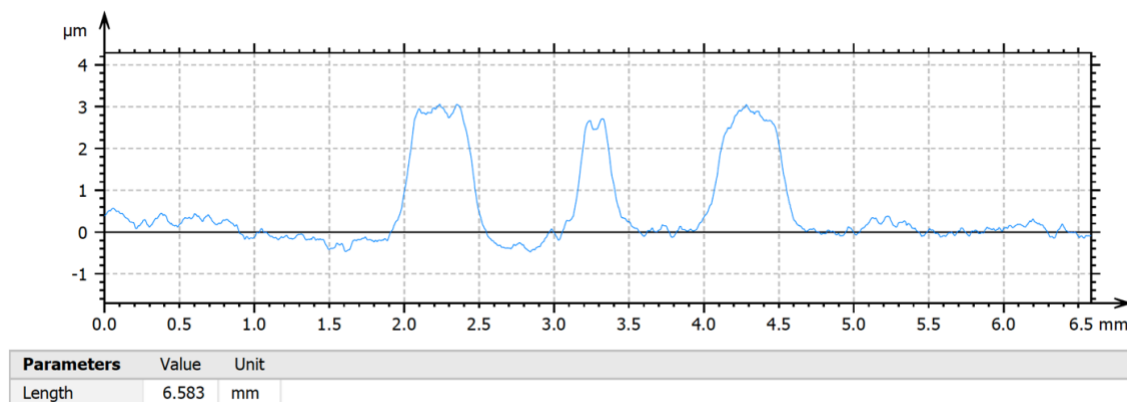


Figure 3.6 Height value of electrode cross section. Reprinted from [117]

In our assay, increasing concentrations of target RNA in the sample results in more HRP released from the magnetic beads, leaving less HRP enzyme to oxidize TMB. As shown in Figure 3, the absorbance of the characteristic peak at 650 nm derives from the catalyzed reaction product of TMB, indicating that HRP attached to the magnetic beads possesses good catalytic ability. As expected, the UV-vis absorption peak gradually decreases with the increasing target RNA concentration from 100 fM to 1 nM (**Figure 3.7A**). **Figure 3.7B** shows the absorption measurements for the different negative controls (SARS-1, Influenza

A, and no target), which are noticeably different from the positive samples. In **Figure 3.7C**, the absorbance is linearly correlated with the change of target RNA concentration from 100 fM to 1 nM ( $R^2 = 0.91385$ ). Therefore, the detection limit was determined to be 324.1 fM based on the  $3\sigma$  rule [127]. The inset of **Figure 3.7C** is a photograph of the reaction solution in daylight associated with the increase of target RNA concentration. We note that the color of the reaction mixture changes continuously from dark to light with increasing target concentration, which can be identified by naked eye. The peak absorption of the positive and negative samples is shown in **Figure 3.7D** and the inset is a photograph of the sample, clearly showing the difference.

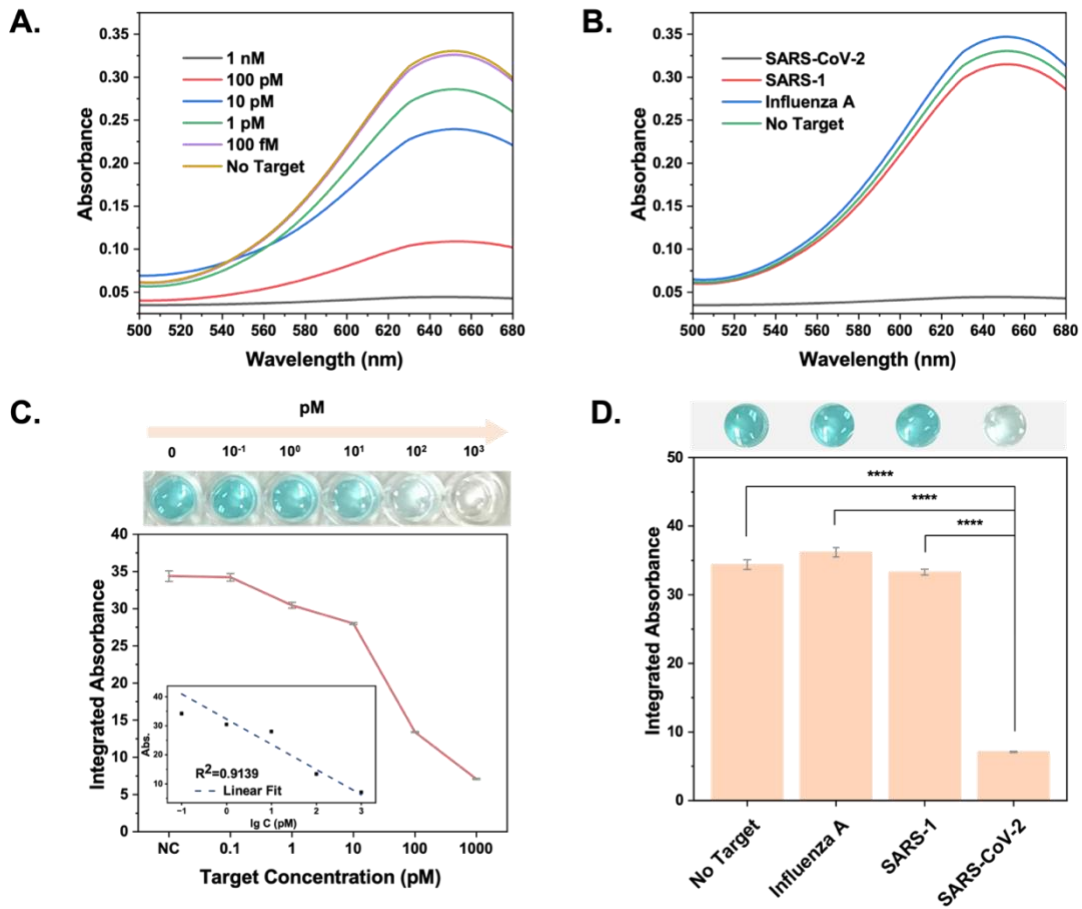


Figure 3.7 A. UV-vis spectrum vs. SARS-CoV-2 RNA concentration after RNA detection by our assay. B. UV-vis spectrum vs. positive and negative target. C. Top: Photographs of the test solution with different SARS-CoV-2 concentrations under daylight. Bottom: The relationship between the integrated absorbance and the concentration of SARS-CoV-2 RNA. Inset: The calibration curve for the integrated absorbance value vs. The logarithm of the target concentration. Error bars denote standard deviation (n = 5). D. Top: Photographs of the test solution of different targets under daylight. Detection specificity of the SARS-CoV-2 RNA target compared with other targets. Error bars denote standard deviation (n = 5). The asterisks represent statistical significance according to a *t*-test of \*P ≤ 0.05, \*\*P ≤ 0.01, \*\*\*P ≤ 0.001, \*\*\*\*P ≤ 0.0001. Reprinted from [117]

After optimizing reaction conditions, the analytical performance of our chip was investigated. As shown in **Figure 3.8A**, the color of the substrate changes from blue to colorless as the concentration of SARS-CoV-2 RNA increases. By analyzing the RGB values, we found that the R values are linearly correlated with target RNA concentration ranging from 100 fM to 1 nM ( $R^2 = 0.95$ ). (Table S1). Therefore, the detection limit was determined to be 195 fM according to the  $3\sigma$  rule. The specificity of our chip was also investigated by using SARS-1 and Influenza A as negative samples. As shown in **Figure 3.8B**, without target input, the solution shows no significant color change, while the addition of target RNA triggers a dramatic color change. Similar to the no target sample, this color change can easily be observed by naked eye. This result indicates that our strategy can be used for the detection of SARS-CoV-2 RNA with a high sensitivity and specificity.

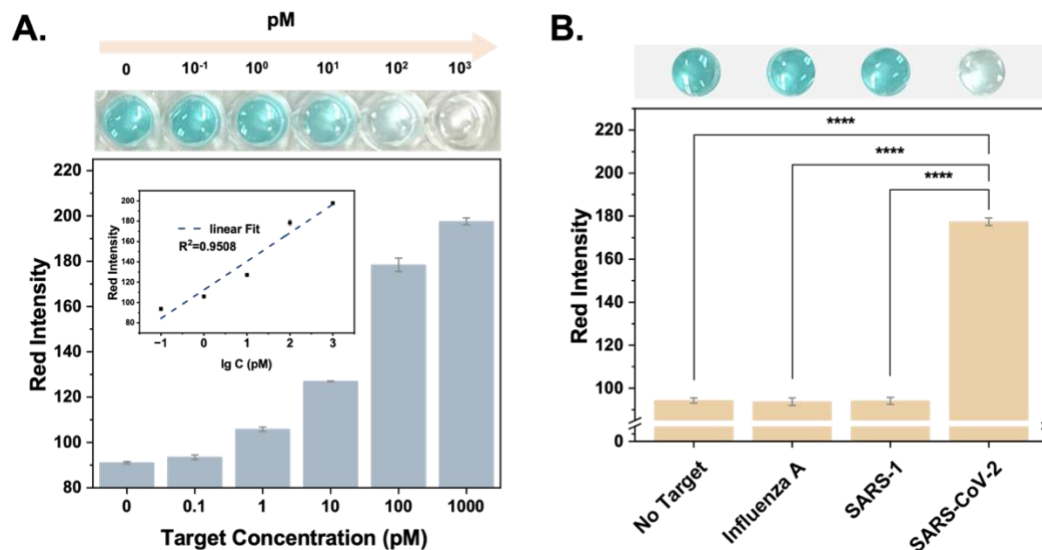


Figure 3.8 A. Top: Photographs of the test solution with different SARS-CoV-2 RNA concentrations under daylight. Bottom: The relationship between the R value and the concentration of the SARS-CoV-2 RNA. Inset: Calibration curve of the R value vs. The logarithm of the target concentration. Error bars denote standard deviation (n = 5). B. Top: Photographs of the test solution with different RNA targets under daylight. Bottom: Detection specificity of the SARS-CoV-2 RNA target compared with other targets. Error bars denote standard deviation (n = 5). The asterisks represent statistical significance according to a *t*-test. \*P ≤ 0.05, \*\*P ≤ 0.01, \*\*\*P ≤ 0.001, \*\*\*\*P ≤ 0.0001. Reprinted from [117]

Electrochemical measurements were also performed to quantitatively assess the detection limit and dynamic range of the target. In the TMB substrate solution, the chronoamperometric response at +3 mV increases with increasing target RNA concentration (**Figure 3.9A**). A linear relationship was observed between chronoamperometric response and target RNA concentration ranging from 100 fM to 10 nM ( $R^2 = 0.98$ ) with a correlation coefficient (**Figure 3.9B**). The detection limit was determined to be 163 fM based on the  $3\sigma$  rule. **Figure 3.9C** and **Figure 3.9D** show the comparison of the current curves and different current values for chronoamperometric reactions for positive and negative targets, showing clear differences between positive and negative groups.

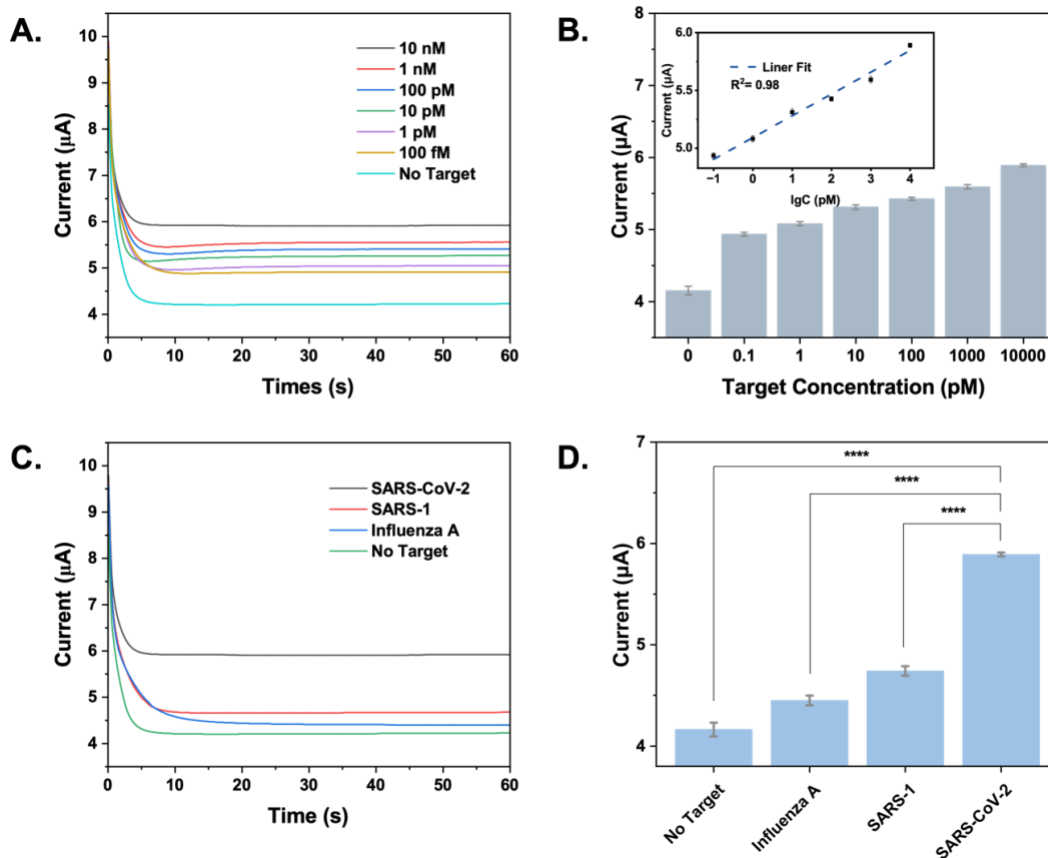


Figure 3.9 A. Chronoamperometric responses of SARS-CoV-2 RNA targets at different concentrations. B. Plot of current of last 30s mean value versus different concentrations of SARS-CoV-2 target. Error bars denote standard deviation ( $n = 5$ ). Inset: Calibration curve of the current vs. the logarithm of the target concentration. C. Chronoamperometric responses of the positive and negative targets. D. Detection specificity of the SARS-CoV-2 RNA target compared with other targets. Error bars denote standard deviation ( $n = 5$ ). The asterisks represent statistical significance according to a  $t$ -test. \* $P \leq 0.05$ , \*\* $P \leq 0.01$ , \*\*\* $P \leq 0.001$ , \*\*\*\* $P \leq 0.0001$ . Reprinted from [117]

A comparison of the linear fits of R values and current values for different concentrations of SARS-CoV-2 targets is shown in **Figure 3.10**. Both readings show excellent linearity over the range of target concentration from femtomolar to picomolar, confirming the high sensitivity and reliability of the biosensor.

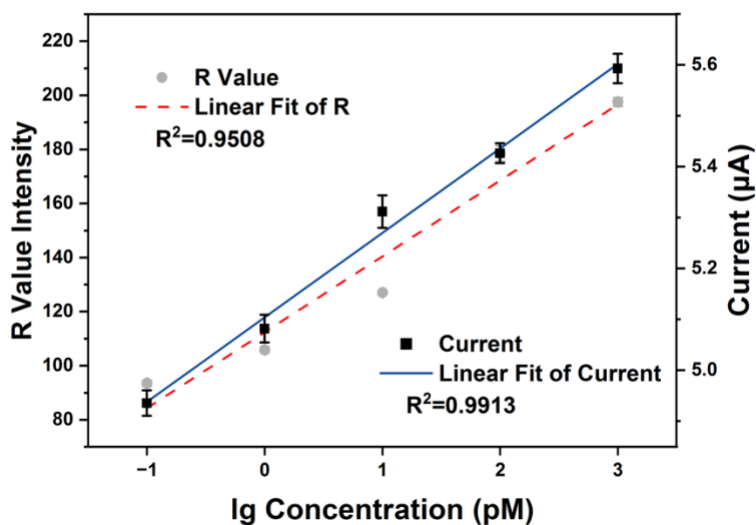


Figure 3.10 R value intensity and measured current vs. target RNA concentration with a  $R^2$  value of 0.9508 and 0.9913, respectively. Error bars denote standard deviation ( $n = 5$ ). Reprinted from [117]

### 3.4.3 Discussion

Our reaction chemistry is highly specific and reliable. First, specific guide RNA sequences only recognize specific target RNAs due to the characteristic specificity of the CRISPR guide RNA sensing the target sequence, making it more specific than other sensing methods, such as immunoassays [128]. We show that we can differentiate SARS-CoV-2 from negative controls such as Influenza and SARS-CoV-1 at various concentrations. Second, in our reaction, the signal indicator Anti-FAM HRP is conjugated on the magnetic beads via ssRNA linkers. After the washing step, the impurities in the reaction are washed away thus leaving the final reactants with a relatively pure HRP enzyme to react with the TMB substrate. The high purity of the analyte is critical for electrochemical detection, as the presence of impurities in the reaction solution can cause current changes and reduce the detection sensitivity [129]. Third, unlike other electrochemical methods, our approach

does not require complex modification of the electrode surface with capture antibodies or probes, thereby avoiding many limitations associated with surface functionalization and simplify the reaction step. Last but not least, this detection can be performed within one hour and at a relatively low cost. Short detection times are due to the rapidity of the Cas13 reaction and the timeliness of the current detection, which provide real-time results [130]. Our amplification-free detection method simplifies the whole reaction and is designed for POC applications. In addition, a useful biosensor should have good stability during the sensing process. By observing the response of our biosensor exposed to sulfuric acid (0.05 mM) over a set time for 12 cycles, voltammograms of multiple measurements on the same chip were compared, showing a very high retention of the original peaks and potentials.

One unique advantage of our biosensor is the dual-function detection scheme as we can track both electrochemical signal change and colorimetric signal change simultaneously. Reading color changes with the naked eye is simple and straightforward, which is desired for rapid POC applications [33]. On the other hand, the electrochemical sensing provides a more quantitative readout, which is crucial to monitor the viral load in the sample when necessary. Importantly, a similar detection limit for colorimetric and electrochemical sensing is achieved. This dual-function platform reduces the false-positive and false-negative results caused by the variation of target samples and test chips.

Our electrochemical chip was fabricated by aerosol-jet printing, which is highly stable and inexpensive. Aerosol-jet printing technology is a process of depositing extremely fine droplets (2-5  $\mu\text{m}$  diameter) of ink suspended in an aerosol onto a substrate to form patterns.

The aerosol used in this process acts as a carrier to deliver the ink to the surface, providing a more consistent and controlled deposition than traditional liquid-based inkjet technologies [113]. One of the main advantages of aerosol-jet printing technology is its ability to produce high-resolution patterns with precise control over the size and distribution of the ink droplets. This high level of control enables the creation of intricate and detailed designs, making it ideal for a wide range of applications, including printing on flexible and transparent substrates [131]. Another advantage of aerosol-jet printing technology is its ability to print on a wide range of materials, including those that are difficult to print on using traditional liquid-based inkjet technologies. This is due to the unique properties of aerosol, which allow it to conform to irregular surfaces and maintain its stability, even on porous or uneven substrates [115]. In addition, the chip manufacturing method we utilize significantly reduces production costs and enables easy scalability for large-scale production. We have demonstrated the significant benefits in cost and time without sacrificing sensitivity. In the future, when combined with portable electrochemical testing devices [132], it can facilitate timely POC testing in remote areas or regions with limited resources.

Our biosensor is based on a highly specific CRISPR-Cas13 assay and a highly sensitive electrochemical detection platform. Without target amplification, a detection limit of 200 fM is achieved, which is 500 times more sensitive than our previous results of using pure liquid phase CRISPR-Cas13a reactions [133]. This dual function of electrochemical and colorimetric approach also avoids photobleaching problems in fluorescence-based sensing. In the future, our assay can be combined with RT-LAMP or RT-RPA methods to extend

the detection limit by several orders of magnitude [134]. In addition, by simply changing the design of guide RNA sequences, our assay can be used to detect a wide range of infections and diseases, such as cancers and sepsis, which are the main causes of premature deaths [135]. Furthermore, aerosol inkjet printing is a highly versatile and precise printing technique that offers unique advantages in terms of material compatibility, resolution, and flexibility [136]. Its applications range from printed electronics and sensors to biotechnology and beyond, making it a promising technology for numerous industries seeking innovative and efficient printing solutions [137].

# **Chapter 4. Loop-mediated amplification integrated on microfluidic chips for point-of-care quantitative detection of nucleic acid**

## **4.1 Introduction**

Amplification-based nucleic acid detection methods are powerful techniques used to detect and quantify specific DNA or RNA sequences in biological samples [48]. These methods rely on the amplification of the target nucleic acid sequence to levels that are easily detectable, even if the initial concentration of the target sequence is very low. One of the most widely used amplification techniques is polymerase chain reaction (PCR), which involves cycles of DNA denaturation, primer annealing, and DNA synthesis by a DNA polymerase enzyme [49]. PCR amplifies the target sequence exponentially, making it highly sensitive and specific. Variants of PCR, such as quantitative PCR (qPCR) [54] and digital PCR (dPCR) [138], allow for precise quantification of target nucleic acid.

The isothermal amplification-based nucleic acid detection methods offer an efficient, rapid, and often deployable alternative to traditional PCR techniques, which require cycling through different temperature stages [139]. These methods operate at a constant temperature, simplifying instrumentation and reducing the time required for analysis. These technologies have brought revolutionary changes to molecular diagnostics, especially in environments with limited resources and lacking advanced laboratory equipment. One prominent isothermal amplification method is Recombinase Polymerase Amplification (RPA) [140], which utilizes recombinase proteins to facilitate primer binding to target sequences and DNA polymerase to amplify the primers. It operates at a

constant low temperature (37-42°C) and can detect DNA or RNA targets. Another commonly used amplification method is Loop-Mediated Isothermal Amplification (LAMP) [141], which employs multiple primers and a DNA polymerase with strand displacement activity to amplify DNA under isothermal conditions, typically around 60°C. Compared to PCR, LAMP offers high sensitivity, simplicity of equipment, and is suitable for point-of-care diagnostics.

Amplification-based nucleic acid detection methods have revolutionized molecular biology, diagnostics, and biomedical research by enabling rapid and sensitive detection of infectious agents, genetic mutations, and gene expression levels. They are essential tools in fields such as clinical diagnostics, forensics, environmental monitoring, and biotechnology.

#### **4.2 The different strategy of LAMP visualization nucleic acid detection method**

Detection of nucleic acids by isothermal amplification reactions requires simple and effective assays, resulting in a wide variety of endpoint and real-time monitoring methods. Isothermally amplified DNA can be visualized by gel electrophoresis or other post-amplification assay steps, but these steps require the reaction tube to be opened, thus greatly increasing the risk of carrying contamination [60]. To minimize this risk and increase the applicability of simple on-site assays, single-pot reactions are strongly recommended. Several assays applicable to such closed-tube amplification reactions are available for endpoint detection and real-time analysis of amplified DNA. Here, we focus



#### 4.2.1 The colorimetric LAMP reaction.

This section shows a detailed experimental procedure for the LAMP colorimetric reaction.

##### **Materials and reagents.**

Colorimetric LAMP assay for SARS-CoV-2 detection. SARS-CoV-2 Rapid Colorimetric LAMP Assay Kit was purchased from New England Biolabs, Inc. LAMP reaction was prepared in a total volume of 25  $\mu\text{l}$  which included 12.5  $\mu\text{l}$  WarmStart LAMP 2X master mix with UDG, 2.5  $\mu\text{l}$  primer mix (16  $\mu\text{M}$  of FIP and BIP primers, 2  $\mu\text{M}$  of F3 and B3 primers, 4  $\mu\text{M}$  of Loop F and Loop B), 2.5  $\mu\text{l}$  guanidine hydrochloride, 2  $\mu\text{l}$  target with different concentrations, 5.5  $\mu\text{l}$  nuclease-free water. Each tube is covered with 20  $\mu\text{l}$  of mineral oil. Place reactions into a heat block and incubate 65°C for 30 minutes. The color change of the solution can be observed with the naked eye at the end of the reaction.

The photograph at the top of Figure 4.2 shows the result of SARS-CoV-2 target amplification in a tube. It is easy to observe the color change of the solution with the naked eye. The solution changes to yellow in the presence of target DNA, and the negative control remains the same color, pink. The photograph shows that the detection limit is about 200 copies/ $\mu\text{l}$  (~334 aM). Phenol red is a pH indicator which can indirectly detect the results of amplification reactions because the synthesis of DNA produces a large amount of hydrogen ions, making the solution acidic and the phenol red indicator will become pink to yellow. The bar graph shows the Hue degree of different concentrations of SARS-CoV-2 target, for the negative sample, the Hue degree is about 340°, which has significantly

difference with positive samples. Using the photograph analysis, it's easily quantified the results and it's friendly for people with weak color.

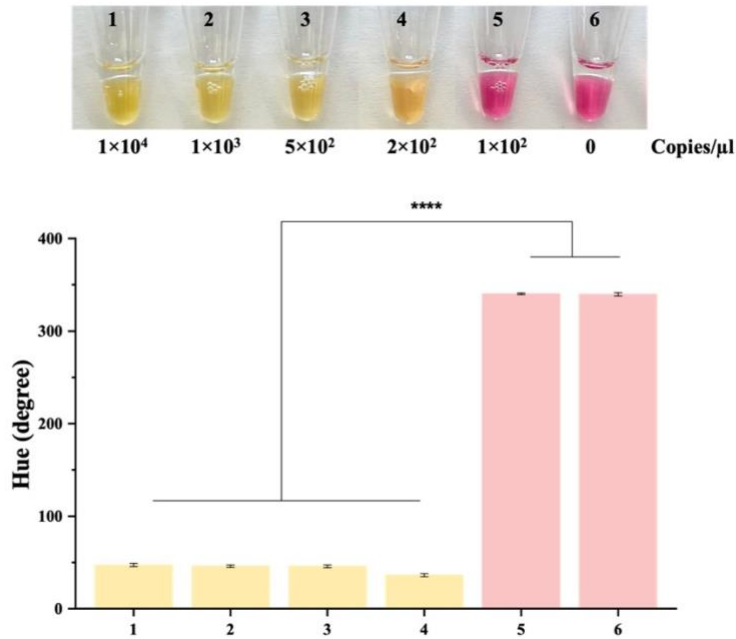


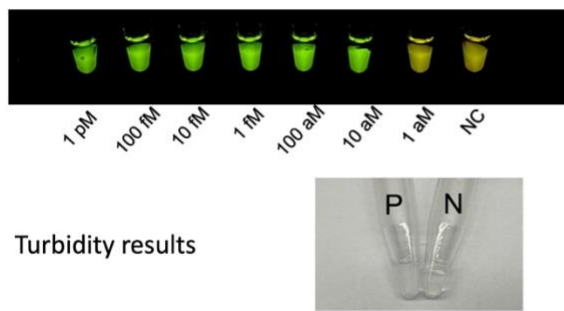
Figure 4.2 Colorimetric detection of the SARS-CoV-2 DNA by LAMP reactions.

The loop-mediated isothermal amplification method (LAMP) uses the N gene and E gene of SARS-CoV-2 as the detection virus and can detect the virus at a minimum concentration of 200 Copies/ $\mu$ l (334 aM) with the naked eye in 25 minutes at 65 degrees Celsius, which is a very low virus concentration and is certainly a great advantage for our virus detection. Here we can not only easily observe the change of signal with the naked eye, but also analyze the color analysis with hue. In future experiments, this amplification method will be combined with a microfluidic system and have intelligent picture analysis so that we can get an integrated, and fast and convenient way to detect viruses.

#### 4.2.2 Fluorescent dye-based LAMP reaction

Another assay that can be directly visualized LAMP reaction is the direct detection of isothermally amplified DNA using intercalating dyes. SYBR Green I and EvaGreen are widely used in PCR and are well characterized. These two dyes emit a weak fluorescent signal in the presence of single-stranded DNA (ssDNA) but instantaneously emit a strong fluorescent signal when bound to double-stranded DNA (dsDNA), requiring no reaction time, making them ideal for the detection of DNA in LAMP reactions. Because of its inhibitory effect on DNA polymerization at higher concentrations, SYBR Green I is primarily used in LAMP for end-point detection, either by adding it to the reaction mixture after the amplification reaction or by depositing the dye on the lid of the reaction vessel. EvaGreen is more suited for real-time monitoring of LAMP reactions because it does not affect DNA polymerization and therefore may be present throughout the reaction.

1. LAMP Result with Eva Green Dye



2. LAMP Result with SYBR Green I

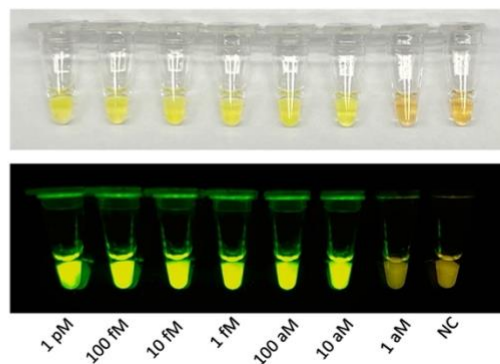


Figure 4.3 Fluorescent dye-based LAMP reaction result. 1.LAMP result with Eva green dye, target is lambda DNA, the detection limit can reach the 10 aM. The bottom figure shows the turbidity result of positive and negative. 2. LAMP result with SYBR Green I dye, the top photograph shows the tube under natural light. And the bottom photograph shows the fluorescent signal, the detection limit can reach 10 aM.

Figure 4.3 illustrates the results of the assay using the two fluorescent dyes, the limit of detection for both the Eva Green dye and the SYBR Green I dye is 10 aM. It can also be observed that the positives have turbidity while the negative control reaction is clear.

#### **4.3 Introduction of Microfluidic Nano digital chip for nucleic acid detection**

Foodborne illness presents significant challenges to both public health and the economy in the United States. Annually, there are over 45 million cases of illness, resulting in 3,000 deaths and economic losses exceeding \$55 billion [147]. The lack of rapid and sensitive detection methods for foodborne pathogens outside of laboratory settings contributes to frequent outbreaks associated with food products [148]. Conventional methods for detecting these pathogens in foods are limited, and detecting viruses like human norovirus presents additional challenges due to their inability to be easily enriched [149]. Widely used molecular techniques such as RT-qPCR require advanced equipment, electricity, and skilled operators, as well as stringent nucleic acid purification due to susceptibility to inhibitors in foods, making them impractical for non-laboratory settings [150]. Immunoassays, while simpler, suffer from poor sensitivity and produce false positives [151]. Consequently, developing a rapid, low-cost, highly sensitive, and field-ready assay for detecting foodborne pathogens in foods without complex sample preparation is crucial for reducing foodborne illness [152].

Microfluidic technology that can manipulate fluids in the channels with dimensions of tens to hundreds of micrometers has emerged as a distinct new field [153]. Over the past few

decades, microfluidic systems have rapidly developed into inexpensive and portable analytical devices, combining sample pretreatment, separation, reaction, and detection. Various methods have been reported to fabricate microfluidic devices, including laser ablation, hot embossing, and polymer casting [154]. Microfluidics is an ideal technology for isolating single-cell nucleic acids from bulk solutions into small volumes. The ability to manipulate nanoliter wells or droplets as independent reactors enables microfluidic devices to provide high-throughput analysis platforms. Compared to large-capacity microliter reactors, nanoliter reactors have been shown to enhance throughput and reduce detection time by generating high-density environments and concentrating diffusible signals. Additionally, enclosing the entire analysis process within nanoliter wells or droplets can reduce potential contamination, conserve reagents, and improve sensitivity, specificity, and reliability [152].

Foodborne pathogen detection conducted on digital microfluidic chips is frequently reported, including the analysis of protein biomarkers and target nucleic acids [155]. For example, droplet digital PCR (ddPCR) has been widely used in various biological research applications, including the detection of foodborne pathogens. Although ddPCR can provide sensitive and high-throughput detection of foodborne pathogens, it requires an external and expensive passive pump system to load reaction reagents, limiting its true portability and practical applications in point-of-need settings [156]. There are also many other methods to manufacture such reactors and perform reactions on chips. These methods include continuous-flow water-in-oil (w/o) droplets [157], static microchamber arrays such as SlipChip [158], porous arrays [159], OpenArrays [160], or valve-based reaction chamber

arrays [161]. Although each of these platforms has certain advantages, most still require additional mechanical manipulation or complex microfabrication to achieve complete digitization. Many of these platforms also require excessive sample volumes to achieve sample digitization. In situations where resources are limited, there is still a need to develop simple, inexpensive, and sample-saving devices to provide self-contained nanoliter compartments and minimize the complexity of chip operation.

Herein, we describe a Nano digital LAMP assay platform to achieve absolute quantitative analysis of nucleic acids. It introduces nano-digital LAMP reagents directly into a digital microfluidic chip. The signal amplification provided by this approach achieves ultra-sensitive detection of target nucleic acids. This portable chip uses loop-mediated isothermal amplification (LAMP) technology, which enables a one-pot target-specific assay based on the principle that a dye-labeled primer is added to a target-specific amplicon and a short complementary quencher hybridizes to the unbound primer. Digital quantitative nucleic acid detection can be performed directly from the target sample within 30 minutes. These contributions address the shortcomings of qualitative detection and complex assay instrumentation while retaining the advantages of simplicity, low cost, portability, and quantitative molecular readouts. Our portable digital nanoliter chip digitizes nucleic acid amplification signals without the need for external equipment and can be used for rapid, sensitive, convenient, and cost-effective on-site detection of viral and bacterial pathogens in food products, thereby improving food safety. This is important for the long-term goal of preventing the spread of foodborne pathogens in food and reducing foodborne disease outbreaks.

#### 4.4 Integrated microfluidic chip for isothermal amplification detection of nucleic acids

A fluorescence labeled FIP primer and quencher probe-based RT-LAMP assay was developed to detect norovirus.

##### Materials and Methods

RNA Preparation: Gene fragments of Norovirus (GII) (accession no. X86557) were ordered from Integrated DNA Technologies and resuspended in TE buffer (Table S1). The norovirus RNA for RT-LAMP assay was synthesized by HiScribe® T7 High Yield RNA Synthesis Kit (New England Biolabs, Inc). DNase I was used to remove the DNA templates. After that, a Monarch® RNA Cleanup Kit (NewEngland Biolabs, Inc) was used to purify the RNA. The RNA concentration was determined from the A260 value measured by a Nanodrop spectrophotometer. The gel electrophoresis image of the RNA sample is shown in **Figure 4.4**.

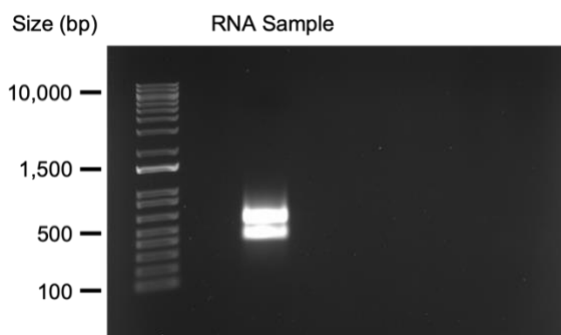


Figure 4.4 The gel electrophoresis image of Norovirus RNA sample.

LAMP Primer Design: The Norovirus primers sequences were designed according to the LAMP Primer Design Tool from New England BioLabs website. Primer sets were

analyzed by comparing to all the norovirus sequences in GenBank to avoid cross-reactivity with other viruses. Primer sets were also evaluated to minimize hairpin formation and self-dimerization using OligoAnalyzer. FAM-FIP primers and their complementary quenching probes were designed using IDT's online OligoAnalyzer tool (v3.1) with parameters adjusted for LAMP reaction conditions. Fluorescently labeled primer was selected by avoiding primers that were likely to form stable hairpins. The melting temperature of the fluorescent primer-quenching probe complex was designed to be significantly lower than 65 °C (at least 10 °C lower). Primers, dye-labeled primers, and quenching probes were ordered from Integrated DNA Technologies, Inc.

RT-LAMP Assay: We performed all RNA (norovirus) detection experiment with RT-LAMP. The LAMP kit was provided by NEB. Briefly, 25 µl of the reaction for each experiment contained 2.5 µl of 10× Isothermal Amplification Buffer, 1.5 µl of MgSO<sub>4</sub> (100 mM), 3.5 µl dNTP mix (10 mM), 2.5 µl of 10× target-specific primer mix (FAM-FIP/BIP 16 µM, F3/B3 2 µM, LoopF/B 4 µM), 1 µl of Bst 2.0 WarmStart DNA Polymerase (8 U/µl), and 2 µl of target DNA. The rest of the reaction contained 12.75 µl of nuclease-free water. Quenching probes were typically added at 1.5× the concentration of the corresponding fluorescently labeled primer.

Figure 4.5a briefly illustrates the principle of the RT-LAMP reaction for norovirus. The FIP primer labeled with a fluorophore at the 5' end was used for target amplification. As the amplification reaction proceeds, the fluorophore-labeled primer is incorporated into the amplicon. The reaction also includes a short quenching probe, which usually has about 10

bases complementary to the 5' end of the labeled primer. The 3' end of the quenching probe is modified with a Black Hole quencher. It is critical that the melting temperature of the quenching probe annealed to the labeled primer be well below the temperature of LAMP amplification (typically 60-65 °C) so that the quenching probe dissociates during amplification and does not participate in or inhibit the reaction. After 30 min of incubation at the specified endpoint, the reaction was stopped and moved to room temperature to cool. Upon cooling, for positive samples, the primer-labeled probe was incorporated to the amplicon, and the quenching probe cannot hybridize to it, resulting in a fluorescence output. On the other hand, for negative samples, any free primers that are not incorporated into the amplicon will hybridize with the quenching probe, resulting in a close proximity between the fluorophore and the quenching probe, and the fluorophore is completely quenched. To optimize the assay, the concentration of FIP was fixed at 1.6  $\mu\text{M}$ , and the quenching probe with a concentration ranging from 0 to 2.4  $\mu\text{M}$  was added (Figure 4.5b). We found that the best quenching effect was observed at a quenching probe to FIP ratio of 1.5:1. To investigate the specificity of the reaction system, we examined the effects of mismatches between FAM-FIP probe and Quencher probe. The mismatches are indicated by red letters.

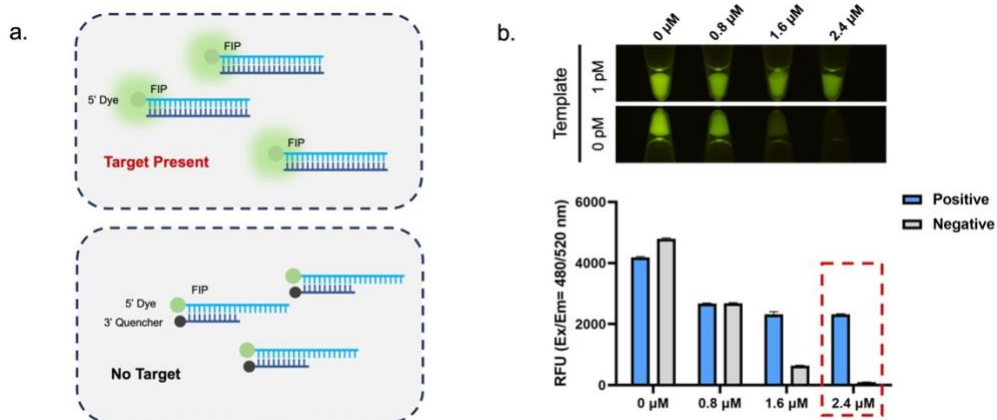


Figure 4.5 a. The schematic of the RT-LAMP reaction using a FAM-FIP probe and Quenching probe. b. The concentration of FIP was fixed at 1.6  $\mu\text{M}$ , and 0  $\mu\text{M}$ , 0.8  $\mu\text{M}$ , 1.6  $\mu\text{M}$ , and 2.4  $\mu\text{M}$  of the quenching probe were added, respectively. The best quenching effect was observed with a quenching probe concentration of 2.4  $\mu\text{M}$  (with a quencher probe to FIP probe ratio of 1.5:1). (mean  $\pm$  SD, n = 3).

Figure 4.6a and Figure 4.6b show the results of the reaction with different numbers of mismatch quencher probes as well as single mismatch quencher probes at different sites.

The negative signal is not fully quenched until the DNA bases are fully matched.

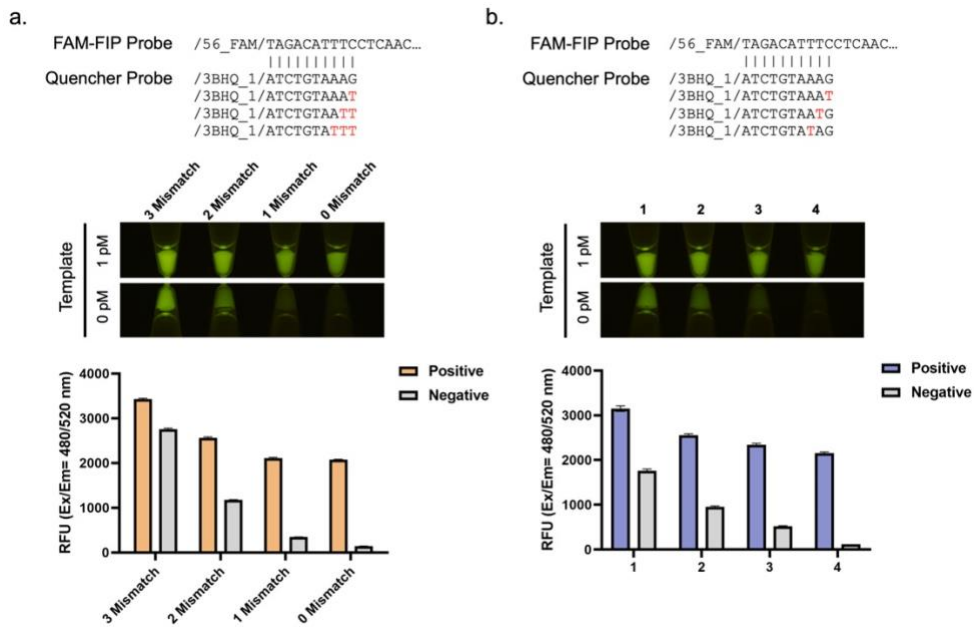


Figure 4.6 a. Comparison of positive and negative results for mismatched sequences of the quencher probe, including fully matched, one mismatch, two mismatches, and three mismatches, demonstrating optimal quenching only when all bases are fully matched (mean  $\pm$  SD, n = 3). b. Comparison of positive and negative results for mismatched sequences of the quencher probe, including 1. 8th mismatch, 2. 9th mismatch, 3. 10th mismatch and 4. fully matched, demonstrating optimal quenching only when all bases are fully matched (mean  $\pm$  SD, n = 3).

#### 4.5 Microfabrication of the integrated Nano digital microfluidic chip

We fabricated the chips using a standard soft lithography process. The mold of the designed microfluidic chips was fabricated on a silicon wafer using SU-8 photoresist (Kayaku Advanced Materials, Inc.). The main channel and vacuum lungs are 200  $\mu\text{m}$  in width and 100  $\mu\text{m}$  in depth. The dimension of each well is 400  $\times$  200  $\times$  100  $\mu\text{m}$  (length  $\times$  width  $\times$

depth). To replicate the patterns onto polydimethylsiloxane (PDMS), elastomer mixture (10:1 weight ratio of Sylgard 184 silicone elastomer base and curing agent) were mixed and degassed in a vacuum chamber. The mixture was then poured on the silicon wafer and placed into an oven at 80 °C for two hrs. Afterward, the PDMS was peeled off from the silicon wafer. The inlet and outlet of the channel were punched with 1 mm diameter holes to allow the reagent to flow through the channel. The final device was sealed in a pretreated glass coverslip by oxygen plasma (Electro-Technic Products) pre-treatment system and baked at 125 °C on a hotplate overnight. After that, hydrophobic modification was made by passivating the microfluidic surface with an anti-biofouling surface treatment to avoid nonspecific absorption of protein/DNA.

The overview of the final LAMP-dChip is shown in Figure 4.7a. Red color food dye was loaded into the chip to facilitate better observation of the shape of the channels. The PDMS channel, vacuum lungs, and wells with 8 nano-liter volumes were replicated from a silicon wafer. Each chip costs ~100 mg of PDMS, which is ~\$0.1 and each glass slide is ~\$0.25. Thus, each chip costs only \$0.35. As shown in Figure 4.7b, the width of the channels and vacuum lungs is 200  $\mu\text{m}$ , and the wells have a dimension of 400  $\times$  200  $\times$  100  $\mu\text{m}$  (length  $\times$  width  $\times$  depth). The whole microfluidic chip has 1,040 wells, and each well is an individual reactor. Figure 4.7c shows the chip fabrication process: SU-8 master with a thickness of 100  $\mu\text{m}$  determines the depth of the channel, vacuum lung, and wells. When loading the microfluidic chip, the sample solution is added into the inlet and extra solution comes out from the outlet. After the sample solution loading, mineral oil is added into the channel to seal the well. The microscope image of the chip with loaded samples under

bright-field illumination is shown in Figure 4.7d. The samples and mineral oil are well separated, which is due to the much greater surface tension of the samples compared to the mineral oil.

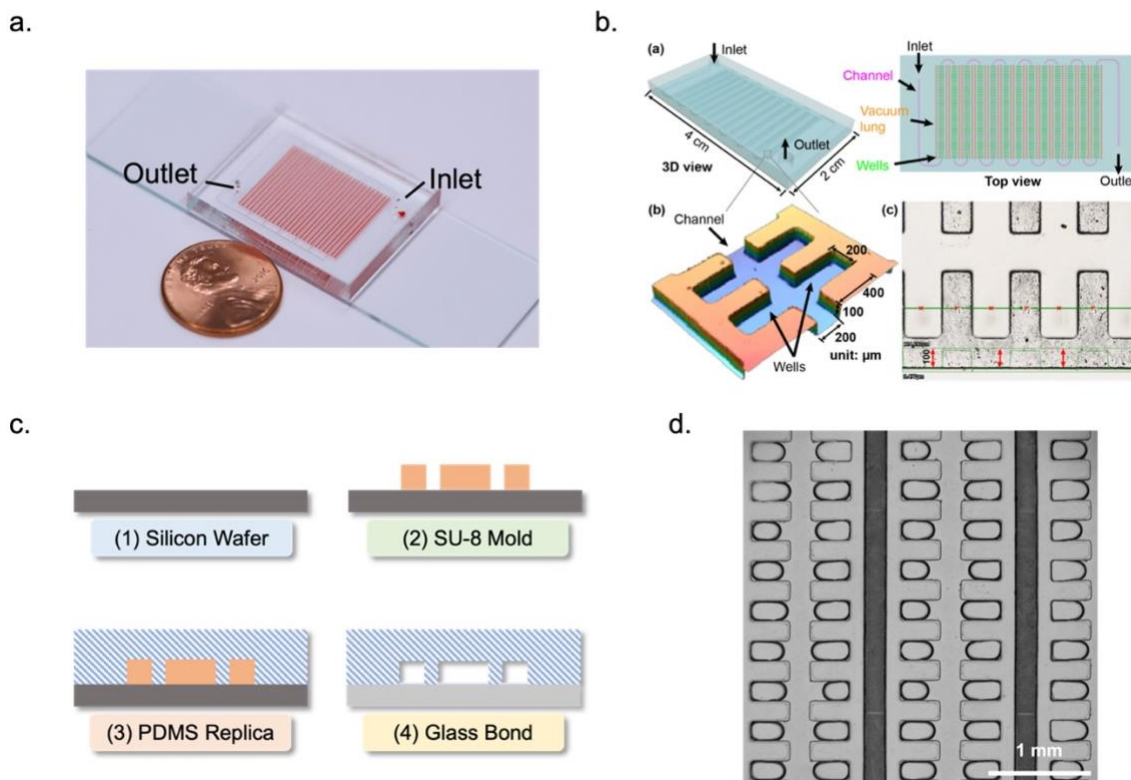


Figure 4.7 a. A photograph of the microfluidic chip, with red food dye load onto it to enhance visibility of the microfluidic channel. b. Design and dimensions of the microfluidic chip, the channels and vacuum lungs have a width of 200  $\mu\text{m}$ , and the wells have a dimension of 400  $\times$  200  $\times$  100  $\mu\text{m}$  (length  $\times$  width  $\times$  depth) that will hold a liquid of 8 nL. The whole microfluidic chip has 1040 wells, and each well will be one individual reactor. c. Chip fabrication step: (1) Silicon wafer used as substate; (2) The negative photoresist SU-8 utilized as a mold; (3) PDMS mixture poured onto the mold to create the channels; (4) PDMS channels bonded on glass substrate to form the chip. d. Microfluidic chip filled with reaction reagent and mineral oil, observed under bright-field illumination.

## 4.6 Characteristics of the Nano-dChip and on-chip reaction

### 4.6.1 Nano-dChip vacuum charging working principle

We incubated the devices at -95 kPa for 15 min in a vacuum chamber before liquid loading experiments. We preloaded 25  $\mu\text{l}$  diluted red food dye into polytetrafluorethylene (PTFE)

tubes. The tubing was connected to the inlet and outlet of the device after taking the devices out of the vacuum. Once the food dye completely filled the wells, mineral oil was injected in to isolate each reaction well. We compared devices with vacuum pump and without vacuum pump. For the on-chip testing, 25 microliters of the RT-LAMP reaction mixture were loaded into the chip using a syringe. After the reaction mixture was loaded, mineral oil was filled into the channels to seal the wells, making each well isolated to avoid evaporation. Then, PCR sealing tape was used to seal the inlet and outlet. The device was placed on a heat block and incubated at 63 °C for 30 min.

The cross section of the chip construction is shown in Figure 4.8a. The system consists of reaction flow channels and lung-like vacuum channels. The vacuum lung mimics alveolar gas exchange by allowing air to diffuse into the vacuum lung through a thin wall of breathable PDMS. The vacuum lung system has no physical connection to the fluid lines and only air diffuses through PDMS. Vacuum lungs are provided at both ends of the flow path to maximize loading efficiency. The auxiliary vacuum lung system assists in loading the microwells as the reactants are loaded into the chip. As shown in Figure 4.8b, dead-end microwells are loaded and segregated. Dead-end loading is crucial because it removes excess air bubbles that can cause pooling or liquid ejection when heated. Mineral oil is then injected into the reaction flow channel to separate each reaction well. Due to the difference in surface tension between the mineral oil and the reaction solution, the mineral oil provides a good separation while avoiding evaporation of the reaction solution. Figure 4.8c and 4.8d illustrate a comparison of mechanisms with and without the vacuum lung loaded. The vacuum lung system provides a more stable and faster sample loading process. It takes only

three minutes for the reaction liquid to be automatically loaded into the chip, while a chip without a vacuum lung cannot be automatically loaded. Air only needs to diffuse through the thin PDMS wall in the vacuum lung, resulting in a more stable pressure gradient than in conventional degassing pumping, where air must diffuse over long distances in a large block of PDMS.

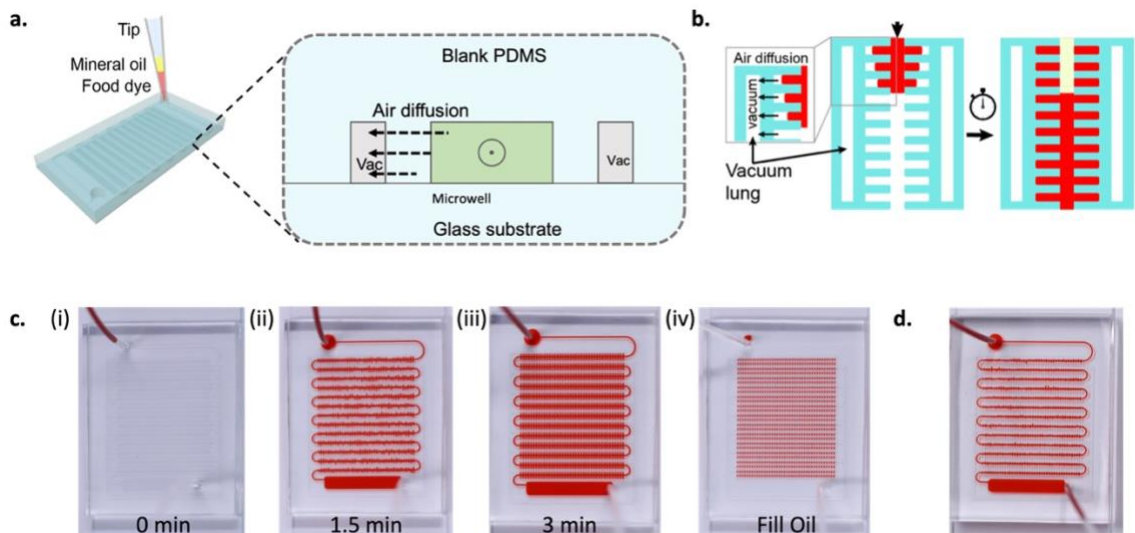


Figure 4.8 Vacuum lung on the chip. a. Side view of the nano dChip design, the vacuum lung design which can remove the reaction reagent into dead-end wells for digital amplification. b. Reaction reagent automatically driven by vacuum lung, after fill with mineral oil, the wells will separate into thousand reaction chambers. c. The design of the vacuum lung enables the reaction reagent to be automatically loaded into the chip in 3 minutes. d. The chips without the vacuum lung cannot automatically load samples.

#### 4.6.2 Quantitative digital amplification of nucleic acid

The one-step quantitative digital detection of norovirus is shown in Figure 4.9a. Our method minimizes the possibility of false-positive signal as the fluorophore quencher molecular probe only fluoresces when amplicons matching the sequence of interest are present. We characterized the distribution of the target in the digital nanofluidic chip with 1 pM concentration. The area and fluorescence intensity of 1,040 wells were analyzed using ImageJ. As shown in Figure 4.9b, the average well area was  $432.7 \pm 42.98 (\times 1000)$

$\mu\text{m}^2$ ) with a 9.9% variation in well area ( $R^2=0.9819$ ). Similarly, Figure 4.9c shows the average fluorescence intensity was  $118,098 \pm 11,351$  a.u., with a variation in fluorescence intensity of 9.6% ( $R^2=0.9787$ ). These results indicate that our digital microfluidic chip has high uniformity across all wells and is ideal for digital fluorescence sensing.

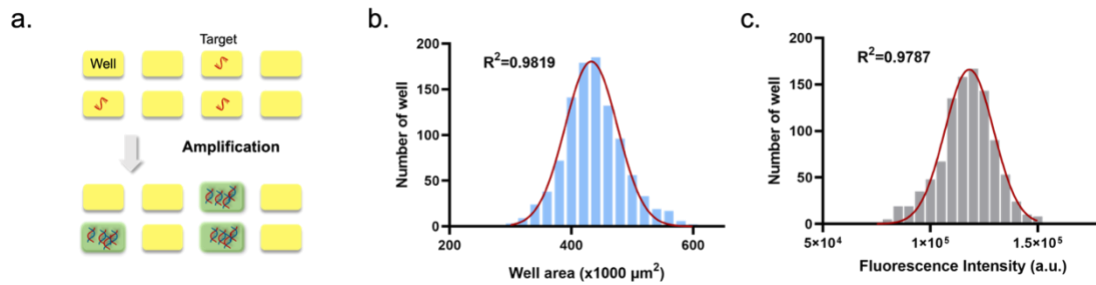


Figure 4.9 Quantitative digital amplification of nucleic acid. a. The concept of digital amplification. Wells have target templates are amplified, whereas others remain unamplified. One can determine the original template concentration by counting the number of amplified wells. Isothermal nucleic acid amplification was done with RT-LAMP. b. the average well area was  $432.7 \pm 42.98$  ( $\times 1000 \mu\text{m}^2$ ) with a 9.9% variation in pore area ( $R^2=0.9819$ ). c. the average fluorescence intensity was  $118098 \pm 11351$  a.u., with a variation in fluorescence intensity of 9.6% ( $R^2=0.9787$ ).

The representative fluorescence images of the nano-dChip are shown in Figure 4.10a. We demonstrate a detection sensitivity of 1 fM within 30 min. Figure 4.10b shows the count number with different concentrations of target RNA, ranging from 1 fM to 10 pM. As shown in Figure 4.9c, a linear relationship was observed between count number and target RNA concentration ( $R^2=0.9363$ ).

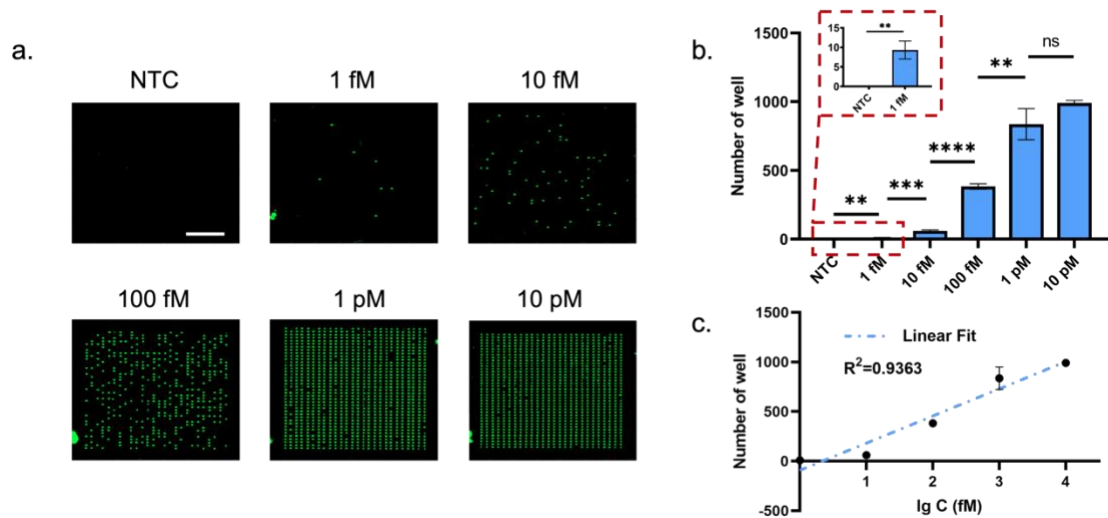


Figure 4.10 a. The end-point fluorescence images of reactions with different starting concentrations of Norovirus RNA. Scale bar, 5 mm. b. The relationship between number of wells and the concentration of the Norovirus RNA (mean  $\pm$  SD, n = 3). c. Calibration curve of the number of wells vs the logarithm of the target concentration (mean  $\pm$  SD, n = 3). The asterisks represent statistical significance according to a *t*-test. \* $P \leq 0.05$ , \*\* $P \leq 0.01$ , \*\*\* $P \leq 0.001$ , \*\*\*\* $P \leq 0.0001$ .

#### 4.6.3 Discussion

We developed a novel nanoliter digital chip (nano-dChip) that can readily digitalize any nucleic acid (DNA and RNA) amplification. This compact, affordable, and disposable device is poised to transform nucleic acid amplification, catering to both DNA and RNA analysis. It is not only suitable for laboratory environments, but can also be applied in real-world scenarios, especially in the rapid detection of representative foodborne pathogens, including human norovirus (ssRNA) on a small single chip. Human noroviruses are the most common viral cause of acute gastroenteritis worldwide. Global outbreaks occurring in the winter seasons caused by the genogroup II, genotype 4 (GII.4) variant are estimated to be in the region of 700 million cases leading to 220,000 deaths annually [162]. Currently, there are no approved vaccines or specific therapeutics to treat the disease. One of obstacles delaying the development of a norovirus vaccine is the extreme diversity presented by noroviruses [163]. In our study, a simple, specific, rapid and sensitive RT-LAMP assay

was established, targeting RNA for the detection of the dominant norovirus genogroup-Nov. GII fragment [164]. Leveraging the LAMP reaction's exceptional specificity with three pairs of six primers and our innovative fluorescence-quencher binding reaction for precise target recognition, our method offers a versatile solution for detecting a wide range of pathogens with shared strains, thus expanding its utility in pathogen detection.

The one-pot fluorescence-quencher reaction system we used is highly specific and greatly reduces the background signal. During amplification, fluorophore-labeled primers are incorporated into the amplicons [165]. It also includes a short quenching probe, usually with 10 bases complementary to the 5' end of the labeled primer. The 3' end of the quenching probe is modified with a dark quencher. Our mismatch experiment results validate the high specificity of the fluorescence probe's reaction with the quenching probe. Excess quenching probe ensures completely quenching of fluorescence in negative reaction. It is critical that the melting temperature of the quenching probe annealed to the labeled primer be well below the temperature of LAMP amplification to dissociate the quenching probes during amplification otherwise they can participate in or inhibit the reaction. We also found that the length of the quenching probes should be appropriate as too long is not conducive to primer binding and prone to secondary structures, and can even inhibit the reaction [166]. While too short results in poor specificity, e.g., shorter than five bases, and cannot provide effective quenching. In addition, for the quenching probe design it is important to avoid having too many GCs and prevent three consecutive Cs or Gs; consecutive CGs are not conducive to quenching probe binding with the primer. The  $\Delta G$  value should be greater than -9 kcal/mol to avoid self-dimer formation [167]. In addition,

due to the high specificity of our detection method, it provides an excellent strategy for studying the diversity and genotypes of viruses with many similar strains or variants.

One of the key innovations of our nano-dChip is the digitalization of amplification products, which simplifies operation and significantly improves analytical sensitivity, quantitative accuracy, and resistance to sample-related inhibition, surpassing various traditional amplification chemistry methods [168]. Quantitative detection of nucleic acids is crucial in basic life science research and medical diagnosis. Compared to widely used qPCR, the nano-dChip detection method does not require external standards and has advantages in both direct and absolute quantification. Additionally, the design of the reaction wells effectively segregates the reaction reagent into distinct small reaction chambers. This segregation prevents interference between chambers, mitigating the risk of cross-contamination and ensuring the integrity of the results. The nano-dChip amplification detection method analyzes reaction wells to count nucleic acid molecules, providing absolute quantification of nucleic acids. The linear response between input and measured nucleic acid concentrations is excellent within a certain range ( $R^2 = 0.9363$ ), indicating precise nucleic acid quantification.

An ideal foodborne pathogen assay would provide untrained operators with a rapid, inexpensive, highly sensitive on-site method for assessing the microbiological safety of food products with little or no sample preparation or purification [162]. Our sensing strategy is performed on a small chip without the need for expertise to operate, making it accessible to a wide range of users. This equipment-free microfluidic system offers

numerous advantages such as simple, inexpensive, integrated, portable, and rapid. The fabrication of the nano-dChip relies on standard microfabrication, driving down production costs to less than \$0.50 USD per unit. This affordability makes it feasible for widespread distribution and disposable use, eliminating the need for costly equipment maintenance and reducing the overall cost of molecular analysis. In the future, the device can be hermetically sealed in aluminum vacuum packaging using a vacuum sealer for long-term storage or transportation purposes [169].

In the next phase of development, the chip holds potential for a wide range of applications, including the real-time detection of various pathogens, viruses, and bacteria [170]. By incorporating multiple quencher primer sets tailored to different targets, the chip enables spectrally multiplexed detection, enhancing its versatility and utility [165]. Furthermore, the device can expedite rapid multiplexed nucleic acid screening in hospital intensive care units, facilitating timely diagnosis and treatment decisions [171]. Looking ahead, we envision leveraging simple and portable commercially available fluorescence microscopes to read fluorescence results, eliminating the need for bulky and expensive instruments [172]. Additionally, employing a machine learning approach for quantification holds promise, with potential applications in image classification for automatic data processing and quantitative analysis [173]. This integration of advanced technologies underscores the chip's potential to revolutionize diagnostics, making it more accessible, efficient, and accurate in various clinical settings.

## **Chapter 5. 3D Digital chip for simple and highly quantitative detection of HPV DNA**

### **5.1 Introduction**

Infection with human papillomavirus (HPV) almost invariably leads to all cases of cervical cancer, making cervical cancer the fourth most common cancer in women globally [174]. Particularly, the two most common high-risk genotypes HPV16 and 18 are responsible for over 70% of cervical cancer cases [175]. The diagnosis of cervical cancer through polymerase chain reaction (PCR) testing has high sensitivity (94.6%) and specificity (96.8%). Due to its elevated sensitivity and specificity, HPV DNA testing has become an integral part of the gold standard for cervical cancer diagnosis [176]. In recent years, nucleic acid isothermal amplification detection has emerged as a promising alternative to traditional PCR due to its simplicity, speed, cost-effectiveness, and high sensitivity [177]. Various nucleic acid isothermal amplification methods have been developed, including loop-mediated isothermal amplification (LAMP) [178], recombinase polymerase amplification (RPA) [179], rolling circle amplification (RCA) [180], and nucleic acid sequence-based amplification (NASBA) [181]. Even though highly promising, most isothermal amplification detection methods have limitations such as a lack of quantitative detection capabilities, occasional unexpected non-specific amplification signals, and relatively high background signals [182].

LAMP is one of the most widely applied isothermal amplification technologies in pathogen diagnostics [183]. The advantages of the LAMP reaction include high sensitivity and multiple primers, which have exceptionally high specificity because at least a set of four

primers with six binding sites must hybridize correctly to their target sequence before DNA biosynthesis occurs [142]. The reaction temperature is around 63°C, which avoids undesirable pre-amplification at room temperature [170]. In addition, it exhibits strong tolerance to inhibitors. Traditional detection methods relying on intercalating dyes like EvaGreen or SYBR Green can directly detect amplified targets but have drawbacks such as low selectivity and can inhibit the amplification reaction, thus requiring post-reaction addition, and this can cause false positives if added after opening the reaction chamber [184]. To address these issues, energy transfer-labeled oligonucleotide probes for sequence-specific fluorescence detection have been developed to improve the amplification process. We introduce an innovative ribonuclease-dependent cleavable (fluorophore–quencher) FQ LB primer designed to augment the sensitivity and specificity of LAMP detection. This primer undergoes cleavage exclusively upon recognizing a specific nucleic acid sequence, thereby markedly enhancing detection specificity, and minimizing background signal.

Digital micro- and nanofluidic chips have been developed in recent years with advantages such as greater tolerance to inhibitory substances, higher sensitivity, and more accurate detection [185]. The combination of digital chips and nucleic acid amplification methods enables absolute quantification analysis of nucleic acid targets by distributing target molecules into small wells or droplets. When dividing the sample into countless aliquots, those aliquots contain no target molecule or only one molecule. The target molecule concentration can then be derived from counting the number of positive aliquots. The isolation of aliquots eliminates the competition of primers and probes, which is especially

important for detecting minute DNA targets [186]. Currently, there are mainly two strategies for generating isothermal reaction units, one of which involves using chamber microfluidic chips to generate reaction units. However, due to manufacturing process limitations, the number of chambers in microfluidic chips is limited, or the chamber volume is relatively large, leading to restricted dynamic range [187]. The other strategy involves using droplet microfluidic chips to generate monodisperse droplets. However, the process of droplet formation is relatively complex, and the stability of the droplets poses issues, making real-time reaction monitoring a significant challenge [188].

Here, we show a novel energy transfer-labeled oligonucleotide probe with improved fluorescence changes to create a highly sensitive and specific isothermal amplification of nucleic acids for sensitive and quantitative detection of HPV 16 DNA in plasmid mimic samples. The digital warm start assay is established through LAMP-based reaction into sub microliter aliquots within a digital nanofluidic chip. This reaction is a one-pot format FQ labeled primer isothermal amplification-based detection, preventing premature target amplification at room temperature and enabling accurate digital quantification of nucleic acids. Separation of aliquots eliminates competition between primers and probes and largely reduces false positive signals. Machine learning facilitates the straightforward derivation of quantitative relationships for target concentrations from the analysis. Our developed combination of the assay and nanofluidic chip allows for highly sensitive and uncomplicated detection of HPV 16. This system is poised for adaptation in hospitals or point-of-care settings for the quantification of sexually transmitted infections.

## 5.2 Characteristic of silicon chip and principle of digital chip

The schematic of the digital nanofluidic chip based on the one-step LAMP assay is shown in Figure 5.1a. The primers were designed to amplify a 271 bp HPV 16 L1 fragment gene sequence (GenBank accession MT316211.1). The FQ-LAMP reaction mixture was first prepared in an Eppendorf tube. The prepared reaction mixture was then distributed into a QuantStudio 3D digital chip. The 3D digital chip is a 10 mm<sup>2</sup> high-density reaction plate that has a single array of 20,000 reaction microwells. Each microwell has a diameter of 60 μm and a depth of 500 μm (Figure 5.1b). The chip was pretreated with hydrophobic coating on the chip surface to enable the loading and isolation of the LAMP reactions within the microwells. After the addition of the reaction reagent, an oil layer was applied to cover the chip. This step not only facilitates the straightforward isolation of each reaction microwell but also serves as a preventive measure against contamination and reagent evaporation. Following a 45-minute incubation at 63°C, microwells containing the target DNA exhibit a green fluorescence signal attributed to successful target amplification, while microwells lacking the target remain devoid of such fluorescence.

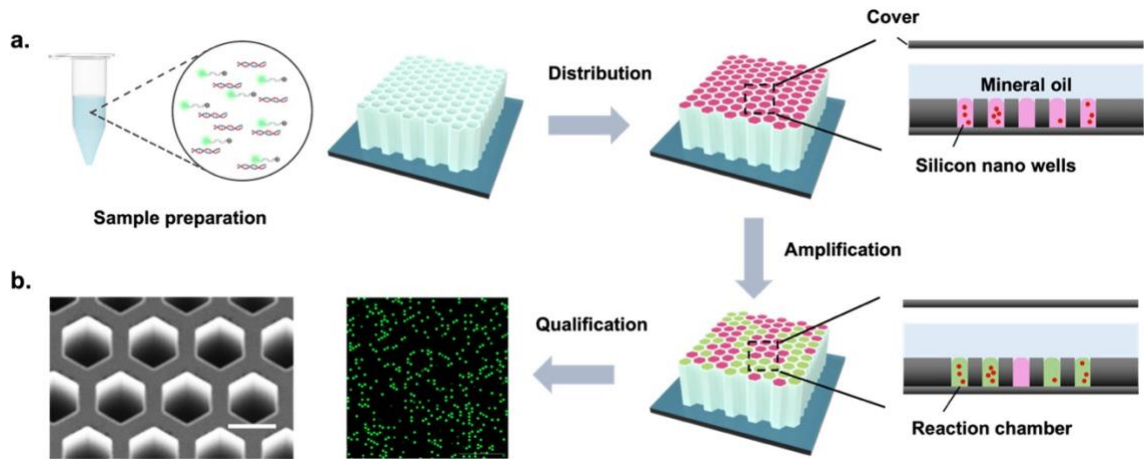


Figure 5.1 a. Schematic illustration of FQ LAMP assay. One-pot reaction mixture is first prepared in one tube. The sample mixture then distributed randomly into over ten thousand of microwells. When incubated

at 63 °C, each micro reaction with plasmid HPV 16 DNA target undergoes a reaction and generates strong green fluorescence (positive spots), whereas not in those without target (negative spots). Through detecting and counting the positive micro reactions (or spots), plasmid HPV 16 DNA can be quantified based on the proportion of positive spots. b. SEM image of micro digital chip, Scale bar is 60 μm. Reprinted from [189]

### 5.3 Analytical sensitivity and specificity of FQ-LAMP assay

**Figure 5.2** shows the schematic of the FQ probe-based LAMP reaction. This assay was developed with the designation of two sets of primers to specifically detect the HPV 16 DNA target. Five sets of the LAMP primers (FIP, BIP, F3, B3, and LB) were designed according to the distinct regions of the HPV 16. In the present study, two different types of LBs were constructed: the LB probe is the traditional probe with unlabeled ends. The other probe, named the FQ LB probe, has the same sequence as the LB probe but was tagged with FAM fluorophore at the 5'-end and Iowa Black® RQ quencher at the 3'-end. This probe is quenched at the unbound state and fluoresces only when annealed to the specific complementary regions during the amplification process. The quencher functions to inhibit the fluorophore from emitting signals when they are close to each other. The fluorophore and quencher were placed further from each other to allow it specifically annealing the stem loop region of the dumbbell like LAMP amplicons. As the probe is longer than 20 base pairs, it was designed with an additional internal quencher, that is, an internal quencher /ZEN/ positioned in the middle of the strand. This design was intended to reduce the assay's crosstalk signal, increase the amplification signal, and produce a lower background noise.

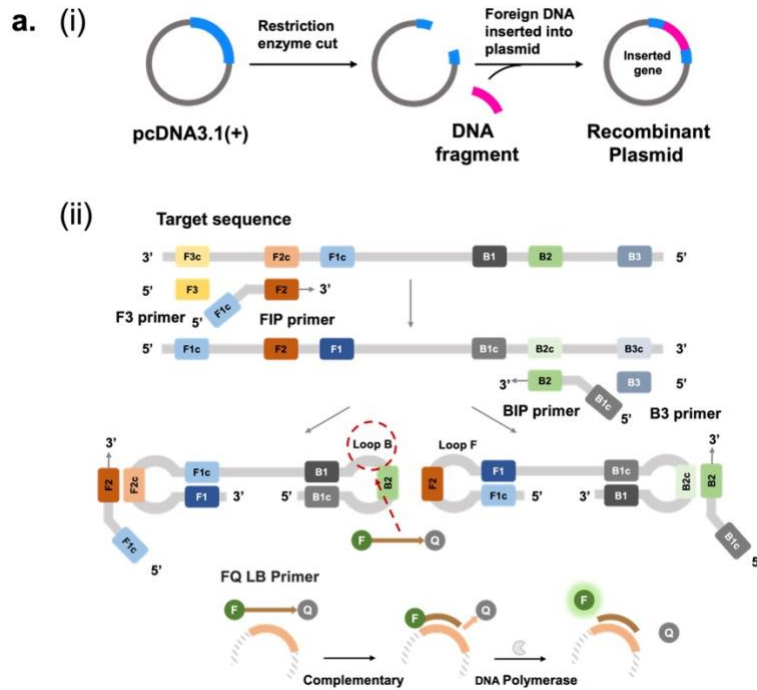


Figure 5.2 a. (1) 450-base pair (bp) sequences of HPV-L1 gene from HPV16 insert into plasmid cDNA3.1(+) vector. (2) Principle of the FQ-LAMP assay. In the assay, LAMP's loop backward (LB) primer was used to design the FQ LAMP probe, the target sequence recognition and enhanced fluorescence detection of the FQ LB probe. Reprinted from [189]

As shown in **Figure 5.3a** and **Figure 5.3b**, the optimal concentration of the LB and FQ LB primers and the optimal ratio of LB primer to FQ LB primer are 0.4  $\mu\text{M}$  and 1:1, respectively.

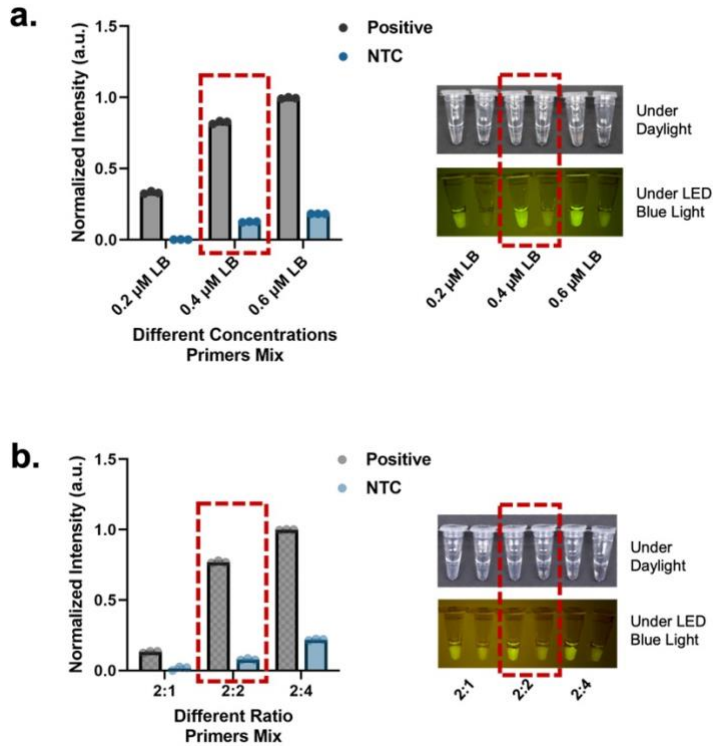


Figure 5.3 a. The LAMP conditions were optimized for the reaction with a mixture of LB/FQ LB primers at concentrations of 0.2, 0.4, and 0.6  $\mu\text{M}$ , respectively. b. The LAMP conditions were optimized for the reaction with a mixture ratio of LB/FQ LB primers were 2:1, 2:2, and 2:4, respectively. For each concentration's testing, error bars denote the standard deviation ( $n = 3$ ). The asterisks represent statistical significance according to a t-test. \* $P \leq 0.05$ , \*\* $P \leq 0.01$ , \*\*\* $P \leq 0.001$ , \*\*\*\* $P \leq 0.0001$ . Reprinted from [189]

The fluorescence intensity was measured for the target DNA concentration ranging from 10 aM to 1 pM (**Figure 5.4a**), and the positive reaction was clearly observed in the 1 fM sample with both naked eye detection and UV illumination. **Figure 5.4b** shows the comparison of the fluorescence intensity for positive and negative targets (1 pM), and a clear difference between positive (HPV16) and negative groups (HPV 18 and NTC) is observed.

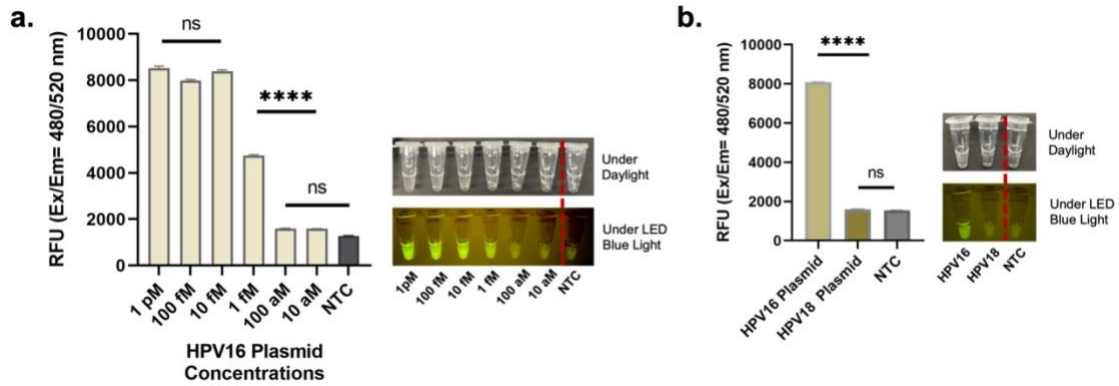


Figure 5.4 a. Endpoint fluorescence detection of the FQ LAMP after 45-min amplification of various concentrations of plasmid HPV 16 DNA targets, from 10 aM to 1 pM. b. Endpoint fluorescence detection of the Plasmid HPV 16 DNA target (1 pM) compared with plasmid HPV 18 DNA target (1 pM) and no template control. For each concentration's testing, error bars denote the standard deviation ( $n = 3$ ). The asterisks represent statistical significance according to a t-test. \* $P \leq 0.05$ , \*\* $P \leq 0.01$ , \*\*\* $P \leq 0.001$ , \*\*\*\* $P \leq 0.0001$ . Reprinted from [189]

## 5.4 On-chip reaction

On-chip isothermal digital amplification assay: The digital nanofluidic chip is a 10 mm<sup>2</sup> high-density reaction plate that has a single array of 20,000 reaction microwells with 15  $\mu$ l volume for each well. The 15  $\mu$ l reaction mixture contained 1.5  $\mu$ l of 10 x Isothermal Amplification Buffer, 0.9  $\mu$ l of MgSO<sub>4</sub> (100 mM), 2.1  $\mu$ l dNTP mix (10 mM), 1.5  $\mu$ l of 10 x target-specific primer mix (FIP/BIP 16  $\mu$ M, F3/B3 2  $\mu$ M, LoopB 4  $\mu$ M, FQ probe 4  $\mu$ M), 0.6  $\mu$ l of Bst 2.0 WarmStart DNA Polymerase (8000 U/ml), 1.2  $\mu$ l of target DNA, and 7.2  $\mu$ l of nuclease-free water. After assay mixing, the 15  $\mu$ l reaction liquid was loaded into the chip and mineral oil was used to seal the loading port. The device was placed on a heat block and incubate at 63°C for 45 min.

Data acquisition and analysis: After incubation, the chip was quantified using a BioTek Cytation 5 Cell Imaging Multimode Reader (Agilent, CA, USA) with a 4x magnification

objective. Every image was captured in about 30 s of laser irradiation, and the irradiation was turned off until the next imaging. Five distinct regions (3.5 x 3.5 mm) without overlapping areas were randomly captured by the microscopy to cover about 2,750 microwells. The number of the positive spots and corresponding fluorescence intensity were measured by using the ImageJ software (bit depth: 8 bits; 1,992 x 1,992 pixels). GraphPad Software Prism 9.5.1 was used to plot real-time fluorescence curves, analyze linear regression, and verify statistical significance between different assay groups.

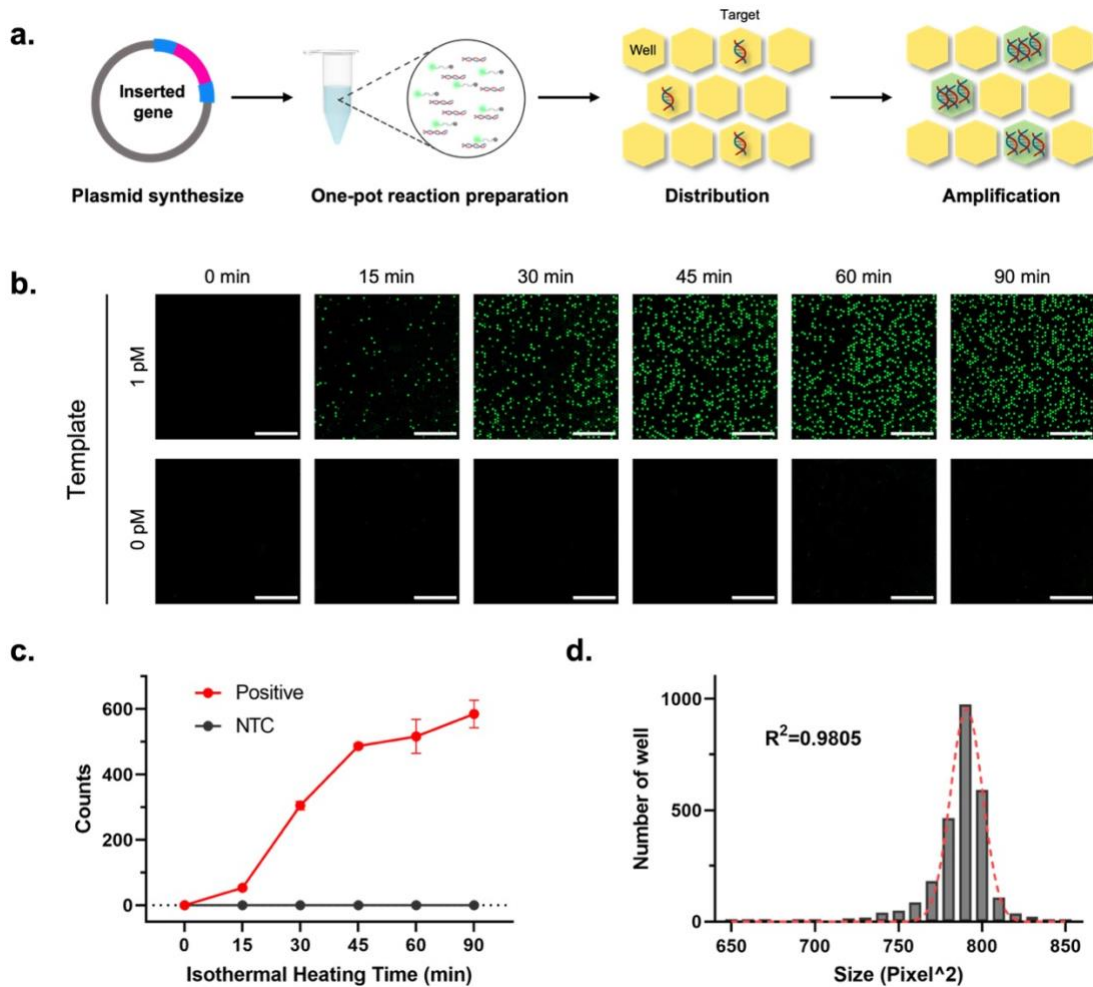


Figure 5.5 a. The concept of digital amplification. Wells that have at least one or more target templates are amplified, whereas others remain unamplified. One can determine the original template concentration by counting the number of amplified wells. Isothermal nucleic acid amplification was done with LAMP. b. Endpoint fluorescence micrographs of the QuantStudio digital chip for the HPV 16 detection with various incubation time (0, 15, 30, 45, 60 and 90 min) at 63 °C. 1 pM plasmid HPV 16 DNA and no template

control were loaded. Scale bar, 1 mm. c. The average positive spots increase to a detectable level within 15 min, and when the time was greater than 45 min, there was no significant change in the positive spots. Error bars denote the standard deviation ( $n = 5$ ). d. Histogram of well area conforming to Gaussian distribution ( $R^2=0.9805$ ), 10 pM plasmid HPV 16 DNA target was loaded, proofing the chip has the high uniformity of all wells. Reprinted from [189]

Analytical sensitivity and specificity of FQ-LAMP assay on digital chip: After optimizing the reaction conditions off-chip, the analytical performance of the microwell chip was investigated. **Figure 5.5a** illustrates the typical workflow of the FQ-LAMP assay, encompassing the synthesis of DNA Plasmid, preparation of a one-pot LAMP reaction mixture, distribution of the reaction mixture into the chip, and on-chip incubation at 63°C. **Figure 5.5b** shows the images of the reactions under a microscope with various incubation times (e.g., 0, 15, 30, 45, 60 and 90 min) by using 1 pM HPV plasmid as a target. As shown in **Figure 5.5c**, a 45-min incubation is enough for the FQ probe LAMP assay to reach the maximum percentage of the positive spots. The uniformity of the microwell volume was also characterized by ImageJ. As shown in **Figure 5.5d**, the average well area was  $790.7 \times 9.633 \text{ Pixel}^2$ , which conforms to a Gaussian distribution ( $R^2=0.9805$ ).

By testing various concentrations of HPV 16 DNA plasmid target, the on-chip detection sensitivity was also investigated. As shown in **Figure 5.6a**, the digital FQ LAMP assay was performed with a target concentration ranging from 100 aM to 100 pM, and it can directly be observed by counting the positive spots shown under the microscope. We are able to detect the HPV 16 target with a concentration as low as 1 fM, and the signal is saturated with a concentration greater than 10 pM. The specificity of the digital LAMP assay was also carried out by using similar strains. As shown in Figure 36c, positive spots are observed in the chip loaded with the HPV 16 positive control, whereas not for those

negative control samples, such as the HPV 18 control and the no template control, which is consistent with our off-chip results. In addition, the digital nanofluidic chip shows highly quantitative readings with a target concentration range from 1 fM to 10 pM (**Figure 5.6b**), demonstrating a dynamic range of 5 orders of magnitude. Moreover, notable distinctions exist in the specificity of HPV target detection when compared to other strains (**Figure 5.6c and Figure 5.6d**).

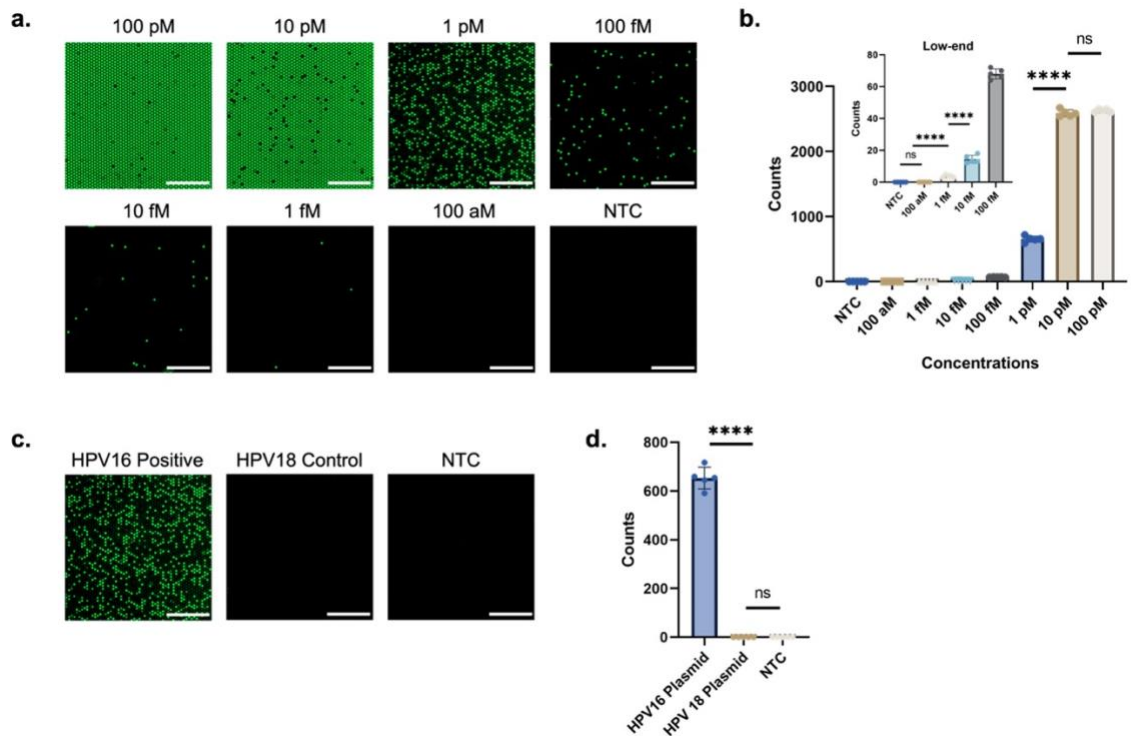


Figure 5.6 a. End-point fluorescence images of reactions with different starting concentrations of plasmid HPV 16 DNA target within 45 min incubation at 63 °C. Scale bar, 1 mm. b. Quantification range of the digital chip. The relationship between positive spots (Y) and concentration of targets (X), from 100 aM to 100 pM. The low-end shows the enlarged view of low concentration range from 100 aM to 100 fM. c. End-point fluorescence images for the specificity detection. Plasmid HPV 16 PC, Plasmid HPV 18 control and no template control. Scale bar, 1 mm. d. Detection specificity of the Plasmid HPV 16 DNA target (1 pM) compared with plasmid HPV 18 DNA target (1 pM) and no template control. For each concentration's testing, error bars denote the standard deviation (n = 5). The asterisks represent statistical significance according to a t-test. \*P ≤ 0.05, \*\*P ≤ 0.01, \*\*\*P ≤ 0.001, \*\*\*\*P ≤ 0.0001. Reprinted from [189]

## 5.5 Computer vision enables precise analysis

The entire pipeline for processing images and classifying the testing samples is shown in **Figure 5.7**. To estimate target concentrations from sample images, we first inputted a dataset of training images showcasing results. These images are crucial for creating a baseline for the system's understanding of target appearances at various concentrations. Next, template matching algorithms were applied to detect samples within these images due to the spatial hexagon shape property of each individual sample. We slide this hexagon template across the entire sample image to detect individual samples. This precise detection is critical for accurate analysis. The detected samples were sorted based on image intensity levels, arranging them from high intensity to low intensity. This sorting is essential to standardizing the analysis across different samples, as the sample image intensity is highly correlated to the target concentration. Subsequently, the intensity values of all samples were normalized to account for variations in target concentration. This normalization ensures consistent and reliable data fed into the neural network. Finally, a Convolutional Neural Network (CNN) was trained using these normalized images. The CNN learns the patterns and correlations between the visual characteristics of the target samples and their known concentrations. This learning enables the network to accurately estimate target concentrations in new, unseen images. Eventually, we composed the target concentration result for each individual sample to an entire training sample image dataset with thousands of individual samples and visualize the target concentration distribution. With this learning, our system can correctly identify all the positive and negative samples, and the network can accurately estimate the target concentration in unseen images.

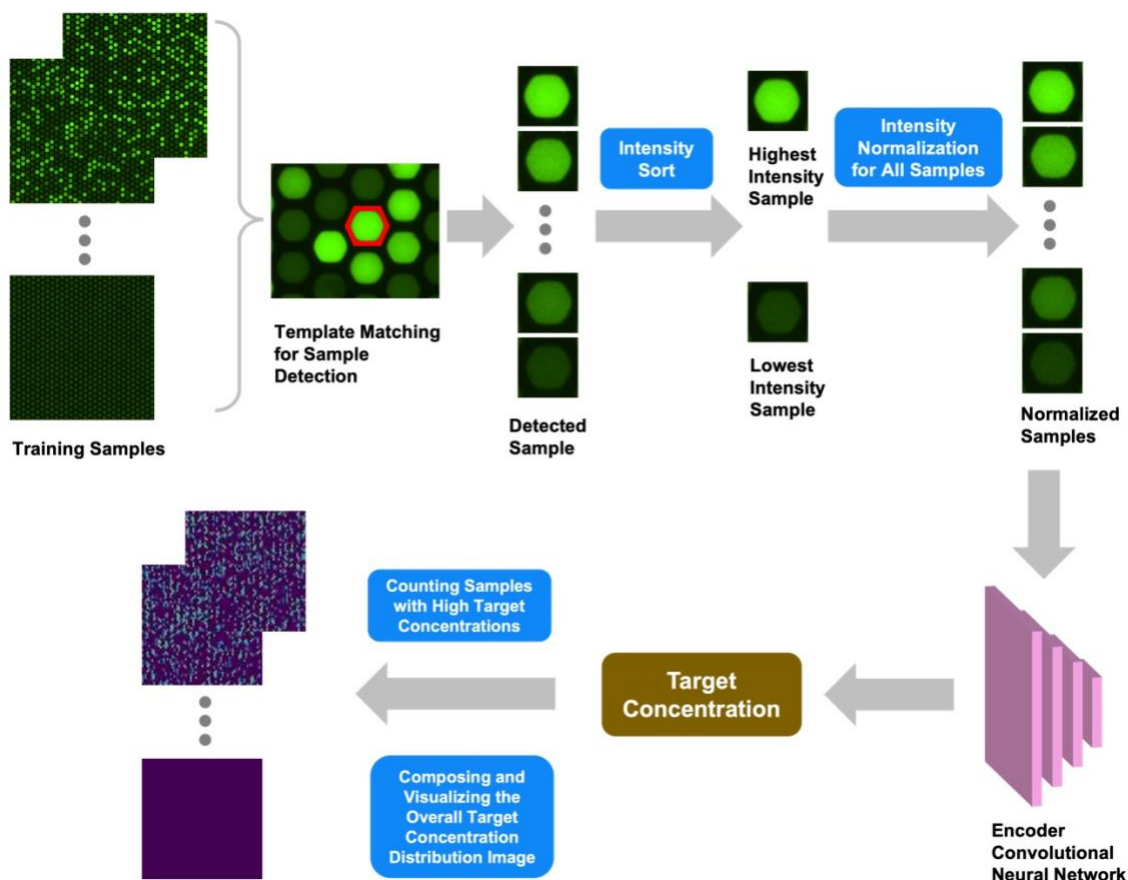


Figure 5.7 Image processing and testing result classification pipeline of computer vision enabled HPV target sensing on Digital Nanofluidic Chip, which involves feature generation, intensity range selection, and feature classification. Reprinted from [189]

## 5.6 Highly quantitative nucleic acid detection and analysis

In this study, we developed a novel energy transfer-labeled oligonucleotide probe to create a highly sensitive and specific isothermal amplification assay for nucleic acids detection. We applied it in a digital nanofluidic chip to enable rapid quantitative detection of HPV targets. FQ LB is a single fluorophore and quencher-labeled oligonucleotide probe that can be cleaved by ribonuclease, simultaneously initiating rapid nucleic acid amplification and generating sequence-specific fluorescence. The devised assay is conducted as a single step within a closed one-pot procedure, mitigating the risk of carryover or cross-contamination

arising from post-amplification procedures. The quencher restricts the signals by the fluorophore when they are in close proximity. The probes employed in our approach are quenched in the unbound state and emit fluorescence exclusively upon annealing to a specific complementary region during the amplification process, ensuring high sequence specificity. For LB probes shorter than 20 nucleotides, labeling is limited to the ends, while those exceeding 20 nucleotides incorporate an internal quencher at the midpoint, which would otherwise not be quenched due to the length of the DNA strand. This design reduces crosstalk, enhances amplification, and diminishes background noise [190]. In addition, the use of FQ probes does not require a complex pre-processing procedure. Due to the complexity of distinguishing non-specific LAMP amplicons from target amplicons, FQ probes are more specific than conventional LAMP assays using DNA intercalating dyes and can significantly reduce background signals. Therefore, this study reveals the benefits of using FQ LB probes to improve amplicon detection in LAMP assays.

We developed a robust digital amplification system for easy identification of detection targets. This method is a simple patterning method that is unique in its ability to concentrate reagents in a small size. Because the target molecules are assigned to numerous small, separated reaction reservoirs, the positive and negative reservoirs can easily be distinguished from each other without interference. The system is more tolerant to reaction inhibitors, as the potential reaction inhibitors are separated from the reaction mixture, reducing the amplification reaction inhibition in the digital assay and making it well-suited for the detection of low-level targets. We found that due to the multiprobe of the conventional LAMP assays, reactions in Eppendorf tubes are more susceptible to non-

specific amplification due to the cross-linking of amplicons, and aerosols generated during the reaction may cause contamination, leading to false positives [191]. In contrast, no false-positive signals were found in the reaction system of our digital nanofluidic chip. Therefore, digital detection can directly detect nucleic acid in many samples without complicated sample pre-treatment and nucleic acid purification processes.

Our microliter digital microwells enable the quantitative detection of nucleic acids without the need for calibration curves, thereby improving the accuracy of detecting low-copy nucleic acid templates. We found that conventional reactions in Eppendorf tubes are difficult to achieve accurate quantitative detection and are more suitable for qualitative detection [192]. In contrast, the microliter digital microarray reaction allows for easy quantitative distinction across five magnitude orders ranging from 1 fM to 10 pM. The ability to quantitatively detect nucleic acids without relying on calibration curves is a key feature that enhances accuracy, particularly in low-copy nucleic acid template detection. In addition, compared to droplet microfluidic chips that produce monodisperse droplets, fixed-structure chambers are more stable and suitable for real-time monitoring [193]. The compartmentalization of nucleic acid in digital detection enables individual amplification and detection, enhancing sensitivity to the single-molecule level. This surpasses the sensitivity achievable with traditional isothermal amplification reactions, which often require intricate primer screening and probe optimization. Currently, we have labeled different targets with different fluorophores and quenchers, allowing them to be detected simultaneously on different fluorescent channels of a real-time monitoring system [194].

We have developed a computer vision-based data analysis system. Through this learning process, our system correctly identifies both positive and negative samples, and the network can also accurately estimate the concentration of targets in unseen images. In the end, the classification accuracy of separating detected positive samples from negative samples is 100%. Our method integrates image processing and deep learning techniques, making it a robust and powerful tool for analyzing target concentrations, which has important applications in areas such as molecular detection and clinical diagnosis. The application of computer vision in biosensors has great prospects, as it enables large-scale, automated, high-throughput, and multi-target detection compared with the traditional analysis methods [173]. The prospect of enhancing sensitivity, specificity, and efficiency in biosensing through computer vision signifies a significant leap forward in the realm of diagnostic and analytical methodologies. It stands as a vital tool for the future development of traditional biosensors toward intelligent biosensors.

## **Chapter 6. Conclusion: Micro Biosensing platform to fundamentals and applications**

### **6.1 Conclusions**

Micro biosensing platforms represent a cutting-edge fusion of biology and microengineering, enabling highly sensitive and rapid detection of a wide range of analytes [195]. By harnessing the remarkable specificity and sensitivity of biological molecules such as enzymes, antibodies, and nucleic acids, these platforms can accurately identify target molecules even at very low concentrations. This capability is further enhanced through the integration of microfabricated structures, which facilitate precise signal transduction and amplification. Techniques like microfluidics enable precise manipulation of tiny fluid volumes, enhancing the efficiency and accuracy of the detection process. Electrochemical sensing allows for the conversion of biological recognition events into electrical signals, while optical detection methods utilize light-matter interactions to detect and quantify analytes with high precision. Together, these technologies form the foundation of micro biosensing platforms, enabling real-time analysis with unparalleled sensitivity and specificity.

The applications of micro biosensing platforms are incredibly diverse and far-reaching. In the field of medical diagnostics, these platforms are revolutionizing healthcare by enabling rapid and accurate detection of disease biomarkers, facilitating early diagnosis and personalized treatment strategies [196]. In environmental monitoring, micro biosensing platforms play a crucial role in detecting pollutants, toxins, and pathogens in air, water, and soil, thereby aiding in environmental conservation and public health protection [197].

Moreover, in the realm of food safety, these platforms ensure the timely detection of contaminants and adulterants, safeguarding food quality and preventing potential health risks for consumers [104]. Additionally, micro biosensing platforms are invaluable in security applications, where they are utilized for the detection of chemical and biological threats, enhancing safety measures in critical infrastructure and public spaces [198]. Their portability and cost-effectiveness make them particularly well-suited for point-of-care testing in resource-limited settings, enabling timely intervention and disease management.

The future direction of biosensing platforms is poised to witness significant advancements driven by several key trends. Firstly, there will be a focus on enhancing sensitivity and selectivity through the integration of novel biological recognition elements and advanced nanomaterials [199]. Additionally, the development of multiplexed detection capabilities will enable simultaneous analysis of multiple analytes, enhancing the versatility and efficiency of biosensing platforms [200]. Moreover, the miniaturization and integration of components will lead to the emergence of more portable and wearable biosensing devices, facilitating point-of-care diagnostics and personalized healthcare monitoring [201]. Furthermore, there will be increasing emphasis on the development of biosensing platforms capable of interfacing with digital health systems, enabling seamless data collection, analysis, and interpretation. Lastly, the incorporation of artificial intelligence and machine learning algorithms will play a crucial role in optimizing biosensing performance, enabling real-time data analysis, and unlocking new insights into complex biological processes [202]. Overall, the future of biosensing platforms holds great promise in revolutionizing

healthcare, environmental monitoring, and various other fields by providing accurate, rapid, and cost-effective analytical solutions.

## **6.2 Future perspective in virus detection**

Computer vision has become a powerful tool in the field of biosensing, aiding in the development of innovative and precise systems for the analysis and interpretation of biological data. This interdisciplinary approach harnesses the capabilities of computer vision algorithms and techniques to extract valuable information from various biosensing applications, including medical diagnostics, environmental monitoring, food health, etc. Despite years of development, there is still significant room for improvement in this area. In this perspective, we outline how computer vision is applied to raw sensor data in biosensors and its advantages to biosensing applications. We then discuss ongoing research and developments in the field and subsequently explore the challenges and opportunities that computer vision faces in biosensor applications. We also suggest directions for future work, ultimately underscoring the significant impact of computer vision on advancing biosensing technologies and their applications.

### **6.2.1 How computer vision benefit biosensors**

Biosensors are analytical devices that combine biological elements with transducers to detect and quantify specific biological or chemical substances. They are used in a wide range of applications, including medical diagnostics [35], [203], [204], chemical substance detection [205], [206], [207], environmental monitoring [208], [209], [210], food safety

[211], [212], [213], and biotechnology [214], [215], [216]. In the past few decades, biosensors have grown significantly with the advancements of nanotechnology [217], [218], [219], signal amplification strategies [220], and hardware [221]. For example, nanomaterial-based electrochemical signal amplification has great potential to improve the sensitivity and selectivity of biosensors [105]. However, all biosensors inevitably have drawbacks such as irregular signal noise, poor stability, difficult integration, and automation [222]. Therefore, researchers are seeking other breakthroughs to improve the performance of biosensors. Here, we survey the intersection of computer vision and biosensing, focusing on research in biosensing imaging, as well as based on 2D image signals such as electrochemical signals, spectral signals, which represents the vast majority of current computer vision applications for biosensors. Computer vision is a field of research that focuses on enabling computers to interpret and understand visual information in images or videos. It involves the development of algorithms, techniques, and models to extract meaningful information from visual data [223]. The application of computer vision improves the ability to analyze and interpret data, thereby enhancing the performance of biosensors [224]. For example, it can provide highly accurate analysis and detection that can help overcome the specificity and selectivity problems of the sensors themselves [225]. Another advantage is it can efficiently process extensive sensing data with complex matrices or samples, which can significantly improve the efficiency and speed of data collection [226]. It also provides real-time monitoring with the advantages of being non-invasive, automated, and high throughput [227]. These advantages make computer vision a vital tool in the field of biosensors and will be a way to transform conventional biosensors

into intelligent biosensors. **Figure 6.1** shows the overview of the progress, challenges, and prospects for computer vision in biosensor applications.



Figure 6.1 Overview of the progress, challenges, and prospects for computer vision in biosensors application. Reprinted from

Computer vision can analyze raw sensing data from biosensors in several ways: (1) Classification: Algorithms can classify sensed signals into different categories based on the target analyte. Especially for unsupervised learning, machine learning can help us achieve signal clustering in cases where humans cannot categorize signals explicitly [228]. (2) Noise Reduction: Sensed signals always contain noise. Biosensors may have severe signal interference or noise. Therefore, machine models can be trained to distinguish between signal and noise [229]. (3) Anomaly detection: Biosensors are inevitably affected by the

sample matrix and operating conditions. When biosensors are used in the field, they may be severely disturbed by contamination. Computer-learned adaptivity not only detects the signal but also corrects for variations in sensor performance due to biological contamination and interference in the actual sample [230]. (4) Data Visualization and Interpretation: Computer vision techniques can help visualize and interpret data obtained from biosensors, making it easier for researchers and users to understand and draw conclusions from complex biological information [231]. In summary, computer vision can directly, automatically, accurately, and quickly help biosensors read out data, which is important for on-site inspection or diagnosis.

#### 6.2.2 Different biosensors powered by computer vision

Computer vision technology can directly, automatically, accurately, and rapidly assist in reading biosensors and processing acquired images to extract relevant information for analysis and diagnostics. This technology is commonly combined with microfluidics [232], lateral flow assay [233], and microscopy [234], etc., which significantly improves the accuracy and convenience of detection. Recently, our lab developed a disposable chip for SARS-CoV-2 detection using computer vision technique [65], which can improve the reliability and accuracy of naked-eye based detection; Zhao et al. integrated optical microscopy with a microfluidic platform for computer vision-based analysis [235], enabling simultaneous analysis of multiple biomarkers and antibiotics. Electrochemical biosensors are another widely used systems that generate data in the form of electrochemical signals whose spatial distribution can be captured by imaging techniques

and then analyzed using computer vision algorithms. A common problem with electrochemical biosensors for real sample detection is that the reproducibility and stability is relatively weak [236], [237]. Rong et al. developed an SVM (Support Vector machine) model to analyze the EIS (Electrochemical Impedance Spectroscopy) data without equivalent circuit fitting [238]. The SVM with radial base function kernel was demonstrated to have the optimal performance for classifying the training data set with an accuracy of 98%. Combining single molecule electrical biosensors with computer vision can improve the accuracy and precision of single molecular identification with applications in DNA sensing [86], RNA sequencing [239], and pathogen detection [72]. The overlapping of current signals in many electrochemical sensors cannot satisfy the detection and identification of multiple analytes. This challenge can be addressed by using computer vision to analyze the current temporal waveform [240]. Arima et al. introduce a nanopore platform integrated with machine learning for digital diagnosis of virus infection [241]. SPR (Surface Plasmon Resonance) and other spectra-based biosensors are also promising tool for the rapid and nondestructive detection [242]. Li et al. developed a chemically based SPR imaging technique for fingerprint surfaces that can facilitate subsequent computer vision for analysis or identification [243]. Computer vision can also simplify the detection process of point-of-care biosensors by providing rapid and on-site analysis of biological samples. For example, smartphone-based microscopy has become a promising POC device for the applications in diagnostics [244]. The images can be acquired, calculated, and analyzed in real time by a smartphone camera. Xu et al. developed a smartphone application named Tick Phone App, which can rapidly identify the ticks using this App [245]. There are also in vivo imaging biosensors using computer vision to visualize and

analyze biological processes inside living organisms. They often involve non-invasive imaging methods [246], such as fluorescence imaging [247], optical coherence tomography [248], or multimodal fusion approaches [249] to study tissues and organs in vivo [250]. Some biosensors employ computer vision to assess and monitor environmental conditions, such as water quality [251], air pollution [252], or soil health [253]. These biosensors can detect changes in biological indicators to assess the environmental impact.

### 6.2.3 Current challenges and future directions for computer vision in biosensors

The use of computer vision in biosensor applications has been increasingly compelling, but many challenges remain to realize its full potential [254]. Data availability is a major driver for computer vision applications and also a major obstacle. Machine learning requires large amounts of data, and the scarcity and lack of data pose a serious challenge, especially for biosensors and biomedical related data. In clinical practice, data from various modalities may not always be accessible for all samples, primarily due to cost constraints and limitations in data collection. Therefore, innovative methods must be developed to deal with different modalities of missing patterns. Fortunately, various interpolations [255], estimations [256], and matrix-completion algorithms [257], etc. have been successfully applied to optimize algorithms for practical applications.

Another challenge is data acquisition and analysis. Biological samples may have complex sample morphology, necessitating accurate recognition and segmentation, even when structures overlap is irregular [258]. The quality and quantity of data used to train and test

computer vision algorithms can greatly affect the performance of the algorithms [259]. It is critical to obtain annotated datasets that accurately represent the diversity and complexity of biosensor samples. In particular, analyzing single-molecule detection data is challenging and is largely limited by poor signal-to-noise ratio, signal overlap, and signal dispersion [260]. The development of new machine learning methods to reduce noise and extract multidimensional signal features can improve the resolution of pattern recognition and the sensitivity of objective identification [261].

Improving the performance of computing hardware has become a significant challenge and is currently a bottleneck in the field. Firstly, achieving effective biosensing through computer vision depends on the quality of hardware such as cameras and sensors. Higher-quality equipment is necessary to achieve high accuracy. Secondly, computer vision applications often demand substantial computational resources and necessitating enhancements in hardware performance, such as GPUs, TPUs [262], and the introduction of new chip architectures [263]. Faster storage devices and higher-speed network connections are also areas that require enhancement. Additionally, ongoing maintenance and updates contribute to the overall high cost. While computer vision algorithms require high-performance hardware, they also need to consider energy efficiency and cost reduction. Fortunately, with the advent of the new industrial era, there is more room to optimize these issues, such as the use of hardware accelerators and emerging computing paradigms like quantum computing [264], [265].

With the advent of the big data era, technological advances and the protection of privacy, security, and ethical principles have become paramount issues [266]. The proliferation of data-driven technologies, including computer vision, means that our personal information, once considered private, is increasingly likely to be exposed to the public. In the context of biosensor applications, computer vision may involve the analysis of large amounts of personal biological data [267]. This convergence of powerful technologies with private personal information highlights the urgent need to address the legal and ethical issues associated with data privacy and security. It is critical that strong security measures and strict access controls be put in place to protect this sensitive information from destruction, disclosure, or any form of exploitation. We hope and expect that the coming era of big data will continue to explore these trade-offs and find new ways to balance the various interests of humanity [268].

Addressing these challenges requires advanced computer vision techniques, data preprocessing, machine learning, and domain-specific knowledge. Researchers and engineers in the field will continue to develop innovative solutions for successfully integrating computer vision into biosensor applications to improve healthcare [269], diagnostics [270], and medical [271]. Over the past few years, algorithmic advances have ushered in a new era of capabilities and possibilities for computer vision. The development of novel models such as deep learning models [272], migration learning models [273], Generative Adversarial Networks (GANs) [274], semi-supervised and self-supervised learning techniques [275], etc., has played an important role in addressing data labeling challenges. With the rapid development of mobile terminals such as smartphones [276],

tablets [277], and wearables [278], future AI systems will indeed move towards miniaturization and portability. Miniature devices can perform many tasks locally without sending user data to the cloud for processing, helping to protect user privacy and sensitive information. The computing power of mobile terminals is increasing, making it possible to execute complex AI algorithms on small devices. As algorithms are carried out and enhanced, the ability to perform computer vision can be greatly improved.

Traditional biosensing methods offer major advantages such as portability, simplicity and low cost [279]. However, combining them with emerging technologies like computer vision further improves the overall performance and reliability of biosensing systems. The application of computer vision in biosensors holds great promise, yet it confronts some challenges that need attention. These challenges encompass enhancing computer hardware performance, optimizing sensor material performance, and refining biological applications. As research advances, data collection and sharing methods continually improve, and the cost and accessibility of disease surveillance technologies continue to decrease. Machine learning algorithms emerge as a promising avenue to further expedite progress in the field of biosensors. In the coming era of artificial intelligence, future biosensors may incorporate technologies such as artificial intelligence, the Internet of Things, big data sets, and cloud computing to build AI systems for themselves [280]. Leaving digital traces can unlock vast opportunities. The digital realm mirrors the physical world, enabling us to migrate experimental designs and entire industrial processes to the cloud, allowing for the virtual extrapolation of our world. This has the potential to usher in a new era of industrial revolution [281].

### **6.3 Summarizing and Understanding Virus Detection**

Virus detection is a crucial aspect of infectious disease control and public health management. It involves identifying the presence of viral pathogens in various samples, including bodily fluids, environmental samples, and surfaces. Traditional methods of virus detection include viral culture, antigen detection assays, and serological tests, which rely on the isolation and identification of viral particles, or the detection of antibodies produced by the host immune system in response to viral infection. However, these methods can be time-consuming, labor-intensive, and may lack sensitivity.

In recent years, molecular techniques such as polymerase chain reaction (PCR) and nucleic acid amplification tests (NAATs) have become the gold standard for virus detection due to their high sensitivity and specificity. These methods detect the genetic material (DNA or RNA) of the virus by amplifying specific regions of the viral genome, allowing for the rapid and accurate identification of viral pathogens. PCR-based assays are widely used in clinical diagnostics for detecting a variety of viruses, including influenza, HIV, hepatitis, and SARS-CoV-2, the virus responsible for COVID-19.

In addition to molecular techniques, advances in biosensing technologies have led to the development of rapid and portable virus detection devices. Biosensors typically employ biological recognition elements such as antibodies or nucleic acids immobilized on a transducer surface to selectively capture and detect viral particles. These biosensors can

offer real-time detection of viruses with high sensitivity and specificity, making them valuable tools for point-of-care testing and surveillance.

Furthermore, recent advancements in nanotechnology, microfluidics, and artificial intelligence have enabled the development of innovative virus detection platforms with enhanced performance characteristics. Nanomaterial-based sensors, for example, offer increased sensitivity and reduced detection limits, while microfluidic devices enable precise sample handling and automation. Machine learning algorithms can be employed to analyze complex datasets generated by these detection platforms, improving accuracy and reliability.

Overall, virus detection methods continue to evolve, driven by advancements in technology and a growing need for rapid, sensitive, and reliable diagnostic solutions. These innovations play a crucial role in controlling infectious disease outbreaks, guiding treatment decisions, and informing public health interventions.

## Bibliography

- [1] “Global Disease Detection Timeline.” Accessed: Oct. 25, 2021. [Online]. Available: <https://www.cdc.gov/globalhealth/infographics/global-health-security/global-disease-detection-timeline.html>
- [2] H. Yue, M. Huang, T. Tian, E. Xiong, and X. Zhou, “Advances in Clustered, Regularly Interspaced Short Palindromic Repeats (CRISPR)-Based Diagnostic Assays Assisted by Micro/Nanotechnologies,” *ACS Nano*, vol. 15, no. 5, pp. 7848–7859, May 2021, doi: 10.1021/acsnano.1c02372.
- [3] T. Tian *et al.*, “An Ultralocalized Cas13a Assay Enables Universal and Nucleic Acid Amplification-Free Single-Molecule RNA Diagnostics,” *ACS Nano*, vol. 15, no. 1, pp. 1167–1178, Jan. 2021, doi: 10.1021/acsnano.0c08165.
- [4] C. Yuan *et al.*, “Universal and Naked-Eye Gene Detection Platform Based on the Clustered Regularly Interspaced Short Palindromic Repeats/Cas12a/13a System,” *Anal. Chem.*, vol. 92, no. 5, pp. 4029–4037, Mar. 2020, doi: 10.1021/acs.analchem.9b05597.
- [5] P.-F. Liu, K.-R. Zhao, Z.-J. Liu, L. Wang, S.-Y. Ye, and G.-X. Liang, “Cas12a-based electrochemiluminescence biosensor for target amplification-free DNA detection,” *Biosens. Bioelectron.*, vol. 176, p. 112954, Mar. 2021, doi: 10.1016/j.bios.2020.112954.
- [6] R. Zhou, Y. Li, T. Dong, Y. Tang, and F. Li, “A sequence-specific plasmonic loop-mediated isothermal amplification assay with orthogonal color readouts enabled by CRISPR Cas12a,” *Chem. Commun.*, vol. 56, no. 24, pp. 3536–3538, 2020, doi: 10.1039/D0CC00397B.
- [7] J. Song *et al.*, “Two-Stage Isothermal Enzymatic Amplification for Concurrent Multiplex Molecular Detection,” *Clin. Chem.*, vol. 63, no. 3, pp. 714–722, Mar. 2017, doi: 10.1373/clinchem.2016.263665.
- [8] C. B. F. Vogels *et al.*, “Analytical sensitivity and efficiency comparisons of SARS-CoV-2 RT-qPCR primer–probe sets,” *Nat. Microbiol.*, vol. 5, no. 10, pp. 1299–1305, Oct. 2020, doi: 10.1038/s41564-020-0761-6.
- [9] R. Aman, A. Mahas, and M. Mahfouz, “Nucleic Acid Detection Using CRISPR/Cas Biosensing Technologies,” *ACS Synth. Biol.*, vol. 9, no. 6, pp. 1226–1233, Jun. 2020, doi: 10.1021/acssynbio.9b00507.
- [10] L. Liu *et al.*, “The Molecular Architecture for RNA-Guided RNA Cleavage by Cas13a,” *Cell*, vol. 170, no. 4, pp. 714–726.e10, Aug. 2017, doi: 10.1016/j.cell.2017.06.050.
- [11] M. Patchsung *et al.*, “Clinical validation of a Cas13-based assay for the detection of SARS-CoV-2 RNA,” *Nat. Biomed. Eng.*, vol. 4, no. 12, pp. 1140–1149, Dec. 2020, doi: 10.1038/s41551-020-00603-x.
- [12] P. Fozouni *et al.*, “Amplification-free detection of SARS-CoV-2 with CRISPR-Cas13a and mobile phone microscopy,” *Cell*, vol. 184, no. 2, pp. 323–333.e9, Jan. 2021, doi: 10.1016/j.cell.2020.12.001.
- [13] Q. A. Phan, L. B. Truong, D. Medina-Cruz, C. Dincer, and E. Mostafavi, “CRISPR/Cas-powered nanobiosensors for diagnostics,” *Biosens. Bioelectron.*, vol. 197, p. 113732, Feb. 2022, doi: 10.1016/j.bios.2021.113732.

- [14] N. Yadav, A. K. Chhillar, and J. S. Rana, “Detection of pathogenic bacteria with special emphasis to biosensors integrated with AuNPs,” *Sens. Int.*, vol. 1, p. 100028, Jan. 2020, doi: 10.1016/j.sintl.2020.100028.
- [15] V. Ramalingam, “Multifunctionality of gold nanoparticles: Plausible and convincing properties,” *Adv. Colloid Interface Sci.*, vol. 271, p. 101989, Sep. 2019, doi: 10.1016/j.cis.2019.101989.
- [16] J.-H. Choi, J. Lim, M. Shin, S.-H. Paek, and J.-W. Choi, “CRISPR-Cas12a-Based Nucleic Acid Amplification-Free DNA Biosensor via Au Nanoparticle-Assisted Metal-Enhanced Fluorescence and Colorimetric Analysis,” *Nano Lett.*, vol. 21, no. 1, pp. 693–699, Jan. 2021, doi: 10.1021/acs.nanolett.0c04303.
- [17] S. Liu *et al.*, “Highly Sensitive CRISPR/Cas12a-Based Fluorescence Detection of Porcine Reproductive and Respiratory Syndrome Virus,” *ACS Synth. Biol.*, vol. 10, no. 10, pp. 2499–2507, Oct. 2021, doi: 10.1021/acssynbio.1c00103.
- [18] M. Bao, E. Jensen, Y. Chang, G. Korensky, and K. Du, “Magnetic Bead-Quantum Dot (MB-Qdot) Clustered Regularly Interspaced Short Palindromic Repeat Assay for Simple Viral DNA Detection,” *ACS Appl. Mater. Interfaces*, vol. 12, no. 39, pp. 43435–43443, Sep. 2020, doi: 10.1021/acsami.0c12482.
- [19] K. Du *et al.*, “Microfluidic System for Detection of Viral RNA in Blood Using a Barcode Fluorescence Reporter and a Photocleavable Capture Probe,” *Anal. Chem.*, vol. 89, no. 22, pp. 12433–12440, Nov. 2017, doi: 10.1021/acs.analchem.7b03527.
- [20] P. Qin *et al.*, “Rapid and Fully Microfluidic Ebola Virus Detection with CRISPR-Cas13a,” *ACS Sens.*, vol. 4, no. 4, pp. 1048–1054, Apr. 2019, doi: 10.1021/acssensors.9b00239.
- [21] Q. He *et al.*, “High-throughput and all-solution phase African Swine Fever Virus (ASFV) detection using CRISPR-Cas12a and fluorescence based point-of-care system,” *Biosens. Bioelectron.*, vol. 154, p. 112068, Apr. 2020, doi: 10.1016/j.bios.2020.112068.
- [22] Y. Chang, M. Bao, J. Waitkus, H. Cai, and K. Du, “On-Demand Fully Enclosed Superhydrophobic–Optofluidic Devices Enabled by Microstereolithography,” *Langmuir*, vol. 38, no. 34, pp. 10672–10678, Aug. 2022, doi: 10.1021/acs.langmuir.2c01658.
- [23] X. Yong and K. Du, “Effects of Shape on Interaction Dynamics of Tetrahedral Nanoplastics and the Cell Membrane,” *J. Phys. Chem. B*, vol. 127, no. 7, pp. 1652–1663, Feb. 2023, doi: 10.1021/acs.jpcc.2c07460.
- [24] Y. Liu, K. Du, I. Wathuthanthri, and C.-H. Choi, “From nanocone to nanodisc: Structural transformation of gold nanoarrays via simple mechanical stresses,” *J. Vac. Sci. Technol. B*, vol. 30, no. 6, p. 06FF10, Nov. 2012, doi: 10.1116/1.4765635.
- [25] K. Du, Y. Liu, I. Wathuthanthri, and C.-H. Choi, “Fabrication of hierarchical nanostructures using free-standing trilayer membrane,” *J. Vac. Sci. Technol. B*, vol. 31, no. 6, p. 06FF04, Sep. 2013, doi: 10.1116/1.4821655.
- [26] K. Du, Y. Liu, I. Wathuthanthri, and C.-H. Choi, “Dual applications of free-standing holographic nanopatterns for lift-off and stencil lithography,” *J. Vac. Sci. Technol. B*, vol. 30, no. 6, p. 06FF04, Oct. 2012, doi: 10.1116/1.4757110.
- [27] C. ten Pas, K. Du, L. Pan, R.-Q. Wang, and S. Xu, “Understanding the dynamics of fluid–structure interaction with an Air Deflected Microfluidic Chip (ADMC),” *Sci. Rep.*, vol. 12, no. 1, p. 20399, Nov. 2022, doi: 10.1038/s41598-022-24112-w.

- [28] R. Peng, X. Chen, F. Xu, R. Hailstone, Y. Men, and K. Du, “Pneumatic nano-sieve for CRISPR-based detection of drug-resistant bacteria,” *Nanoscale Horiz.*, vol. 8, no. 12, pp. 1677–1685, 2023, doi: 10.1039/D3NH00365E.
- [29] K. Du *et al.*, “Multiplexed efficient on-chip sample preparation and sensitive amplification-free detection of Ebola virus,” *Biosens. Bioelectron.*, vol. 91, pp. 489–496, May 2017, doi: 10.1016/j.bios.2016.12.071.
- [30] K. N. Hass *et al.*, “Integrated Micropillar Polydimethylsiloxane Accurate CRISPR Detection System for Viral DNA Sensing,” *ACS Omega*, vol. 5, no. 42, pp. 27433–27441, Oct. 2020, doi: 10.1021/acsomega.0c03917.
- [31] H. Zhao *et al.*, “Ultrasensitive supersandwich-type electrochemical sensor for SARS-CoV-2 from the infected COVID-19 patients using a smartphone,” *Sens. Actuators B Chem.*, vol. 327, p. 128899, Jan. 2021, doi: 10.1016/j.snb.2020.128899.
- [32] A. Singh *et al.*, “Recent Advances in Electrochemical Biosensors: Applications, Challenges, and Future Scope,” *Biosensors*, vol. 11, no. 9, Art. no. 9, Sep. 2021, doi: 10.3390/bios11090336.
- [33] H. Karimi-Maleh, F. Karimi, M. Alizadeh, and A. L. Sanati, “Electrochemical Sensors, a Bright Future in the Fabrication of Portable Kits in Analytical Systems,” *Chem. Rec.*, vol. 20, no. 7, pp. 682–692, 2020, doi: 10.1002/tcr.201900092.
- [34] Z. Li, X. Ding, K. Yin, Z. Xu, K. Cooper, and C. Liu, “Electric field-enhanced electrochemical CRISPR biosensor for DNA detection,” *Biosens. Bioelectron.*, vol. 192, p. 113498, Nov. 2021, doi: 10.1016/j.bios.2021.113498.
- [35] A. M. Shrivastav, U. Cvelbar, and I. Abdulhalim, “A comprehensive review on plasmonic-based biosensors used in viral diagnostics,” *Commun. Biol.*, vol. 4, no. 1, Art. no. 1, Jan. 2021, doi: 10.1038/s42003-020-01615-8.
- [36] E. Mauriz, “Recent Progress in Plasmonic Biosensing Schemes for Virus Detection,” *Sensors*, vol. 20, no. 17, Art. no. 17, Jan. 2020, doi: 10.3390/s20174745.
- [37] K. M. Mayer and J. H. Hafner, “Localized Surface Plasmon Resonance Sensors,” *Chem. Rev.*, vol. 111, no. 6, pp. 3828–3857, Jun. 2011, doi: 10.1021/cr100313v.
- [38] A. J. Haes, S. Zou, J. Zhao, G. C. Schatz, and R. P. Van Duyne, “Localized Surface Plasmon Resonance Spectroscopy near Molecular Resonances,” *J. Am. Chem. Soc.*, vol. 128, no. 33, pp. 10905–10914, Aug. 2006, doi: 10.1021/ja063575q.
- [39] J. Waitkus *et al.*, “Gold Nanoparticle Enabled Localized Surface Plasmon Resonance on Unique Gold Nanomushroom Structures for On-Chip CRISPR-Cas13a Sensing,” *Adv. Mater. Interfaces*, vol. 10, no. 1, p. 2201261, 2023, doi: 10.1002/admi.202201261.
- [40] G. McNay, D. Eustace, W. E. Smith, K. Faulds, and D. Graham, “Surface-Enhanced Raman Scattering (SERS) and Surface-Enhanced Resonance Raman Scattering (SERRS): A Review of Applications,” *Appl. Spectrosc.*, vol. 65, no. 8, pp. 825–837, Aug. 2011, doi: 10.1366/11-06365.
- [41] X. Wang, W. Shi, G. She, and L. Mu, “Surface-Enhanced Raman Scattering (SERS) on transition metal and semiconductor nanostructures,” *Phys. Chem. Chem. Phys.*, vol. 14, no. 17, pp. 5891–5901, 2012, doi: 10.1039/C2CP40080D.
- [42] E. Ferrari, “Gold Nanoparticle-Based Plasmonic Biosensors,” *Biosensors*, vol. 13, no. 3, Art. no. 3, Mar. 2023, doi: 10.3390/bios13030411.

- [43] X. Yu *et al.*, “Plasmonic enhanced fluorescence spectroscopy using side-polished microstructured optical fiber,” *Sens. Actuators B Chem.*, vol. 160, no. 1, pp. 196–201, Dec. 2011, doi: 10.1016/j.snb.2011.07.033.
- [44] R. Layouni *et al.*, “High contrast cleavage detection for enhancing porous silicon sensor sensitivity,” *Opt. Express*, vol. 29, no. 1, pp. 1–11, Jan. 2021, doi: 10.1364/OE.412469.
- [45] K. Du, Y. Jiang, Y. Liu, I. Wathuthanthri, and C.-H. Choi, “Manipulation of the Superhydrophobicity of Plasma-Etched Polymer Nanostructures,” *Micromachines*, vol. 9, no. 6, Art. no. 6, Jun. 2018, doi: 10.3390/mi9060304.
- [46] Z. Li, L. Leustean, F. Inci, M. Zheng, U. Demirci, and S. Wang, “Plasmonic-based platforms for diagnosis of infectious diseases at the point-of-care,” *Biotechnol. Adv.*, vol. 37, no. 8, p. 107440, Dec. 2019, doi: 10.1016/j.biotechadv.2019.107440.
- [47] L. Liu, M. Dubrovsky, S. Gundavarapu, D. Vermeulen, and K. Du, “Viral nucleic acid detection with CRISPR-Cas12a using high contrast cleavage detection on micro-ring resonator biosensors,” in *Frontiers in Biological Detection: From Nanosensors to Systems XIII*, SPIE, Mar. 2021, pp. 8–13. doi: 10.1117/12.2580053.
- [48] P. T. Monis and S. Giglio, “Nucleic acid amplification-based techniques for pathogen detection and identification,” *Infect. Genet. Evol.*, vol. 6, no. 1, pp. 2–12, Jan. 2006, doi: 10.1016/j.meegid.2005.08.004.
- [49] H. Zhu, H. Zhang, Y. Xu, S. Laššáková, M. Korabečná, and P. Neuzil, “PCR past, present and future,” *BioTechniques*, vol. 69, no. 4, pp. 317–325, Oct. 2020, doi: 10.2144/btn-2020-0057.
- [50] M. Teymouri *et al.*, “Recent advances and challenges of RT-PCR tests for the diagnosis of COVID-19,” *Pathol. Res. Pract.*, vol. 221, p. 153443, May 2021, doi: 10.1016/j.prp.2021.153443.
- [51] X. Yuan *et al.*, “Current and Perspective Diagnostic Techniques for COVID-19,” *ACS Infect. Dis.*, vol. 6, no. 8, pp. 1998–2016, Aug. 2020, doi: 10.1021/acsinfecdis.0c00365.
- [52] P. B. van Kasteren *et al.*, “Comparison of seven commercial RT-PCR diagnostic kits for COVID-19,” *J. Clin. Virol.*, vol. 128, p. 104412, Jul. 2020, doi: 10.1016/j.jcv.2020.104412.
- [53] L. da Conceição Braga, B. Ô. P. Gonçalves, P. L. Coelho, A. L. da Silva Filho, and L. M. Silva, “Identification of best housekeeping genes for the normalization of RT-qPCR in human cell lines,” *Acta Histochem.*, vol. 124, no. 1, p. 151821, Jan. 2022, doi: 10.1016/j.acthis.2021.151821.
- [54] L. Jacky *et al.*, “Robust Multichannel Encoding for Highly Multiplexed Quantitative PCR,” *Anal. Chem.*, vol. 93, no. 9, pp. 4208–4216, Mar. 2021, doi: 10.1021/acs.analchem.0c04626.
- [55] K. Zhang *et al.*, “Hairpin Structure Facilitates Multiplex High-Fidelity DNA Amplification in Real-Time Polymerase Chain Reaction,” *Anal. Chem.*, vol. 94, no. 27, pp. 9586–9594, Jul. 2022, doi: 10.1021/acs.analchem.2c00575.
- [56] R. Aman, A. Mahas, T. Marsic, N. Hassan, and M. M. Mahfouz, “Efficient, Rapid, and Sensitive Detection of Plant RNA Viruses With One-Pot RT-RPA–CRISPR/Cas12a Assay,” *Front. Microbiol.*, vol. 11, 2020, Accessed: Aug. 04, 2022. [Online]. Available: <https://www.frontiersin.org/articles/10.3389/fmicb.2020.610872>

- [57] J. Fischbach, N. C. Xander, M. Frohme, and J. F. Glökler, “Shining a light on LAMP assays’ A comparison of LAMP visualization methods including the novel use of berberine,” *BioTechniques*, vol. 58, no. 4, pp. 189–194, Apr. 2015, doi: 10.2144/000114275.
- [58] C. Yao, R. Zhang, J. Tang, and D. Yang, “Rolling circle amplification (RCA)-based DNA hydrogel,” *Nat. Protoc.*, vol. 16, no. 12, pp. 5460–5483, Dec. 2021, doi: 10.1038/s41596-021-00621-2.
- [59] Y. Ju, H. Yong Kim, J. Ki Ahn, and H. Gyu Park, “Ultrasensitive version of nucleic acid sequence-based amplification (NASBA) utilizing a nicking and extension chain reaction system,” *Nanoscale*, vol. 13, no. 24, pp. 10785–10791, 2021, doi: 10.1039/D1NR00564B.
- [60] J. Glökler, T. S. Lim, J. Ida, and M. Frohme, “Isothermal amplifications – a comprehensive review on current methods,” *Crit. Rev. Biochem. Mol. Biol.*, vol. 56, no. 6, pp. 543–586, Nov. 2021, doi: 10.1080/10409238.2021.1937927.
- [61] T. J. Moehling, G. Choi, L. C. Dugan, M. Salit, and R. J. Meagher, “LAMP Diagnostics at the Point-of-Care: Emerging Trends and Perspectives for the Developer Community,” *Expert Rev. Mol. Diagn.*, vol. 21, no. 1, pp. 43–61, Jan. 2021, doi: 10.1080/14737159.2021.1873769.
- [62] M. Tan, C. Liao, L. Liang, X. Yi, Z. Zhou, and G. Wei, “Recent advances in recombinase polymerase amplification: Principle, advantages, disadvantages and applications,” *Front. Cell. Infect. Microbiol.*, vol. 12, Nov. 2022, doi: 10.3389/fcimb.2022.1019071.
- [63] D. Liu *et al.*, “A microfluidic-integrated lateral flow recombinase polymerase amplification (MI-IF-RPA) assay for rapid COVID-19 detection,” *Lab. Chip*, vol. 21, no. 10, pp. 2019–2026, May 2021, doi: 10.1039/D0LC01222J.
- [64] S. Tomar, B. Lavickova, and C. Guiducci, “Recombinase polymerase amplification in minimally buffered conditions,” *Biosens. Bioelectron.*, vol. 198, p. 113802, Feb. 2022, doi: 10.1016/j.bios.2021.113802.
- [65] M. Bao *et al.*, “Computer vision enabled funnel adapted sensing tube (FAST) for power-free and pipette-free nucleic acid detection,” *Lab. Chip*, vol. 22, no. 24, pp. 4849–4859, 2022, doi: 10.1039/D2LC00586G.
- [66] Q. Chen *et al.*, “CRISPR–Cas12-based field-deployable system for rapid detection of synthetic DNA sequence of the monkeypox virus genome,” *J. Med. Virol.*, vol. 95, no. 1, p. e28385, 2023, doi: 10.1002/jmv.28385.
- [67] W. Shi, A. K. Friedman, and L. A. Baker, “Nanopore Sensing,” *Anal. Chem.*, vol. 89, no. 1, pp. 157–188, Jan. 2017, doi: 10.1021/acs.analchem.6b04260.
- [68] Y. Wu and J. Justin Gooding, “The application of single molecule nanopore sensing for quantitative analysis,” *Chem. Soc. Rev.*, vol. 51, no. 10, pp. 3862–3885, 2022, doi: 10.1039/D1CS00988E.
- [69] L. Xue, H. Yamazaki, R. Ren, M. Wanunu, A. P. Ivanov, and J. B. Edel, “Solid-state nanopore sensors,” *Nat. Rev. Mater.*, vol. 5, no. 12, pp. 931–951, Dec. 2020, doi: 10.1038/s41578-020-0229-6.
- [70] B. N. Miles, A. P. Ivanov, K. A. Wilson, F. Doğan, D. Japrun, and J. B. Edel, “Single molecule sensing with solid-state nanopores: novel materials, methods, and applications,” *Chem. Soc. Rev.*, vol. 42, no. 1, pp. 15–28, 2013, doi: 10.1039/C2CS35286A.

- [71] M. Wanunu and A. Meller, “Chemically Modified Solid-State Nanopores,” *Nano Lett.*, vol. 7, no. 6, pp. 1580–1585, Jun. 2007, doi: 10.1021/nl070462b.
- [72] L. Liu *et al.*, “Gold Nanoparticle-Labeled CRISPR-Cas13a Assay for the Sensitive Solid-State Nanopore Molecular Counting,” *Adv. Mater. Technol.*, vol. 7, no. 3, p. 2101550, 2022, doi: 10.1002/admt.202101550.
- [73] S.-W. Nam, M. J. Rooks, K.-B. Kim, and S. M. Rossnagel, “Ionic Field Effect Transistors with Sub-10 nm Multiple Nanopores,” *Nano Lett.*, vol. 9, no. 5, pp. 2044–2048, May 2009, doi: 10.1021/nl900309s.
- [74] Y. Zhao, M. Iarossi, A. F. De Fazio, J.-A. Huang, and F. De Angelis, “Label-Free Optical Analysis of Biomolecules in Solid-State Nanopores: Toward Single-Molecule Protein Sequencing,” *ACS Photonics*, vol. 9, no. 3, pp. 730–742, Mar. 2022, doi: 10.1021/acsp Photonics.1c01825.
- [75] Y. Goto, R. Akahori, I. Yanagi, and K. Takeda, “Solid-state nanopores towards single-molecule DNA sequencing,” *J. Hum. Genet.*, vol. 65, no. 1, pp. 69–77, Jan. 2020, doi: 10.1038/s10038-019-0655-8.
- [76] J. Li, D. Fologea, R. Rollings, and B. Ledden, “Characterization of Protein Unfolding with Solid-state Nanopores,” *Protein Pept. Lett.*, vol. 21, no. 3, pp. 256–265, Mar. 2014.
- [77] D.-K. Kwak *et al.*, “Probing the Small-Molecule Inhibition of an Anticancer Therapeutic Protein-Protein Interaction Using a Solid-State Nanopore,” *Angew. Chem. Int. Ed.*, vol. 55, no. 19, pp. 5713–5717, 2016, doi: 10.1002/anie.201511601.
- [78] L. He, P. Karau, and V. Tabard-Cossa, “Fast capture and multiplexed detection of short multi-arm DNA stars in solid-state nanopores,” *Nanoscale*, vol. 11, no. 35, pp. 16342–16350, 2019, doi: 10.1039/C9NR04566J.
- [79] A. Arima *et al.*, “Selective detections of single-viruses using solid-state nanopores,” *Sci. Rep.*, vol. 8, no. 1, p. 16305, Nov. 2018, doi: 10.1038/s41598-018-34665-4.
- [80] Y. Wang, Y. Zhao, A. Bollas, Y. Wang, and K. F. Au, “Nanopore sequencing technology, bioinformatics and applications,” *Nat. Biotechnol.*, vol. 39, no. 11, Art. no. 11, Nov. 2021, doi: 10.1038/s41587-021-01108-x.
- [81] J. Kudr *et al.*, “Fabrication of solid-state nanopores and its perspectives,” *ELECTROPHORESIS*, vol. 36, no. 19, pp. 2367–2379, 2015, doi: 10.1002/elps.201400612.
- [82] “Nanopore Products.” Accessed: Oct. 18, 2021. [Online]. Available: <https://www.norcada.com/products/nanopore-products/>
- [83] E. C. Yusko *et al.*, “Real-time shape approximation and fingerprinting of single proteins using a nanopore,” *Nat. Nanotechnol.*, vol. 12, no. 4, pp. 360–367, Apr. 2017, doi: 10.1038/nnano.2016.267.
- [84] J. Larkin, R. Y. Henley, V. Jadhav, J. Korlach, and M. Wanunu, “Length-independent DNA packing into nanopore zero-mode waveguides for low-input DNA sequencing,” *Nat. Nanotechnol.*, vol. 12, no. 12, pp. 1169–1175, Dec. 2017, doi: 10.1038/nnano.2017.176.
- [85] Y. Luo, L. Wu, J. Tu, and Z. Lu, “Application of Solid-State Nanopore in Protein Detection,” *Int. J. Mol. Sci.*, vol. 21, no. 8, Art. no. 8, Jan. 2020, doi: 10.3390/ijms21082808.
- [86] M. Volarić, D. Veseljak, B. Mravinac, N. Meštrović, and E. Despot-Slade, “Isolation of High Molecular Weight DNA from the Model Beetle *Tribolium* for

- Nanopore Sequencing,” *Genes*, vol. 12, no. 8, Art. no. 8, Aug. 2021, doi: 10.3390/genes12081114.
- [87] L. Cao *et al.*, “On the Origin of Ion Selectivity in Ultrathin Nanopores: Insights for Membrane-Scale Osmotic Energy Conversion,” *Adv. Funct. Mater.*, vol. 28, no. 39, p. 1804189, 2018, doi: 10.1002/adfm.201804189.
- [88] S. W. Kowalczyk, A. R. Hall, and C. Dekker, “Detection of Local Protein Structures along DNA Using Solid-State Nanopores,” *Nano Lett.*, vol. 10, no. 1, pp. 324–328, Jan. 2010, doi: 10.1021/nl903631m.
- [89] R. Nouri, Y. Jiang, X. L. Lian, and W. Guan, “Sequence-Specific Recognition of HIV-1 DNA with Solid-State CRISPR-Cas12a-Assisted Nanopores (SCAN),” *ACS Sens.*, vol. 5, no. 5, pp. 1273–1280, May 2020, doi: 10.1021/acssensors.0c00497.
- [90] N. E. Weckman *et al.*, “Multiplexed DNA Identification Using Site Specific dCas9 Barcodes and Nanopore Sensing,” *ACS Sens.*, vol. 4, no. 8, pp. 2065–2072, Aug. 2019, doi: 10.1021/acssensors.9b00686.
- [91] N. R. Yun, C.-M. Kim, D. Y. Kim, J.-W. Seo, and D.-M. Kim, “Clinical usefulness of 16S ribosomal RNA real-time PCR for the diagnosis of scrub typhus,” *Sci. Rep.*, vol. 11, no. 1, p. 14299, Jul. 2021, doi: 10.1038/s41598-021-93541-w.
- [92] Y. Tang *et al.*, “Performance analysis of solid-state nanopore chemical sensor,” *Sens. Actuators B Chem.*, vol. 286, pp. 315–320, May 2019, doi: 10.1016/j.snb.2019.01.129.
- [93] F. Palaz *et al.*, “CRISPR-Cas13 System as a Promising and Versatile Tool for Cancer Diagnosis, Therapy, and Research,” *ACS Synth. Biol.*, vol. 10, no. 6, pp. 1245–1267, Jun. 2021, doi: 10.1021/acssynbio.1c00107.
- [94] F. Antaw, W. Anderson, A. Wuethrich, and M. Trau, “On the Behavior of Nanoparticles beyond the Nanopore Interface,” *Langmuir*, vol. 37, no. 16, pp. 4772–4782, Apr. 2021, doi: 10.1021/acs.langmuir.0c03083.
- [95] J. Wang, “Electrochemical detection for microscale analytical systems: a review,” *Talanta*, vol. 56, no. 2, pp. 223–231, Feb. 2002, doi: 10.1016/S0039-9140(01)00592-6.
- [96] E. Bakker and M. Telting-Diaz, “Electrochemical Sensors,” *Anal. Chem.*, vol. 74, no. 12, pp. 2781–2800, Jun. 2002, doi: 10.1021/ac0202278.
- [97] A. J. Blasco, M. C. González, and A. Escarpa, “Electrochemical approach for discriminating and measuring predominant flavonoids and phenolic acids using differential pulse voltammetry: towards an electrochemical index of natural antioxidants,” *Anal. Chim. Acta*, vol. 511, no. 1, pp. 71–81, May 2004, doi: 10.1016/j.aca.2004.01.038.
- [98] G. Davis, “Electrochemical techniques for the development of amperometric biosensors,” *Biosensors*, vol. 1, no. 2, pp. 161–178, Jan. 1985, doi: 10.1016/0265-928X(85)80002-X.
- [99] J.-C. Liu, H. Xiao, and J. Li, “Constructing High-Loading Single-Atom/Cluster Catalysts via an Electrochemical Potential Window Strategy,” *J. Am. Chem. Soc.*, vol. 142, no. 7, pp. 3375–3383, Feb. 2020, doi: 10.1021/jacs.9b06808.
- [100] B. J. Privett, J. H. Shin, and M. H. Schoenfish, “Electrochemical Sensors,” *Anal. Chem.*, vol. 82, no. 12, pp. 4723–4741, Jun. 2010, doi: 10.1021/ac101075n.

- [101] G. Hanrahan, D. G. Patil, and J. Wang, "Electrochemical sensors for environmental monitoring: design, development and applications," *J. Environ. Monit.*, vol. 6, no. 8, pp. 657–664, 2004, doi: 10.1039/B403975K.
- [102] J. A. Buledi, Z.-H. Shah, A. Mallah, and A. R. Solangi, "Current Perspective and Developments in Electrochemical Sensors Modified with Nanomaterials for Environmental and Pharmaceutical Analysis," *Curr. Anal. Chem.*, vol. 18, no. 1, pp. 102–115, Jan. 2022, doi: 10.2174/1573411016999201006122740.
- [103] O. Simoska and K. J. Stevenson, "Electrochemical sensors for rapid diagnosis of pathogens in real time," *Analyst*, vol. 144, no. 22, pp. 6461–6478, 2019, doi: 10.1039/C9AN01747J.
- [104] Y. Gu *et al.*, "Recent advances in nanomaterial-assisted electrochemical sensors for food safety analysis," *Food Front.*, vol. 3, no. 3, pp. 453–479, 2022, doi: 10.1002/fft2.143.
- [105] C. Zhu, G. Yang, H. Li, D. Du, and Y. Lin, "Electrochemical Sensors and Biosensors Based on Nanomaterials and Nanostructures," *Anal. Chem.*, vol. 87, no. 1, pp. 230–249, Jan. 2015, doi: 10.1021/ac5039863.
- [106] W. Zhang, R. Wang, F. Luo, P. Wang, and Z. Lin, "Miniaturized electrochemical sensors and their point-of-care applications," *Chin. Chem. Lett.*, vol. 31, no. 3, pp. 589–600, Mar. 2020, doi: 10.1016/j.ccllet.2019.09.022.
- [107] N. Nesakumar, S. Kesavan, C.-Z. Li, and S. Alwarappan, "Microfluidic Electrochemical Devices for Biosensing," *J. Anal. Test.*, vol. 3, no. 1, pp. 3–18, Jan. 2019, doi: 10.1007/s41664-019-0083-y.
- [108] A. Sanati *et al.*, "A review on recent advancements in electrochemical biosensing using carbonaceous nanomaterials," *Microchim. Acta*, vol. 186, no. 12, p. 773, Nov. 2019, doi: 10.1007/s00604-019-3854-2.
- [109] T. Zhou, R. Huang, M. Huang, J. Shen, Y. Shan, and D. Xing, "CRISPR/Cas13a Powered Portable Electrochemiluminescence Chip for Ultrasensitive and Specific MiRNA Detection," *Adv. Sci.*, vol. 7, no. 13, p. 1903661, 2020, doi: 10.1002/advs.201903661.
- [110] R. Bruch *et al.*, "CRISPR/Cas13a-Powered Electrochemical Microfluidic Biosensor for Nucleic Acid Amplification-Free miRNA Diagnostics," *Adv. Mater.*, vol. 31, no. 51, p. 1905311, 2019, doi: 10.1002/adma.201905311.
- [111] M. Zamani, J. M. Robson, A. Fan, M. S. Bono, A. L. Furst, and C. M. Klapperich, "Electrochemical Strategy for Low-Cost Viral Detection," *ACS Cent. Sci.*, vol. 7, no. 6, pp. 963–972, Jun. 2021, doi: 10.1021/acscentsci.1c00186.
- [112] C. Cao, J. B. Andrews, and A. D. Franklin, "Completely Printed, Flexible, Stable, and Hysteresis-Free Carbon Nanotube Thin-Film Transistors via Aerosol Jet Printing," *Adv. Electron. Mater.*, vol. 3, no. 5, p. 1700057, 2017, doi: 10.1002/aelm.201700057.
- [113] R. M. Cardoso *et al.*, "Additive-manufactured (3D-printed) electrochemical sensors: A critical review," *Anal. Chim. Acta*, vol. 1118, pp. 73–91, Jun. 2020, doi: 10.1016/j.aca.2020.03.028.
- [114] A. A. Gupta, A. Bolduc, S. G. Cloutier, and R. Izquierdo, "Aerosol Jet Printing for printed electronics rapid prototyping," in *2016 IEEE International Symposium on Circuits and Systems (ISCAS)*, May 2016, pp. 866–869. doi: 10.1109/ISCAS.2016.7527378.

- [115] S. Agarwala *et al.*, “Wearable Bandage-Based Strain Sensor for Home Healthcare: Combining 3D Aerosol Jet Printing and Laser Sintering,” *ACS Sens.*, vol. 4, no. 1, pp. 218–226, Jan. 2019, doi: 10.1021/acssensors.8b01293.
- [116] L. J. Deiner and T. L. Reitz, “Inkjet and Aerosol Jet Printing of Electrochemical Devices for Energy Conversion and Storage,” *Adv. Eng. Mater.*, vol. 19, no. 7, p. 1600878, 2017, doi: 10.1002/adem.201600878.
- [117] L. Liu *et al.*, “Aerosol Jet Printing-Enabled Dual-Function Electrochemical and Colorimetric Biosensor for SARS-CoV-2 Detection,” *Anal. Chem.*, vol. 95, no. 32, pp. 11997–12005, Aug. 2023, doi: 10.1021/acs.analchem.3c01724.
- [118] P. Fanjul-Bolado, M. B. González-García, and A. Costa-García, “Amperometric detection in TMB/HRP-based assays,” *Anal. Bioanal. Chem.*, vol. 382, no. 2, pp. 297–302, May 2005, doi: 10.1007/s00216-005-3084-9.
- [119] H. Teymourian *et al.*, “Wearable Electrochemical Sensors for the Monitoring and Screening of Drugs,” *ACS Sens.*, vol. 5, no. 9, pp. 2679–2700, Sep. 2020, doi: 10.1021/acssensors.0c01318.
- [120] R. Umapathi, S. M. Ghoreishian, S. Sonwal, G. M. Rani, and Y. S. Huh, “Portable electrochemical sensing methodologies for on-site detection of pesticide residues in fruits and vegetables,” *Coord. Chem. Rev.*, vol. 453, p. 214305, Feb. 2022, doi: 10.1016/j.ccr.2021.214305.
- [121] S. H. Baek *et al.*, “Development of a rapid and sensitive electrochemical biosensor for detection of human norovirus via novel specific binding peptides,” *Biosens. Bioelectron.*, vol. 123, pp. 223–229, Jan. 2019, doi: 10.1016/j.bios.2018.08.064.
- [122] “Rapid and ultrasensitive electromechanical detection of ions, biomolecules and SARS-CoV-2 RNA in unamplified samples | Nature Biomedical Engineering.” Accessed: Dec. 20, 2022. [Online]. Available: <https://www.nature.com/articles/s41551-021-00833-7>
- [123] R. Bruch *et al.*, “CRISPR-powered electrochemical microfluidic multiplexed biosensor for target amplification-free miRNA diagnostics,” *Biosens. Bioelectron.*, vol. 177, p. 112887, Apr. 2021, doi: 10.1016/j.bios.2020.112887.
- [124] A. East-Seletsky *et al.*, “Two distinct RNase activities of CRISPR-C2c2 enable guide-RNA processing and RNA detection,” *Nature*, vol. 538, no. 7624, pp. 270–273, Oct. 2016, doi: 10.1038/nature19802.
- [125] A. M. Weidling, V. S. Turkani, B. Luo, K. A. Schroder, and S. L. Swisher, “Photonic Curing of Solution-Processed Oxide Semiconductors with Efficient Gate Absorbers and Minimal Substrate Heating for High-Performance Thin-Film Transistors,” *ACS Omega*, vol. 6, no. 27, pp. 17323–17334, Jul. 2021, doi: 10.1021/acsomega.1c01421.
- [126] S. M. Pinto *et al.*, “Electrode cleaning and reproducibility of electrical impedance measurements of HeLa cells on aqueous solution,” *Rev. Acad. Colomb. Cienc. Exactas Físicas Nat.*, vol. 44, no. 170, pp. 257–268, Mar. 2020, doi: 10.18257/raccefyn.919.
- [127] A. M. Committee, “Recommendations for the definition, estimation and use of the detection limit,” *Analyst*, vol. 112, no. 2, pp. 199–204, 1987, doi: 10.1039/AN9871200199.

- [128] M. M. Kaminski, O. O. Abudayyeh, J. S. Gootenberg, F. Zhang, and J. J. Collins, “CRISPR-based diagnostics,” *Nat. Biomed. Eng.*, vol. 5, no. 7, Art. no. 7, Jul. 2021, doi: 10.1038/s41551-021-00760-7.
- [129] S. Doblinger, T. J. Donati, and D. S. Silvester, “Effect of Humidity and Impurities on the Electrochemical Window of Ionic Liquids and Its Implications for Electroanalysis,” *J. Phys. Chem. C*, vol. 124, no. 37, pp. 20309–20319, Sep. 2020, doi: 10.1021/acs.jpcc.0c07012.
- [130] S. S. Chandrasekaran *et al.*, “Rapid detection of SARS-CoV-2 RNA in saliva via Cas13,” *Nat. Biomed. Eng.*, vol. 6, no. 8, Art. no. 8, Aug. 2022, doi: 10.1038/s41551-022-00917-y.
- [131] Y. M. Shanbhag, M. M. Shanbhag, S. J. Malode, S. Dhanalakshmi, K. Mondal, and N. P. Shetti, “Direct and Sensitive Electrochemical Evaluation of Pramipexole Using Graphitic Carbon Nitride (gCN) Sensor,” *Biosensors*, vol. 12, no. 8, Art. no. 8, Aug. 2022, doi: 10.3390/bios12080552.
- [132] A. Raziq, A. Kidakova, R. Boroznjak, J. Reut, A. Öpik, and V. Syritski, “Development of a portable MIP-based electrochemical sensor for detection of SARS-CoV-2 antigen,” *Biosens. Bioelectron.*, vol. 178, p. 113029, Apr. 2021, doi: 10.1016/j.bios.2021.113029.
- [133] P. Qin *et al.*, “Rapid and Fully Microfluidic Ebola Virus Detection with CRISPR-Cas13a,” *ACS Sens.*, vol. 4, no. 4, pp. 1048–1054, Apr. 2019, doi: 10.1021/acssensors.9b00239.
- [134] T. Chaibun *et al.*, “Rapid electrochemical detection of coronavirus SARS-CoV-2,” *Nat. Commun.*, vol. 12, no. 1, Art. no. 1, Feb. 2021, doi: 10.1038/s41467-021-21121-7.
- [135] S. Gong, S. Zhang, F. Lu, W. Pan, N. Li, and B. Tang, “CRISPR/Cas-Based In Vitro Diagnostic Platforms for Cancer Biomarker Detection,” *Anal. Chem.*, vol. 93, no. 35, pp. 11899–11909, Sep. 2021, doi: 10.1021/acs.analchem.1c02533.
- [136] S. Lu *et al.*, “Flexible, Print-in-Place 1D–2D Thin-Film Transistors Using Aerosol Jet Printing,” *ACS Nano*, vol. 13, no. 10, pp. 11263–11272, Oct. 2019, doi: 10.1021/acsnano.9b04337.
- [137] C. Fisher, L. N. Skolrood, K. Li, P. C. Joshi, and T. Aytug, “Aerosol-Jet Printed Sensors for Environmental, Safety, and Health Monitoring: A Review,” *Adv. Mater. Technol.*, vol. n/a, no. n/a, p. 2300030, doi: 10.1002/admt.202300030.
- [138] S. Lei, S. Chen, and Q. Zhong, “Digital PCR for accurate quantification of pathogens: Principles, applications, challenges and future prospects,” *Int. J. Biol. Macromol.*, vol. 184, pp. 750–759, Aug. 2021, doi: 10.1016/j.ijbiomac.2021.06.132.
- [139] Z. Wei *et al.*, “Isothermal nucleic acid amplification technology for rapid detection of virus,” *Crit. Rev. Biotechnol.*, vol. 43, no. 3, pp. 415–432, Apr. 2023, doi: 10.1080/07388551.2022.2030295.
- [140] M. A. Munawar, “Critical insight into recombinase polymerase amplification technology,” *Expert Rev. Mol. Diagn.*, vol. 22, no. 7, pp. 725–737, Jul. 2022, doi: 10.1080/14737159.2022.2109964.
- [141] F. Padzil *et al.*, “Loop-Mediated Isothermal Amplification (LAMP) as a Promising Point-of-Care Diagnostic Strategy in Avian Virus Research,” *Animals*, vol. 12, no. 1, Art. no. 1, Jan. 2022, doi: 10.3390/ani12010076.

- [142] M. Soroka, B. Wasowicz, and A. Rymaszewska, “Loop-Mediated Isothermal Amplification (LAMP): The Better Sibling of PCR?,” *Cells*, vol. 10, no. 8, Art. no. 8, Aug. 2021, doi: 10.3390/cells10081931.
- [143] M. Goto, E. Honda, A. Ogura, A. Nomoto, and K.-I. Hanaki, “Colorimetric detection of loop-mediated isothermal amplification reaction by using hydroxy naphthol blue,” *BioTechniques*, vol. 46, no. 3, pp. 167–172, Mar. 2009, doi: 10.2144/000113072.
- [144] K. K. Dixit *et al.*, “Validation of SYBR green I based closed tube loop mediated isothermal amplification (LAMP) assay and simplified direct-blood-lysis (DBL)-LAMP assay for diagnosis of visceral leishmaniasis (VL),” *PLoS Negl. Trop. Dis.*, vol. 12, no. 11, p. e0006922, Nov. 2018, doi: 10.1371/journal.pntd.0006922.
- [145] F. Sun *et al.*, “Smartphone-based multiplex 30-minute nucleic acid test of live virus from nasal swab extract,” *Lab. Chip*, vol. 20, no. 9, pp. 1621–1627, 2020, doi: 10.1039/D0LC00304B.
- [146] “Shining a light on LAMP assays’ A comparison of LAMP visualization methods including the novel use of berberine | BioTechniques.” Accessed: Jan. 24, 2024. [Online]. Available: <https://www.future-science.com/doi/full/10.2144/000114275>
- [147] L. J. Robertson, J. W. B. van der Giessen, M. B. Batz, M. Kojima, and S. Cahill, “Have foodborne parasites finally become a global concern?,” *Trends Parasitol.*, vol. 29, no. 3, pp. 101–103, Mar. 2013, doi: 10.1016/j.pt.2012.12.004.
- [148] S. D. Bennett, S. V. Sodha, T. L. Ayers, M. F. Lynch, L. H. Gould, and R. V. Tauxe, “Produce-associated foodborne disease outbreaks, USA, 1998–2013,” *Epidemiol. Infect.*, vol. 146, no. 11, pp. 1397–1406, Aug. 2018, doi: 10.1017/S0950268818001620.
- [149] S. Strubbia *et al.*, “Metagenomic to evaluate norovirus genomic diversity in oysters: Impact on hexamer selection and targeted capture-based enrichment,” *Int. J. Food Microbiol.*, vol. 323, p. 108588, Jun. 2020, doi: 10.1016/j.ijfoodmicro.2020.108588.
- [150] S. A. Bustin, “Quantification of mRNA using real-time reverse transcription PCR (RT-PCR): trends and problems,” *J. Mol. Endocrinol.*, vol. 29, no. 1, pp. 23–39, Aug. 2002, doi: 10.1677/jme.0.0290023.
- [151] P. A. Underwood, “Problems and pitfalls with measurement of antibody affinity using solid phase binding in the ELISA,” *J. Immunol. Methods*, vol. 164, no. 1, pp. 119–130, Aug. 1993, doi: 10.1016/0022-1759(93)90282-C.
- [152] F. Mi *et al.*, “Recent advancements in microfluidic chip biosensor detection of foodborne pathogenic bacteria: a review,” *Anal. Bioanal. Chem.*, vol. 414, no. 9, pp. 2883–2902, Apr. 2022, doi: 10.1007/s00216-021-03872-w.
- [153] Z. Li *et al.*, “Fully integrated microfluidic devices for qualitative, quantitative and digital nucleic acids testing at point of care,” *Biosens. Bioelectron.*, vol. 177, p. 112952, Apr. 2021, doi: 10.1016/j.bios.2020.112952.
- [154] B. K. Gale *et al.*, “A Review of Current Methods in Microfluidic Device Fabrication and Future Commercialization Prospects,” *Inventions*, vol. 3, no. 3, Art. no. 3, Sep. 2018, doi: 10.3390/inventions3030060.
- [155] A. C. G. Foddai and I. R. Grant, “Methods for detection of viable foodborne pathogens: current state-of-art and future prospects,” *Appl. Microbiol. Biotechnol.*, vol. 104, no. 10, pp. 4281–4288, May 2020, doi: 10.1007/s00253-020-10542-x.

- [156] X. Meng, Y. Yu, P. Gong, and G. Jin, “An integrated droplet digital PCR gene chip for absolute quantification of nucleic acid,” *Microfluid. Nanofluidics*, vol. 25, no. 7, p. 62, Jun. 2021, doi: 10.1007/s10404-021-02465-4.
- [157] S. Lignel, A.-V. Salsac, A. Drelich, E. Leclerc, and I. Pezron, “Water-in-oil droplet formation in a flow-focusing microsystem using pressure- and flow rate-driven pumps,” *Colloids Surf. Physicochem. Eng. Asp.*, vol. 531, pp. 164–172, Oct. 2017, doi: 10.1016/j.colsurfa.2017.07.065.
- [158] F. Shen, W. Du, J. E. Kreutz, A. Fok, and R. F. Ismagilov, “Digital PCR on a SlipChip,” *Lab. Chip*, vol. 10, no. 20, pp. 2666–2672, 2010, doi: 10.1039/C004521G.
- [159] N. Massad-Ivanir *et al.*, “Porous Silicon-Based Biosensors: Towards Real-Time Optical Detection of Target Bacteria in the Food Industry,” *Sci. Rep.*, vol. 6, no. 1, p. 38099, Nov. 2016, doi: 10.1038/srep38099.
- [160] K. Yi, Y. Wang, K. Shi, J. Chi, J. Lyu, and Y. Zhao, “Aptamer-decorated porous microneedles arrays for extraction and detection of skin interstitial fluid biomarkers,” *Biosens. Bioelectron.*, vol. 190, p. 113404, Oct. 2021, doi: 10.1016/j.bios.2021.113404.
- [161] J. Briones, W. Espulgar, S. Koyama, H. Takamatsu, E. Tamiya, and M. Saito, “A design and optimization of a high throughput valve based microfluidic device for single cell compartmentalization and analysis,” *Sci. Rep.*, vol. 11, no. 1, p. 12995, Jun. 2021, doi: 10.1038/s41598-021-92472-w.
- [162] M. A. Zaczek-Moczydlowska, A. Beizaei, M. Dillon, and K. Campbell, “Current state-of-the-art diagnostics for Norovirus detection: Model approaches for point-of-care analysis,” *Trends Food Sci. Technol.*, vol. 114, pp. 684–695, Aug. 2021, doi: 10.1016/j.tifs.2021.06.027.
- [163] L. A. Ford-Siltz, K. Tohma, and G. I. Parra, “Understanding the relationship between norovirus diversity and immunity,” *Gut Microbes*, vol. 13, no. 1, p. 1900994, Jan. 2021, doi: 10.1080/19490976.2021.1900994.
- [164] N. Jothikumar, J. A. Lowther, K. Henshilwood, D. N. Lees, V. R. Hill, and J. Vinjé, “Rapid and Sensitive Detection of Noroviruses by Using TaqMan-Based One-Step Reverse Transcription-PCR Assays and Application to Naturally Contaminated Shellfish Samples,” *Appl. Environ. Microbiol.*, vol. 71, no. 4, pp. 1870–1875, Apr. 2005, doi: 10.1128/AEM.71.4.1870-1875.2005.
- [165] C. S. Ball, Y. K. Light, C.-Y. Koh, S. S. Wheeler, L. L. Coffey, and R. J. Meagher, “Quenching of Unincorporated Amplification Signal Reporters in Reverse-Transcription Loop-Mediated Isothermal Amplification Enabling Bright, Single-Step, Closed-Tube, and Multiplexed Detection of RNA Viruses,” *Anal. Chem.*, vol. 88, no. 7, pp. 3562–3568, Apr. 2016, doi: 10.1021/acs.analchem.5b04054.
- [166] K. A. Curtis, D. L. Rudolph, and S. M. Owen, “Rapid detection of HIV-1 by reverse-transcription, loop-mediated isothermal amplification (RT-LAMP),” *J. Virol. Methods*, vol. 151, no. 2, pp. 264–270, Aug. 2008, doi: 10.1016/j.jviromet.2008.04.011.
- [167] B. Thornton and C. Basu, “Rapid and Simple Method of qPCR Primer Design,” in *PCR Primer Design*, C. Basu, Ed., New York, NY: Springer, 2015, pp. 173–179. doi: 10.1007/978-1-4939-2365-6\_13.

- [168] X. Wu *et al.*, “Digital CRISPR-based method for the rapid detection and absolute quantification of nucleic acids,” *Biomaterials*, vol. 274, p. 120876, Jul. 2021, doi: 10.1016/j.biomaterials.2021.120876.
- [169] E.-C. Yeh, C.-C. Fu, L. Hu, R. Thakur, J. Feng, and L. P. Lee, “Self-powered integrated microfluidic point-of-care low-cost enabling (SIMPLE) chip,” *Sci. Adv.*, vol. 3, no. 3, p. e1501645, Mar. 2017, doi: 10.1126/sciadv.1501645.
- [170] L. Niessen, J. Luo, C. Denschlag, and R. F. Vogel, “The application of loop-mediated isothermal amplification (LAMP) in food testing for bacterial pathogens and fungal contaminants,” *Food Microbiol.*, vol. 36, no. 2, pp. 191–206, Dec. 2013, doi: 10.1016/j.fm.2013.04.017.
- [171] B. R. Schudel, M. Tanyeri, A. Mukherjee, C. M. Schroeder, and P. J. A. Kenis, “Multiplexed detection of nucleic acids in a combinatorial screening chip,” *Lab. Chip*, vol. 11, no. 11, pp. 1916–1923, 2011, doi: 10.1039/C0LC00342E.
- [172] K. K. Ghosh *et al.*, “Miniaturized integration of a fluorescence microscope,” *Nat. Methods*, vol. 8, no. 10, pp. 871–878, Oct. 2011, doi: 10.1038/nmeth.1694.
- [173] L. Liu and K. Du, “A perspective on computer vision in biosensing,” *Biomicrofluidics*, vol. 18, no. 1, p. 011301, Jan. 2024, doi: 10.1063/5.0185732.
- [174] “Cervical cancer.” Accessed: Jan. 28, 2024. [Online]. Available: <https://www.who.int/health-topics/cervical-cancer>
- [175] “Human Papillomavirus (HPV).” Accessed: Jan. 24, 2024. [Online]. Available: <https://www.who.int/teams/health-product-policy-and-standards/standards-and-specifications/vaccine-standardization/human-papillomavirus>
- [176] M. Arbyn *et al.*, “2020 list of human papillomavirus assays suitable for primary cervical cancer screening,” *Clin. Microbiol. Infect. Off. Publ. Eur. Soc. Clin. Microbiol. Infect. Dis.*, vol. 27, no. 8, pp. 1083–1095, Aug. 2021, doi: 10.1016/j.cmi.2021.04.031.
- [177] M.-H. Mayrand *et al.*, “Human Papillomavirus DNA versus Papanicolaou Screening Tests for Cervical Cancer,” *N. Engl. J. Med.*, vol. 357, no. 16, pp. 1579–1588, Oct. 2007, doi: 10.1056/NEJMoa071430.
- [178] T. Notomi, Y. Mori, N. Tomita, and H. Kanda, “Loop-mediated isothermal amplification (LAMP): principle, features, and future prospects,” *J. Microbiol.*, vol. 53, no. 1, pp. 1–5, Jan. 2015, doi: 10.1007/s12275-015-4656-9.
- [179] I. M. Lobato and C. K. O’Sullivan, “Recombinase polymerase amplification: Basics, applications and recent advances,” *TrAC Trends Anal. Chem.*, vol. 98, pp. 19–35, Jan. 2018, doi: 10.1016/j.trac.2017.10.015.
- [180] R. Wang *et al.*, “Rolling Circular Amplification (RCA)-Assisted CRISPR/Cas9 Cleavage (RACE) for Highly Specific Detection of Multiple Extracellular Vesicle MicroRNAs,” *Anal. Chem.*, vol. 92, no. 2, pp. 2176–2185, Jan. 2020, doi: 10.1021/acs.analchem.9b04814.
- [181] B. Deiman, P. van Aarle, and P. Sillekens, “Characteristics and applications of nucleic acid sequence-based amplification (NASBA),” *Mol. Biotechnol.*, vol. 20, no. 2, pp. 163–179, Feb. 2002, doi: 10.1385/MB:20:2:163.
- [182] R. Asadi and H. Mollasalehi, “The mechanism and improvements to the isothermal amplification of nucleic acids, at a glance,” *Anal. Biochem.*, vol. 631, p. 114260, Oct. 2021, doi: 10.1016/j.ab.2021.114260.

- [183] M. Parida, S. Sannarangaiah, P. K. Dash, P. V. L. Rao, and K. Morita, “Loop mediated isothermal amplification (LAMP): a new generation of innovative gene amplification technique; perspectives in clinical diagnosis of infectious diseases,” *Rev. Med. Virol.*, vol. 18, no. 6, pp. 407–421, 2008, doi: 10.1002/rmv.593.
- [184] T. L. Quyen, T. A. Ngo, D. D. Bang, M. Madsen, and A. Wolff, “Classification of Multiple DNA Dyes Based on Inhibition Effects on Real-Time Loop-Mediated Isothermal Amplification (LAMP): Prospect for Point of Care Setting,” *Front. Microbiol.*, vol. 10, 2019, Accessed: Jan. 24, 2024. [Online]. Available: <https://www.frontiersin.org/articles/10.3389/fmicb.2019.02234>
- [185] W. Yin *et al.*, “Digital Recombinase Polymerase Amplification, Digital Loop-Mediated Isothermal Amplification, and Digital CRISPR-Cas Assisted Assay: Current Status, Challenges, and Perspectives,” *Small*, vol. 19, no. 49, p. 2303398, 2023, doi: 10.1002/smll.202303398.
- [186] B. Coelho *et al.*, “Digital Microfluidics for Nucleic Acid Amplification,” *Sensors*, vol. 17, no. 7, Art. no. 7, Jul. 2017, doi: 10.3390/s17071495.
- [187] Z. Yu, L. Xu, W. Lyu, and F. Shen, “Parallel multistep digital analysis SlipChip demonstrated with the quantification of nucleic acid by digital LAMP-CRISPR,” *Lab. Chip*, vol. 22, no. 16, pp. 2954–2961, 2022, doi: 10.1039/D2LC00284A.
- [188] F. X. Liu *et al.*, “Isothermal Background-Free Nucleic Acid Quantification by a One-Pot Cas13a Assay Using Droplet Microfluidics,” *Anal. Chem.*, vol. 94, no. 15, pp. 5883–5892, Apr. 2022, doi: 10.1021/acs.analchem.2c00067.
- [189] L. Liu, S. J. Dollery, G. J. Tobin, G. Lu, and K. Du, “Digital Nanofluidic Chip for Simple and Highly Quantitative Detection of HPV Target.” medRxiv, p. 2024.03.01.24303620, Mar. 02, 2024. doi: 10.1101/2024.03.01.24303620.
- [190] J. M. Wong Tzeling *et al.*, “One-step, multiplex, dual-function oligonucleotide of loop-mediated isothermal amplification assay for the detection of pathogenic *Burkholderia pseudomallei*,” *Anal. Chim. Acta*, vol. 1171, p. 338682, Aug. 2021, doi: 10.1016/j.aca.2021.338682.
- [191] K. Karthik *et al.*, “New closed tube loop mediated isothermal amplification assay for prevention of product cross-contamination,” *MethodsX*, vol. 1, pp. 137–143, Jan. 2014, doi: 10.1016/j.mex.2014.08.009.
- [192] W. E. Huang *et al.*, “RT-LAMP for rapid diagnosis of coronavirus SARS-CoV-2,” *Microb. Biotechnol.*, vol. 13, no. 4, pp. 950–961, 2020, doi: 10.1111/1751-7915.13586.
- [193] S.-Y. Teh, R. Lin, L.-H. Hung, and A. P. Lee, “Droplet microfluidics,” *Lab. Chip*, vol. 8, no. 2, pp. 198–220, 2008, doi: 10.1039/B715524G.
- [194] A. Bektaş, “A Multiplex, Fluorescent, and Isothermal Method for Detecting Genetically Modified Maize,” *Food Anal. Methods*, vol. 11, no. 3, pp. 686–692, Mar. 2018, doi: 10.1007/s12161-017-1041-9.
- [195] M. Bao *et al.*, “Micro- and nanosystems for the detection of hemorrhagic fever viruses,” *Lab. Chip*, vol. 23, no. 19, pp. 4173–4200, Sep. 2023, doi: 10.1039/D3LC00482A.
- [196] C. Rivet, H. Lee, A. Hirsch, S. Hamilton, and H. Lu, “Microfluidics for medical diagnostics and biosensors,” *Chem. Eng. Sci.*, vol. 66, no. 7, pp. 1490–1507, Apr. 2011, doi: 10.1016/j.ces.2010.08.015.

- [197] C. I. L. Justino, A. C. Duarte, and T. A. P. Rocha-Santos, “Recent Progress in Biosensors for Environmental Monitoring: A Review,” *Sensors*, vol. 17, no. 12, Art. no. 12, Dec. 2017, doi: 10.3390/s17122918.
- [198] J. Kirsch, C. Siltanen, Q. Zhou, A. Revzin, and A. Simonian, “Biosensor technology: recent advances in threat agent detection and medicine,” *Chem. Soc. Rev.*, vol. 42, no. 22, pp. 8733–8768, 2013, doi: 10.1039/C3CS60141B.
- [199] M. Ramesh, R. Janani, C. Deepa, and L. Rajeshkumar, “Nanotechnology-Enabled Biosensors: A Review of Fundamentals, Design Principles, Materials, and Applications,” *Biosensors*, vol. 13, no. 1, Art. no. 1, Jan. 2023, doi: 10.3390/bios13010040.
- [200] J. Hu, F. Liu, Y. Chen, G. Shangguan, and H. Ju, “Mass Spectrometric Biosensing: A Powerful Approach for Multiplexed Analysis of Clinical Biomolecules,” *ACS Sens.*, vol. 6, no. 10, pp. 3517–3535, Oct. 2021, doi: 10.1021/acssensors.1c01394.
- [201] J. Tu, R. M. Torrente-Rodríguez, M. Wang, and W. Gao, “The Era of Digital Health: A Review of Portable and Wearable Affinity Biosensors,” *Adv. Funct. Mater.*, vol. 30, no. 29, p. 1906713, 2020, doi: 10.1002/adfm.201906713.
- [202] H. Sun, W. Xie, J. Mo, Y. Huang, and H. Dong, “Deep learning with microfluidics for on-chip droplet generation, control, and analysis,” *Front. Bioeng. Biotechnol.*, vol. 11, 2023, Accessed: Jun. 30, 2023. [Online]. Available: <https://www.frontiersin.org/articles/10.3389/fbioe.2023.1208648>
- [203] S. Kumar, S. Tripathy, A. Jyoti, and S. G. Singh, “Recent advances in biosensors for diagnosis and detection of sepsis: A comprehensive review,” *Biosens. Bioelectron.*, vol. 124–125, pp. 205–215, Jan. 2019, doi: 10.1016/j.bios.2018.10.034.
- [204] P. Li, G.-H. Lee, S. Y. Kim, S. Y. Kwon, H.-R. Kim, and S. Park, “From Diagnosis to Treatment: Recent Advances in Patient-Friendly Biosensors and Implantable Devices,” *ACS Nano*, vol. 15, no. 2, pp. 1960–2004, Feb. 2021, doi: 10.1021/acsnano.0c06688.
- [205] A. Aasi, S. Ebrahimi Bajgani, and B. Panchapakesan, “A first-principles investigation on the adsorption of octanal and nonanal molecules with decorated monolayer WS<sub>2</sub> as promising gas sensing platform,” *AIP Adv.*, vol. 13, no. 2, p. 025157, Feb. 2023, doi: 10.1063/5.0139950.
- [206] A. Aasi, S. M. Aghaei, and B. Panchapakesan, “Noble metal (Pt or Pd)-decorated atomically thin MoS<sub>2</sub> as a promising material for sensing colorectal cancer biomarkers through exhaled breath,” *Int. J. Comput. Mater. Sci. Eng.*, vol. 13, no. 01, p. 2350014, Mar. 2024, doi: 10.1142/S2047684123500148.
- [207] T. Arakawa, D. V. Dao, and K. Mitsubayashi, “Biosensors and Chemical Sensors for Healthcare Monitoring: A Review,” *IEEJ Trans. Electr. Electron. Eng.*, vol. 17, no. 5, pp. 626–636, 2022, doi: 10.1002/tee.23580.
- [208] E. M. McConnell, J. Nguyen, and Y. Li, “Aptamer-Based Biosensors for Environmental Monitoring,” *Front. Chem.*, vol. 8, 2020, Accessed: Sep. 29, 2023. [Online]. Available: <https://www.frontiersin.org/articles/10.3389/fchem.2020.00434>
- [209] S. Kang, K. Zhao, D.-G. Yu, X. Zheng, and C. Huang, “Advances in Biosensing and Environmental Monitoring Based on Electrospun Nanofibers,” *Adv. Fiber Mater.*, vol. 4, no. 3, pp. 404–435, Jun. 2022, doi: 10.1007/s42765-021-00129-0.

- [210] H. Sohrabi *et al.*, “Recent advances in the highly sensitive determination of zearalenone residues in water and environmental resources with electrochemical biosensors,” *Environ. Res.*, vol. 204, p. 112082, Mar. 2022, doi: 10.1016/j.envres.2021.112082.
- [211] Z. Hua, T. Yu, D. Liu, and Y. Xianyu, “Recent advances in gold nanoparticles-based biosensors for food safety detection,” *Biosens. Bioelectron.*, vol. 179, p. 113076, May 2021, doi: 10.1016/j.bios.2021.113076.
- [212] Y. Ye, H. Guo, and X. Sun, “Recent progress on cell-based biosensors for analysis of food safety and quality control,” *Biosens. Bioelectron.*, vol. 126, pp. 389–404, Feb. 2019, doi: 10.1016/j.bios.2018.10.039.
- [213] J. He *et al.*, “Superhydrophobic Rotation-Chip for Computer-Vision Identification of Drug-Resistant Bacteria,” *ACS Appl. Mater. Interfaces*, vol. 15, no. 23, pp. 27732–27741, Jun. 2023, doi: 10.1021/acsami.3c05131.
- [214] S. Munir *et al.*, “Nanozymes for medical biotechnology and its potential applications in biosensing and nanotherapeutics,” *Biotechnol. Lett.*, vol. 42, no. 3, pp. 357–373, Mar. 2020, doi: 10.1007/s10529-020-02795-3.
- [215] A. Antonacci and V. Scognamiglio, “Biotechnological Advances in the Design of Algae-Based Biosensors,” *Trends Biotechnol.*, vol. 38, no. 3, pp. 334–347, Mar. 2020, doi: 10.1016/j.tibtech.2019.10.005.
- [216] E. Cesewski and B. N. Johnson, “Electrochemical biosensors for pathogen detection,” *Biosens. Bioelectron.*, vol. 159, p. 112214, Jul. 2020, doi: 10.1016/j.bios.2020.112214.
- [217] V. Naresh and N. Lee, “A Review on Biosensors and Recent Development of Nanostructured Materials-Enabled Biosensors,” *Sensors*, vol. 21, no. 4, Art. no. 4, Jan. 2021, doi: 10.3390/s21041109.
- [218] M. T. Yarak and Y. N. Tan, “Metal Nanoparticles-Enhanced Biosensors: Synthesis, Design and Applications in Fluorescence Enhancement and Surface-enhanced Raman Scattering,” *Chem. – Asian J.*, vol. 15, no. 20, pp. 3180–3208, 2020, doi: 10.1002/asia.202000847.
- [219] P. Malik, R. Gupta, V. Malik, and R. K. Ameta, “Emerging nanomaterials for improved biosensing,” *Meas. Sens.*, vol. 16, p. 100050, Aug. 2021, doi: 10.1016/j.measen.2021.100050.
- [220] L. He *et al.*, “Current signal amplification strategies in aptamer-based electrochemical biosensor: A review,” *Chin. Chem. Lett.*, vol. 32, no. 5, pp. 1593–1602, May 2021, doi: 10.1016/j.ccllet.2020.12.054.
- [221] F. Laghrib *et al.*, “Current progress on COVID-19 related to biosensing technologies: New opportunity for detection and monitoring of viruses,” *Microchem. J.*, vol. 160, p. 105606, Jan. 2021, doi: 10.1016/j.microc.2020.105606.
- [222] R. Antiochia, “Developments in biosensors for CoV detection and future trends,” *Biosens. Bioelectron.*, vol. 173, p. 112777, Feb. 2021, doi: 10.1016/j.bios.2020.112777.
- [223] R. Szeliski, *Computer Vision: Algorithms and Applications*. Springer Nature, 2022.
- [224] H. Raji, M. Tayyab, J. Sui, S. R. Mahmoodi, and M. Javanmard, “Biosensors and machine learning for enhanced detection, stratification, and classification of cells: a

- review,” *Biomed. Microdevices*, vol. 24, no. 3, p. 26, Aug. 2022, doi: 10.1007/s10544-022-00627-x.
- [225] F. Cui, Y. Yue, Y. Zhang, Z. Zhang, and H. S. Zhou, “Advancing Biosensors with Machine Learning,” *ACS Sens.*, vol. 5, no. 11, pp. 3346–3364, Nov. 2020, doi: 10.1021/acssensors.0c01424.
- [226] J. Deng, W. Dong, R. Socher, L.-J. Li, K. Li, and L. Fei-Fei, “ImageNet: A large-scale hierarchical image database,” in *2009 IEEE Conference on Computer Vision and Pattern Recognition*, Jun. 2009, pp. 248–255. doi: 10.1109/CVPR.2009.5206848.
- [227] T. C. Hollon *et al.*, “Near real-time intraoperative brain tumor diagnosis using stimulated Raman histology and deep neural networks,” *Nat. Med.*, vol. 26, no. 1, Art. no. 1, Jan. 2020, doi: 10.1038/s41591-019-0715-9.
- [228] Y. Zhang and L. Wu, “Classification of Fruits Using Computer Vision and a Multiclass Support Vector Machine,” *Sensors*, vol. 12, no. 9, Art. no. 9, Sep. 2012, doi: 10.3390/s120912489.
- [229] J. Guan, R. Lai, A. Xiong, Z. Liu, and L. Gu, “Fixed pattern noise reduction for infrared images based on cascade residual attention CNN,” *Neurocomputing*, vol. 377, pp. 301–313, Feb. 2020, doi: 10.1016/j.neucom.2019.10.054.
- [230] Y. Bao, Z. Tang, H. Li, and Y. Zhang, “Computer vision and deep learning-based data anomaly detection method for structural health monitoring,” *Struct. Health Monit.*, vol. 18, no. 2, pp. 401–421, Mar. 2019, doi: 10.1177/1475921718757405.
- [231] A. Chatzimparmpas, R. M. Martins, I. Jusufi, K. Kucher, F. Rossi, and A. Kerren, “The State of the Art in Enhancing Trust in Machine Learning Models with the Use of Visualizations,” *Comput. Graph. Forum*, vol. 39, no. 3, pp. 713–756, 2020, doi: 10.1111/cgf.14034.
- [232] S. Zhou, B. Chen, E. S. Fu, and H. Yan, “Computer vision meets microfluidics: a label-free method for high-throughput cell analysis,” *Microsyst. Nanoeng.*, vol. 9, no. 1, Art. no. 1, Sep. 2023, doi: 10.1038/s41378-023-00562-8.
- [233] N. Rafat, L. Brewer, N. Das, D. J. Trivedi, B. K. Kaszala, and A. Sarkar, “Inexpensive High-Throughput Multiplexed Biomarker Detection Using Enzymatic Metallization with Cellphone-Based Computer Vision,” *ACS Sens.*, vol. 8, no. 2, pp. 534–542, Feb. 2023, doi: 10.1021/acssensors.2c01429.
- [234] H. Ceylan Koydemir *et al.*, “Rapid imaging, detection and quantification of *Giardia lamblia* cysts using mobile-phone based fluorescent microscopy and machine learning,” *Lab. Chip*, vol. 15, no. 5, pp. 1284–1293, 2015, doi: 10.1039/C4LC01358A.
- [235] W. Zhao *et al.*, “Computer Vision-Based Artificial Intelligence-Mediated Encoding-Decoding for Multiplexed Microfluidic Digital Immunoassay,” *ACS Nano*, vol. 17, no. 14, pp. 13700–13714, Jul. 2023, doi: 10.1021/acsnano.3c02941.
- [236] I. S. Kucherenko, O. O. Soldatkin, S. V. Dzyadevych, and A. P. Soldatkin, “Electrochemical biosensors based on multienzyme systems: Main groups, advantages and limitations – A review,” *Anal. Chim. Acta*, vol. 1111, pp. 114–131, May 2020, doi: 10.1016/j.aca.2020.03.034.
- [237] C. A. Martínez-Huitle, M. A. Rodrigo, I. Sirés, and O. Scialdone, “A critical review on latest innovations and future challenges of electrochemical technology for

- the abatement of organics in water,” *Appl. Catal. B Environ.*, vol. 328, p. 122430, Jul. 2023, doi: 10.1016/j.apcatb.2023.122430.
- [238] Y. Rong *et al.*, “Post hoc support vector machine learning for impedimetric biosensors based on weak protein–ligand interactions,” *Analyst*, vol. 143, no. 9, pp. 2066–2075, 2018, doi: 10.1039/C8AN00065D.
- [239] M. Wanunu, T. Dadosh, V. Ray, J. Jin, L. McReynolds, and M. Drndić, “Rapid electronic detection of probe-specific microRNAs using thin nanopore sensors,” *Nat. Nanotechnol.*, vol. 5, no. 11, pp. 807–814, Nov. 2010, doi: 10.1038/nnano.2010.202.
- [240] T. Albrecht, G. Slabaugh, E. Alonso, and S. M. R. Al-Arif, “Deep learning for single-molecule science,” *Nanotechnology*, vol. 28, no. 42, p. 423001, Sep. 2017, doi: 10.1088/1361-6528/aa8334.
- [241] A. Arima, M. Tsutsui, T. Washio, Y. Baba, and T. Kawai, “Solid-State Nanopore Platform Integrated with Machine Learning for Digital Diagnosis of Virus Infection,” *Anal. Chem.*, vol. 93, no. 1, pp. 215–227, Jan. 2021, doi: 10.1021/acs.analchem.0c04353.
- [242] D. Harpaz, B. Koh, R. C. S. Seet, I. Abdulhalim, and A. I. Y. Tok, “Functionalized silicon dioxide self-referenced plasmonic chip as point-of-care biosensor for stroke biomarkers NT-proBNP and S100 $\beta$ ,” *Talanta*, vol. 212, p. 120792, May 2020, doi: 10.1016/j.talanta.2020.120792.
- [243] M. Li, J. Xu, Q. Zheng, C. Guo, and Y. Chen, “Chemical-Based Surface Plasmon Resonance Imaging of Fingerprints,” *Anal. Chem.*, vol. 94, no. 20, pp. 7238–7245, May 2022, doi: 10.1021/acs.analchem.2c00389.
- [244] D. Erickson *et al.*, “Smartphone technology can be transformative to the deployment of lab-on-chip diagnostics,” *Lab. Chip*, vol. 14, no. 17, pp. 3159–3164, Jul. 2014, doi: 10.1039/C4LC00142G.
- [245] Z. Xu *et al.*, “TickPhone App: A Smartphone Application for Rapid Tick Identification Using Deep Learning,” *Appl. Sci.*, vol. 11, no. 16, Art. no. 16, Jan. 2021, doi: 10.3390/app11167355.
- [246] K. Zhang, J. Wang, T. Liu, Y. Luo, X. J. Loh, and X. Chen, “Machine Learning-Reinforced Noninvasive Biosensors for Healthcare,” *Adv. Healthc. Mater.*, vol. 10, no. 17, p. 2100734, Sep. 2021, doi: 10.1002/adhm.202100734.
- [247] A. V. Leopold, D. M. Shcherbakova, and V. V. Verkhusha, “Fluorescent Biosensors for Neurotransmission and Neuromodulation: Engineering and Applications,” *Front. Cell. Neurosci.*, vol. 13, 2019, Accessed: Oct. 03, 2023. [Online]. Available: <https://www.frontiersin.org/articles/10.3389/fncel.2019.00474>
- [248] Y. Zeng, W. C. Chapman Jr, Y. Lin, S. Li, M. Mutch, and Q. Zhu, “Diagnosing colorectal abnormalities using scattering coefficient maps acquired from optical coherence tomography,” *J. Biophotonics*, vol. 14, no. 1, p. e202000276, 2021, doi: 10.1002/jbio.202000276.
- [249] L. R. Soenksen *et al.*, “Integrated multimodal artificial intelligence framework for healthcare applications,” *Npj Digit. Med.*, vol. 5, no. 1, Art. no. 1, Sep. 2022, doi: 10.1038/s41746-022-00689-4.
- [250] J. Banerjee, J. N. Taroni, R. J. Allaway, D. V. Prasad, J. Guinney, and C. Greene, “Machine learning in rare disease,” *Nat. Methods*, vol. 20, no. 6, Art. no. 6, Jun. 2023, doi: 10.1038/s41592-023-01886-z.

- [251] F. Yuan, Y. Huang, X. Chen, and E. Cheng, “A Biological Sensor System Using Computer Vision for Water Quality Monitoring,” *IEEE Access*, vol. 6, pp. 61535–61546, 2018, doi: 10.1109/ACCESS.2018.2876336.
- [252] M. Qi and S. Hankey, “Using Street View Imagery to Predict Street-Level Particulate Air Pollution,” *Environ. Sci. Technol.*, vol. 55, no. 4, pp. 2695–2704, Feb. 2021, doi: 10.1021/acs.est.0c05572.
- [253] P. Srivastava, A. Shukla, and A. Bansal, “A comprehensive review on soil classification using deep learning and computer vision techniques,” *Multimed. Tools Appl.*, vol. 80, no. 10, pp. 14887–14914, Apr. 2021, doi: 10.1007/s11042-021-10544-5.
- [254] X. Jin, C. Liu, T. Xu, L. Su, and X. Zhang, “Artificial intelligence biosensors: Challenges and prospects,” *Biosens. Bioelectron.*, vol. 165, p. 112412, Oct. 2020, doi: 10.1016/j.bios.2020.112412.
- [255] J. Park, K. Ko, C. Lee, and C.-S. Kim, “BMBC: Bilateral Motion Estimation with Bilateral Cost Volume for Video Interpolation,” in *Computer Vision – ECCV 2020*, A. Vedaldi, H. Bischof, T. Brox, and J.-M. Frahm, Eds., in Lecture Notes in Computer Science. Cham: Springer International Publishing, 2020, pp. 109–125. doi: 10.1007/978-3-030-58568-6\_7.
- [256] M. M. Ali, B. K. Paul, K. Ahmed, F. M. Bui, J. M. W. Quinn, and M. A. Moni, “Heart disease prediction using supervised machine learning algorithms: Performance analysis and comparison,” *Comput. Biol. Med.*, vol. 136, p. 104672, Sep. 2021, doi: 10.1016/j.combiomed.2021.104672.
- [257] S. Bac, S. J. Quito, K. J. Kron, J. Chae, U. Mitra, and S. Mallikarjun Sharada, “A matrix completion algorithm for efficient calculation of quantum and variational effects in chemical reactions,” *J. Chem. Phys.*, vol. 156, no. 18, p. 184119, May 2022, doi: 10.1063/5.0091155.
- [258] H.-N. Dai, H. Wang, G. Xu, J. Wan, and M. Imran, “Big data analytics for manufacturing internet of things: opportunities, challenges and enabling technologies,” *Enterp. Inf. Syst.*, vol. 14, no. 9–10, pp. 1279–1303, Nov. 2020, doi: 10.1080/17517575.2019.1633689.
- [259] D. J. Brady, L. Fang, and Z. Ma, “Deep learning for camera data acquisition, control, and image estimation,” *Adv. Opt. Photonics*, vol. 12, no. 4, pp. 787–846, Dec. 2020, doi: 10.1364/AOP.398263.
- [260] N. Akkilić, S. Geschwindner, and F. Höök, “Single-molecule biosensors: Recent advances and applications,” *Biosens. Bioelectron.*, vol. 151, p. 111944, Mar. 2020, doi: 10.1016/j.bios.2019.111944.
- [261] P. J. Navarro, F. Pérez, J. Weiss, and M. Egea-Cortines, “Machine Learning and Computer Vision System for Phenotype Data Acquisition and Analysis in Plants,” *Sensors*, vol. 16, no. 5, Art. no. 5, May 2016, doi: 10.3390/s16050641.
- [262] Y. E. Wang, G.-Y. Wei, and D. Brooks, “Benchmarking TPU, GPU, and CPU Platforms for Deep Learning.” arXiv, Oct. 22, 2019. doi: 10.48550/arXiv.1907.10701.
- [263] J. Pei *et al.*, “Towards artificial general intelligence with hybrid Tianjic chip architecture,” *Nature*, vol. 572, no. 7767, Art. no. 7767, Aug. 2019, doi: 10.1038/s41586-019-1424-8.

- [264] V. Sze, Y.-H. Chen, J. Emer, A. Suleiman, and Z. Zhang, “Hardware for machine learning: Challenges and opportunities,” in *2017 IEEE Custom Integrated Circuits Conference (CICC)*, Apr. 2017, pp. 1–8. doi: 10.1109/CICC.2017.7993626.
- [265] N. P. de Leon *et al.*, “Materials challenges and opportunities for quantum computing hardware,” *Science*, vol. 372, no. 6539, p. eabb2823, Apr. 2021, doi: 10.1126/science.abb2823.
- [266] A. Stylianou and M. A. Talias, “Big data in healthcare: a discussion on the big challenges,” *Health Technol.*, vol. 7, no. 1, pp. 97–107, Mar. 2017, doi: 10.1007/s12553-016-0152-4.
- [267] A. Tsamados *et al.*, “The Ethics of Algorithms: Key Problems and Solutions,” in *Ethics, Governance, and Policies in Artificial Intelligence*, L. Floridi, Ed., in Philosophical Studies Series. , Cham: Springer International Publishing, 2021, pp. 97–123. doi: 10.1007/978-3-030-81907-1\_8.
- [268] G. A. Kaissis, M. R. Makowski, D. Rückert, and R. F. Braren, “Secure, privacy-preserving and federated machine learning in medical imaging,” *Nat. Mach. Intell.*, vol. 2, no. 6, Art. no. 6, Jun. 2020, doi: 10.1038/s42256-020-0186-1.
- [269] P. Rajpurkar, E. Chen, O. Banerjee, and E. J. Topol, “AI in health and medicine,” *Nat. Med.*, vol. 28, no. 1, Art. no. 1, Jan. 2022, doi: 10.1038/s41591-021-01614-0.
- [270] S. Steyaert *et al.*, “Multimodal data fusion for cancer biomarker discovery with deep learning,” *Nat. Mach. Intell.*, vol. 5, no. 4, Art. no. 4, Apr. 2023, doi: 10.1038/s42256-023-00633-5.
- [271] A. Esteva *et al.*, “Deep learning-enabled medical computer vision,” *Npj Digit. Med.*, vol. 4, no. 1, Art. no. 1, Jan. 2021, doi: 10.1038/s41746-020-00376-2.
- [272] A. Mathew, P. Amudha, and S. Sivakumari, “Deep Learning Techniques: An Overview,” in *Advanced Machine Learning Technologies and Applications*, A. E. Hassanien, R. Bhatnagar, and A. Darwish, Eds., in *Advances in Intelligent Systems and Computing*. Singapore: Springer, 2021, pp. 599–608. doi: 10.1007/978-981-15-3383-9\_54.
- [273] D. Li, L. Deng, M. Lee, and H. Wang, “IoT data feature extraction and intrusion detection system for smart cities based on deep migration learning,” *Int. J. Inf. Manag.*, vol. 49, pp. 533–545, Dec. 2019, doi: 10.1016/j.ijinfomgt.2019.04.006.
- [274] D. Saxena and J. Cao, “Generative Adversarial Networks (GANs): Challenges, Solutions, and Future Directions,” *ACM Comput. Surv.*, vol. 54, no. 3, p. 63:1-63:42, May 2021, doi: 10.1145/3446374.
- [275] Y. Li, “Research and Application of Deep Learning in Image Recognition,” in *2022 IEEE 2nd International Conference on Power, Electronics and Computer Applications (ICPECA)*, Jan. 2022, pp. 994–999. doi: 10.1109/ICPECA53709.2022.9718847.
- [276] C. S. Costa *et al.*, “A computer vision system for oocyte counting using images captured by smartphone,” *Aquac. Eng.*, vol. 87, p. 102017, Nov. 2019, doi: 10.1016/j.aquaeng.2019.102017.
- [277] G. Morinan *et al.*, “Computer vision quantification of whole-body Parkinsonian bradykinesia using a large multi-site population,” *Npj Park. Dis.*, vol. 9, no. 1, Art. no. 1, Jan. 2023, doi: 10.1038/s41531-023-00454-8.

- [278] J. Kim, A. S. Campbell, B. E.-F. de Ávila, and J. Wang, “Wearable biosensors for healthcare monitoring,” *Nat. Biotechnol.*, vol. 37, no. 4, Art. no. 4, Apr. 2019, doi: 10.1038/s41587-019-0045-y.
- [279] O. Lazcka, F. J. D. Campo, and F. X. Muñoz, “Pathogen detection: A perspective of traditional methods and biosensors,” *Biosens. Bioelectron.*, vol. 22, no. 7, pp. 1205–1217, Feb. 2007, doi: 10.1016/j.bios.2006.06.036.
- [280] G. Aceto, V. Persico, and A. Pescapé, “Industry 4.0 and Health: Internet of Things, Big Data, and Cloud Computing for Healthcare 4.0,” *J. Ind. Inf. Integr.*, vol. 18, p. 100129, Jun. 2020, doi: 10.1016/j.jii.2020.100129.
- [281] S. S. Gill *et al.*, “Transformative effects of IoT, Blockchain and Artificial Intelligence on cloud computing: Evolution, vision, trends and open challenges,” *Internet Things*, vol. 8, p. 100118, Dec. 2019, doi: 10.1016/j.iot.2019.100118.